ISSN 1726-5479

SENSORS & TRANSDUCERS

vol. 210
3 /17

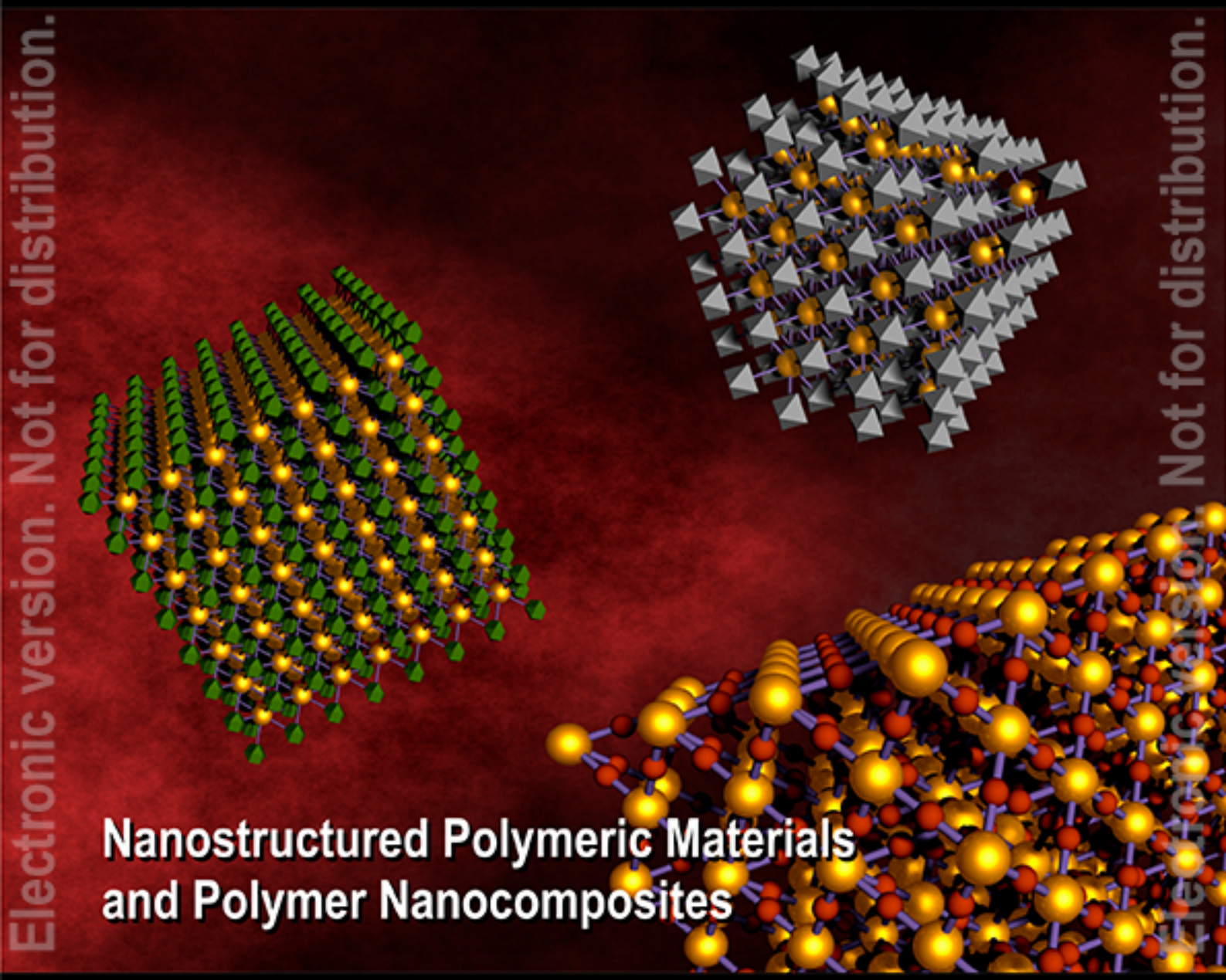

Electronic version. Not for distribution.

Nanostructured Polymeric Materials and Polymer Nanocomposites

International Frequency Sensor Association Publishing

IFSA

Sensors & Transducers

International Official Open Access Journal of the International Frequency Sensor Association (IFSA) Devoted to Research and Development of Sensors and Transducers

Volume 210, Issue 3, March 2017

IFSA Publishing: Barcelona • Toronto

Published by International Frequency Sensor Association (IFSA) Publishing. Printed in the USA.

Sensors & Transducers

Volume 210, Issue 3,
March 2017

www.sensorsportal.com

e-ISSN 1726-5479
ISSN 2306-8515

Sensors & Transducers journal is an open access, peer review international journal published monthly by International Frequency Sensor Association (IFSA).
Available in both: print and electronic (printable pdf) formats.

Sensors & Transducers Journal

Contents

Volume 210
Issue 3
March 2017

www.sensorsportal.com

ISSN 2306-8515
e-ISSN 1726-5479

Research Articles

Authors are encouraged to submit article in MS Word (doc) and Acrobat (pdf) formats
by e-mail: editor@sensorsportal.com. Please visit journal's webpage with preparation instructions:
http://www.sensorsportal.com/HTML/DIGEST/Guides_for_Authors.htm

International Frequency Sensor Association (IFSA).

Sensors & Transducers, Vol. 210, Issue 3, March 2017, pp. 1-8

www.sensorsportal.com

Sensors & Transducers

Published by IFSA Publishing, S. L., 2017
http://www.sensorsportal.com

Flexural, Viscoelastic and Thermal Properties of Epoxy Polymer Composites Modified with Cellulose Nanofibers Extracted from Wheat Straw

Md. Nuruddin, * Mahesh HOSUR, Tanjheel MAHDI, Shaik JEELANI
Department of Materials Science and Engineering,
Tuskegee University, Tuskegee, AL-36088, USA
Tel.: +1334-724-4220, fax: +1334-724-4220
* E-mail: hosur@mytu.tuskegee.edu

Received: 9 January 2017 /Accepted: 28 February 2017 /Published: 31 March 2017

Abstract: The objective of this study is to extract cellulose nanofibers (CNFs) from wheat straw and utilize them in thermoset polymers to improve their performance. CNFs were extracted from wheat straw by formic/peroxyformic acid treatment, hydrogen peroxide bleaching, followed by ball milling. To ensure better interaction between CNFs and epoxy polymer matrix, surface of CNFs was chemically modified by silane treatment. Furthermore, surface treated CNFs were added in varying proportion (1, 2 and 3 %) to an epoxy polymer to fabricate polymer composites. The chemical reaction and structural analysis was evaluated by FTIR analysis. Incorporation of CNFs into matrix increased flexure strength, flexure modulus, storage modulus, glass transition temperature and decomposition temperatures. Maximum improvement was observed for 2 % loading of CNFs as it facilitates maximum crosslinking with epoxy polymers. Maximum improvement in flexure strength and modulus of 22.5 % and 31.7 %, respectively was obtained by the addition of 2 % CNFs. Furthermore, storage modulus was 22.3 % higher than neat epoxy for 2 % loading of CNFs at room temperature, while T_g improved by 18 %. Thermal stability of composite was improved probably due to the catalytic effect of CNFs. Cellulose nanofibers (CNFs) enhanced both first and second decomposition temperatures by up to 19 and 14 °C, respectively over neat system.

Keywords: Cellulose nanofibers, Ball milling, Epoxy polymer, Glass transition temperature, Decomposition.

1. Introduction

Now a day, development of nanomaterials has drawn wide attention of the researchers all over the world. Numerous research studies have been conducted to develop nanomaterials for various engineering applications such as automotive components, building construction materials, electronic devices, and also for biomedical applications. Unfortunately, most of these nanomaterials fail to satisfy the concept of sustainability. Therefore, researchers are trying to develop bio-based renewable nanomaterials of high mechanical and thermal properties as replacement materials. Cellulose is an important component of lignocellulosic fibers, which consists of a bundle of cellulose nanofibers (CNFs). Several research studies have been conducted to isolate cellulose nanofibers from plant based materials [1-5]. Scientists and engineers are working together to utilize cellulose nanofibers in various engineering applications.

Cellulose nanofibers have shown excellent mechanical properties (high specific strength and modulus), better biodegradability, high aspect ratio,

renewability, large specific surface area, low coefficient of thermal expansion, environmental benefits, low cost and availability [5-7]. These properties of CNFs make them comparable with other engineering materials such as carbon nanotube, carbon nanofibers, graphene nanoplatelets and nanoclay. CNFs have been considered as effective reinforcing materials for fabrication of green composite materials because of higher mechanical properties and their web-like structure.

One of the main disadvantages of using CNFs as reinforcing filler in the polymer matrix is moisture absorption and tendency to be agglomerated. The interaction of hydroxyl groups result in strong hydrogen bond formation between the fibers and also with the moisture. Hydrophilic CNFs show poor dispersion capability in hydrophobic polymer matrix [8]. Therefore, several research studies have been conducted to modify the surface to make them suitable for both hydrophilic and hydrophobic polymer matrix [9-10].

Cellulose nanofibers (CNFs) can be used as filler materials in a wide range of thermosetting polymers such as epoxy and polyester [11-12]. Among the thermosetting polymers, epoxy is a high performance polymer that has applications ranging from rocket casing to dental filling. Incorporation of CNFs into epoxy polymer matrix has shown to improve mechanical properties such as fatigue resistance, high strength and stiffness of the materials [13-14]. Nevertheless, the main drawback of epoxy/CNFs composite is the poor adhesion capability of CNFs that causes poor dispersion into the matrix. Therefore, several techniques such as surface modification as well as solvent exchange methods have been used to increase the adhesion ability of CNFs [8, 15].

In the present study, cellulose nanofibers (CNFs) were extracted from wheat straw by delignification and bleaching treatment followed by ball milling technique for use as reinforcing materials in an epoxy polymer. Surface of CNFs was modified by treating it with silane coupling agent. These CNFs were added to epoxy polymer at different loading to fabricate polymer composites. The fabricated composites were characterized by using SEM, Flexure, DMA, FTIR and TGA.

2. Materials and Experiments

2.1. Materials

SC-15 Epoxy, a commercially available low viscosity resin (300 cps), purchased from Applied Poleramic, Inc. was used. It is two phase resin containing part-A (mixture of diglycidyl ether of bisphenol A and aliphatic diglycidyl ether epoxy toughener) and part B (hardener, mixture of cycloaliphatic amine and polyoxyl alkyl amine). Wheat straw was purchased from Home Depot, USA. Hydrogen peroxide (30 wt. % in H_2O), ethanol (≥ 99.5 %), formic acid (≥ 95 %), sodium hydroxide pellets, silane coupling agent (3-aminopropyltriethoxysilane), methanol (anhydrous, 99.8 %) and acetic acid (ACS reagent, ≥ 99.7) were purchased from Sigma–Aldrich (St. Louis, MO, USA).

2.2. Pretreatment of Wheat Straw

Cellulose was extracted from wheat straw according to Nuruddin, *et al.* [16]. In brief, wheat straw and 90 % formic acid were placed on a hot plate maintained at 110 °C for 2 hours. At the end of the reaction time, the fibers were filtered in a Buchner funnel and washed with formic acid followed by hot distilled water. Resulting pulp was further treated with peroxyformic acid solution in hot water bath at 80 °C for 2 hours to remove amorphous content (lignin, hemicellulose and pectin). Finally, delignified fibers were filtered to separate cooking liquor (lignin and hemicellulose mixed with formic acid) from cellulose and washed several times with hot water. Delignified fibers were subjected to bleaching by treating them with 35 % H_2O_2 solution and NaOH solution (to maintain pH: 11-12), and kept in a hot water bath at 80 °C for 2 hours. Finally, the pulp was washed several times with distilled water to ensure complete removal of residual lignin.

2.3. Isolation of Cellulose Nanofibers (CNFs)

In our laboratory, a new technique has been developed to isolate CNFs by ball milling [17]. Approximately 10 gm of bleached cellulose was soaked in 10 ml of 80 % ethanol solution and the fiber was subjected to milling for 120 minutes in a Mixer/Mill 8000D™ (SPEX Sample Prep, USA) using zirconia ceramic grinding vial and ball with diameter 12.7 mm. After ball milling, the mixture was repeatedly washed with distilled water and centrifuged until the pH of the cellulose reaches between 6 and 7. Finally, the suspension of ball milled cellulose nanofibers (CNFs) was freeze dried.

2.4. Surface Modification of Cellulose

1 % silane coupling agent (total weight of fiber) was mixed with 80/20 v/v ethanol/water mixture and then 5 g freeze dried CNFs was added to the mixture. 1 % acetic acid was added dropwise to maintain PH near 3.5, and then the mixture was magnetically stirred at 500 rpm for 90 minutes, maintaining the room temperature. After completion of the reaction, the CNFs suspensions were repeatedly centrifuged and washed with distilled water until the PH became 6. Then samples were freeze dried to use it as filler materials.

2.5. Fabrication of Nanocomposites

Precalculated amount of part-A and CNFs were mixed manually in a beaker and then ultrasonicated for 20 minutes at 40 °C, using "Sonics Vibra-cell" (Sonics & Materials Inc., USA) set at 30 seconds pulse on, 20 seconds pulse off, and amplitude of 50 µ. Then the sonicated mixture was magnetically stirred at 500 rpm for 5 hours at 40 °C temperature to ensure complete dispersion of CNFs in the polymer matrix. After that, part B was mixed with part A modified with CNFs in the ratio of 10:3 (part A: part B). The resultant mixture was stirred again using high speed mechanical stirrer for 5 minutes to ensure complete mixing. Then the mixture was kept in a vacuum oven to remove bubbles formed during mixing of part A and part B. After removal of bubbles, the resin was poured into the metal molds for desired shape and kept in an oven at 60 °C for 1 hour followed with 120 °C for 3 hours. For neat samples, calculated amount of part A and part B were mixed in the ratio of 10:3 by using mechanical stirrer following the same procedure as mentioned for CNFs modified samples.

2.6. Characterization

2.6.1. Flexure Test

Three point bending flexure test was conducted according to ASTM D790-02, using Zwick-Reoll Z 2.5 machine. The test was conducted under displacement control mode with a crosshead speed of 1.2 mm/min. The sample size was 96 mm × 12.5 mm × 4.5 mm (span length × width × thickness). The span length to thickness ratio of 16:1 was maintained, and at least 5 samples of each type nanocomposites were tested at room temperature.

2.6.2. Scanning Electron Microscopy (SEM)

Scanning electron micrograph of ball milled CNFs was taken using JEOL JSM-6400 scanning electron microscope (SEM) at 20 kV accelerating voltage. Morphological studies of neat epoxy and CNFs reinforced epoxy polymer nanocomposites were conducted using JEOL JSM-6400 scanning electron microscope (SEM) at 15 kV accelerating voltage. Surface of each sample was sputtered with a thin layer of gold particle before SEM conducted.

2.6.3. Transmission Electron Microscopy (TEM)

A drop of dilute cellulose nanofibers (CNFs) suspension was deposited on the 300 mesh Formvar/Carbon coated support film grids. The excess liquid was absorbed by a piece of filter paper and then allowed to dry at room temperature. When the sample has been dried, then it was observedusing ZEISS EM10 Transmission Electron Microscope (Thornwood, NY) operated at 60 kV accelerating voltage.

2.6.4. Fourier Transfer-infrared (FTIR) Spectroscopy

Structural characterization was conducted on CNFs, surface treated CNFs, neat epoxy and CNFs reinforced epoxy polymer composite, using Shimadzu FTIR 8400s equipped with MIRacle^{TM} ATR, and samples were scanned from 550-3500 cm^{-1} with a resolution of 4 cm^{-1}.

2.6.5. Dynamic Mechanical Analysis

Dynamic Mechanical Analysis (DMA) of nanocomposites was conducted according to ASTM D4065 using TA Instrument DMA Q-800. The tests were performed in a three-point bending mode at an amplitude of 15 µm and oscillation frequency of 1 Hz. The temperature range was 30 to 150 °C at a heating rate of 5 °C/min. The sample size was 60 mm × 12.5 mm × 4.5 mm, and at least 3 samples of each type of composites were tested. Storage modulus and tan-delta as a function of temperature were obtained. Glass transition temperature was obtained from Tan-delta curve.

2.6.6. Thermogravimetric Analysis (TGA)

Thermal stability of polymer nanocomposites and neat epoxy were studied using thermogravimetric analysis Q-500 from TA Instruments Inc. (DE). Approximately 10-12 mg Samples were taken for the test. TG scans were performed at 10 °C/min from 25 - 600 °C under nitrogen environment with a purge flow rate of 60 mL/min.

3. Results and Discussion

3.1. Morphological Characterization of CNFs and Nanocomposites

Fig. 1 shows the SEM and TEM images of extracted web like CNFs. The maximum and minimum diameters were calculated from TEM images using MaxIm DL5 software. The maximum and minimum diameter of ball milled CNFs were approximately and 45 nm and 17 nm respectively.

3.2. Chemical Structure Analysis

FTIR spectroscopy analysis of CNFs and silane treated CNFs was carried out to confirm the chemical reaction between silane coupling agent and cellulose and were shown in Fig. 2.

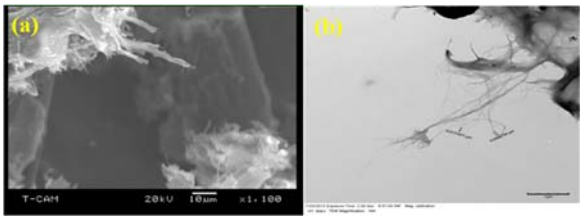

Fig. 1. (a) SEM, and (b) TEM images of Cellulose nanofibers (CNFs).

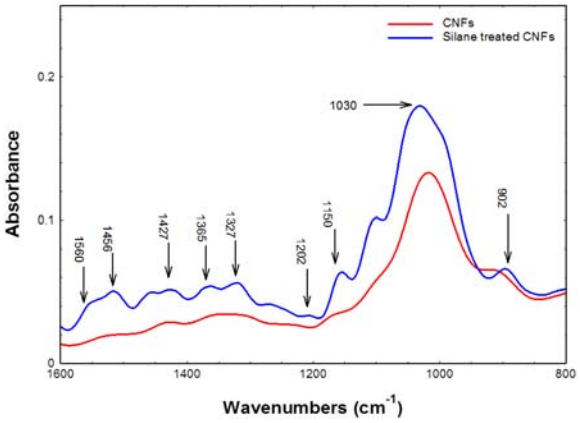

Fig. 2. FTIR spectra of CNFs and silane treated CNFs.

Silane treated CNFs show absorption bands at 1560 and 1456 cm^{-1} indicating deformation modes of amino groups (NH_2) that are strongly hydrogen bonded with hydroxyl groups of both cellulose and silanol (formed during hydrolysis of silane coupling agent) [13]. The weak peaks at 1427, 1365 and 1327 cm^{-1} represent C-H stretching and C-H or O-H bending [18], which can be seen in untreated and treated cellulose nanofibers. The intense peaks at 1150 and 1202 cm^{-1} represent -Si-O-Si- linkage and -Si-O-Cellulose bonds. -Si-O-Si- bond indicated the existence of polysiloxanes chemically bonded with the cellulose nanofibers and the latter bond proved the condensation reaction between cellulose nanofibers and silane coupling agent as shown in the reaction [19]. The broad peaks at 1030 and 903 cm^{-1} indicative of C-O stretching and C-H deformation vibrations associated with cellulose [20-21], and can be seen in all spectra. The increase in intensity for silane treated CNFs is due to the overlapping of Si-O-Si band and C-O stretching of cellulose [22].

FTIR analysis was also conducted on neat epoxy and silane treated cellulose nanofibers reinforced epoxy polymer composite to understand the chemical structure and chemical reaction (Fig. 3). The broad peak around 3100-3600 cm^{-1} for neat epoxy was due to the O-H stretching vibration of hydroxyl group in epoxy and N-H stretching of primary and secondary amine of hardener. Incorporation of silane treated CNFs into the epoxy system produced a doublet, which was mainly due to the unreacted primary amine groups. The peak at 3042 cm^{-1} is the characteristics peak of C-H stretching of terminal oxirane group of epoxy resin. The peak at 2902 and 2860 cm^{-1} represented the characteristics peaks of C-H stretching of epoxy resin, the intensity of which decreases with addition of CNFs. A peak at 2310 cm^{-1} for both epoxy and epoxy/CNFs was observed, which might be due to double CO_2 band [23]. The sharp peak at 1506 cm^{-1} represents the N-H deformation of primary amine of hardener and silane treated CNFs used for epoxy resin. The peaks at 1452 and 1605 cm^{-1} correspond to the aromatic ring stretching of C=C, which is the characteristics of DGEBA epoxy resin. The sharp peaks at 1095 and 1032 cm^{-1} represent the stretching of C-O of saturated aliphatic primary alcohols [24]. These peak intensities decreased with the addition of cellulose nanofibers. The peaks at 1236 and 932 cm^{-1} indicated the stretching of epoxide (-C-O) bonds [25]. Finally, the peak at 823 cm^{-1} was attributed to the stretching of C-O-C of terminal oxirane group of epoxy system.

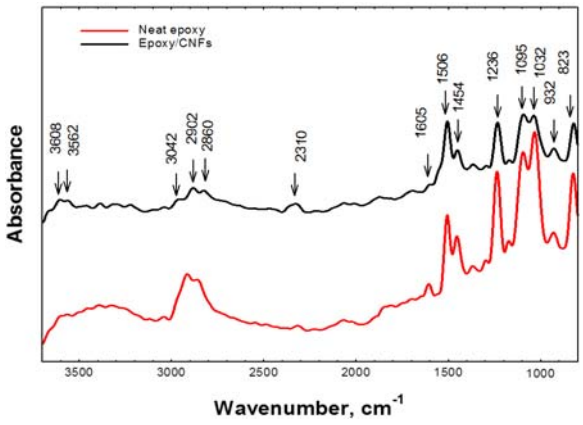

Fig. 3. FTIR spectra of neat epoxy and CNFs reinforced epoxy nanocomposites.

3.3. Flexure Test

Flexure properties of nanocomposites are characterized by subjecting neat epoxy and CNFs reinforced nanocomposites under three point bending load. The stress-strain curves as shown in the Fig. 4, obtained from flexure test show significant non-linearity, although no remarkable yield point was observed in the curves. Flexure test results obtained from various samples are compared in the Fig. 5.

From Fig. 4, it can be seen that incorporation of cellulose nanofibers into epoxy polymer matrix exhibited significant improvement of flexure strength and modulus. The highest flexure strength and modulus were achieved from 2 % CNFs/epoxy nanocomposite (22.5 % and 31.7 % higher than neat epoxy). In contrast, a reduction in flexure properties at 3 % loading might be due to the strong attractive forces between cellulose nanofibers leading to cluster or agglomeration of CNFs. Due to poor dispersion of CNFs at 3 % loading, CNFs agglomerate in the resin system leading to the reduction of load transfer between CNFs and epoxy polymer.

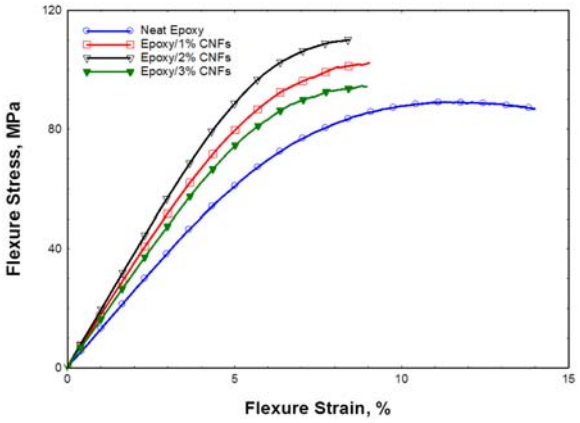

Fig. 4. Flexural stress–strain response of neat epoxy and CNFs incorporated epoxy nanocomposites.

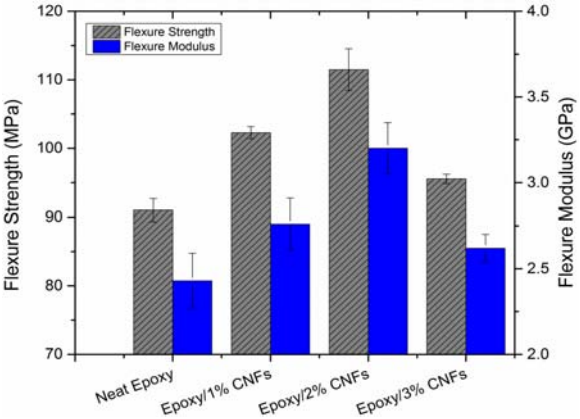

Fig. 5. Comparative value of flexure strength and modolus of neat epoxy and CNFs incorporated epoxy nanocomposites.

Uniform dispersion of CNFs ensures more surface area of cellulose nanofibers to be exposed to the matrix and better interaction between CNFs and epoxy polymer. Silane treated CNFs contain amino functional groups that are strong nucleophile. Therefore, these amino functional groups of CNFs get attached to epoxide group of epoxy SC-15 and form strong covalent bond by ring opening reaction. As a result, higher cross-linking between epoxy molecules takes place resulting in an interlocking structure in the matrix reducing the mobility of epoxy polymer chains through the system. Chemically interlocked resin and CNFs structure may facilitate stress transfer between matrix/fiber and fiber/fiber.

Strong covalent bonds between fibers and polymers must be broken before the sample fails while subjecting to loading. Higher crosslinking means formation of higher covalent bonds between fibers and polymer matrix. Hence, flexure strength and modulus of nanocomposites increases after the addition of CNFs. After initiation of crack due to loading, the propagation of the crack gets restricted by the presence of CNFs. Thus, the direction of crack propagation is changed in the presence of CNFs requiring more energy to cause the failure of the composites.

Analysis of failure behavior through scanning electron microscopy of neat epoxy and CNFs modified epoxy polymer composites is presented in Fig. 6. It is apparent from the SEM images that the fracture surface of CNFs modified nanocomposites is rougher than the neat samples. Among the nanocomposites, 2 % CNFs reinforced composites showed roughest fracture surface indicating the highest resistance to crack propagation by the materials. In contrast, the exposed fracture surface of neat epoxy and 3 % CNFs incorporated samples exhibit relatively smoother surface than 2 % CNFs incorporated samples (Fig. 6(a) and Fig. 6(d)). Addition of higher loading causes cluster of agglomerated CNFs. This agglomeration might be due to two factors. One is, 3 % loading CNFs was more than need to crosslink with epoxy polymer resulting in unreacted CNFs in the form of agglomeration. Another important factor is the higher tendency of hydrogen bonding between the hydrogen groups on the surfaces of CNFs. The crack for 3 % CNFs reinforced samples initiated from a zone where the CNFs appear to be agglomerated to form a cluster.

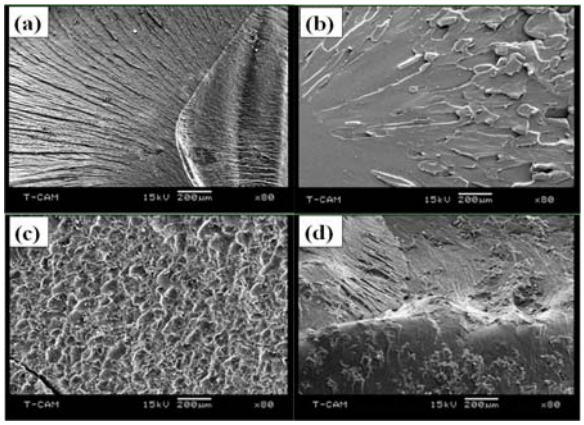

Fig. 6. Fracture surfaces of (a) neat epoxy, (b) epoxy/1 % CNFs, (c) epoxy/2 % CNFs and (d) epoxy/3 % CNFs.

3.4. Viscoelastic Properties of Epoxy Nanocomposites

The viscoelastic properties of neat epoxy and CNFs reinforced nanocomposites are evaluated as a function of temperature. Fig. 7 and Fig. 8 show the comparison of dynamic mechanical properties such as storage modulus and tan-delta as functions of temperature.

Storage modulus measures the energy stored in the materials after deformation when subjected to cyclic loading. Fig. 7(a) represents the storage modulus of nanocomposites as a function of temperature. From Fig. 8, it can be seen that the addition of CNFs increases the storage modulus as compared with neat epoxy. Maximum storage modulus was achieved for 2 % loading of CNFs (22.3 % higher than neat epoxy) at room temperature. The polymer chains deform with

increasing temperature leading to decrease in stiffness. As mentioned earlier, CNFs form covalent bonds with epoxy polymer by crosslinking that restrict the movement of the polymer chains. In contrast, lower value of storage modulus for 3 % loading of CNFs can be attributed the agglomeration of CNFs.

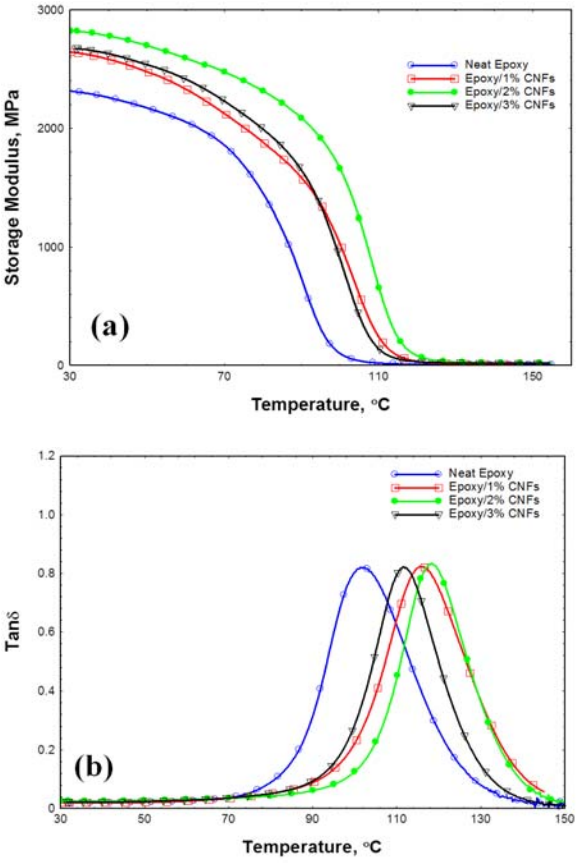

Fig. 7. (a) Storage modulus versus temperature curve and (b) Tanδ versus temperature curves of neat epoxy and epoxy/CNFs nanocomposites.

Fig. 7(b) shows the Tan-delta curve of neat epoxy and different percentage of CNFs incorporated epoxy composite samples. Tan-delta value represents the damping properties of the materials and can be expressed as the ratio of loss modulus over storage modulus. The peak of tan-delta curve represents the glass transition temperature (T_g). From Fig. 8, it can be observed that the value of T_g increases with the addition of CNFs up to 2 %. About 18 % improvement of T_g was achieved at 2 % loading of CNFs compared with neat epoxy polymer composite. Good dispersion of CNFs was achieved for 2 % loading CNFs into the polymer matrix leading to sufficient crosslinking between matrix and cellulose nanofibers and ensures severe restriction of movement of polymer chain when temperature increases. Thus, the matrix/CNFs crosslinked network initiates to move at a relatively higher temperature than neat epoxy sample leading to higher T_g value. Salam, *et al.* reported that improved interfacial bonding between CNTs and epoxy polymer leads to higher T_g value [26]. At higher loading of CNFs, T_g value was lower possibly because of agglomeration tendency of CNFs.

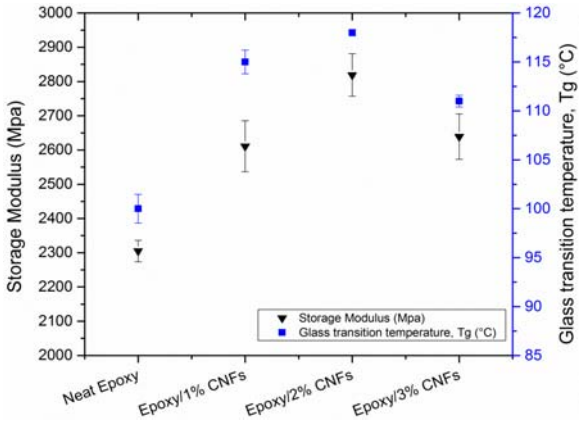

Fig. 8. Comparative study of storage modulus and glass transition temperature (T_g) of nanocomposites.

3.5. Thermal Stability of Nanocomposites

Thermal stability of neat epoxy and cellulose nanofibers incorporated epoxy polymer composites was evaluated by thermo-gravimetric analysis (TGA). Summary of thermal stability of all samples are evaluated in terms of onset of decomposition, (Ti) and maximum decomposition temperature as shown in Table 1. From Table 1 and Fig. 9, it can be seen that the onset temperature varied significantly with the addition of CNFs into epoxy polymer matrix.

Table 1. Thermal properties of neat epoxy and CNFs incorporated epoxy nanocomposites.

Sample	Onset Temperature, Ti (°C)	Maximum Decomposition Temperature (°C)	
		T_1 max	T_2 max
Neat	311 ± 2.3	323 ± 4.2	362 ± 6.5
1 % CNFs/Epoxy	319 ± 0.8	330 ± 0.5	366 ± 3.5
2 % CNFs/Epoxy	327 ± 2.9	342 ± 2.6	376 ± 4.1
3 % CNFs/Epoxy	323 ± 1.7	335 ± 0.9	365 ± 6.5

Onset temperature of neat epoxy was 311 °C and increased up to 327 °C after incorporation of CNFs.

From DTG curves shown in Fig. 9(b), the decomposition of all samples show two distinct peaks. The first decomposition peak was noticed around 323-342 °C with 13-26 % weight loss, which was mainly due to the decomposition of lower molecular weight materials. The second decomposition peak was around 362-376 °C with 48-60 % weight loss of the samples, which was the result of decomposition of highly

crosslinked materials [27]. Cellulose nanofibers (CNFs) enhance both first and second decomposition temperature with a maximum of 19 and 14 °C respectively over neat system. This improvement of thermal stability can be attributed to the probable catalytic effect of CNFs that enhances the cross-linking reaction between polymers and curing agent [13].

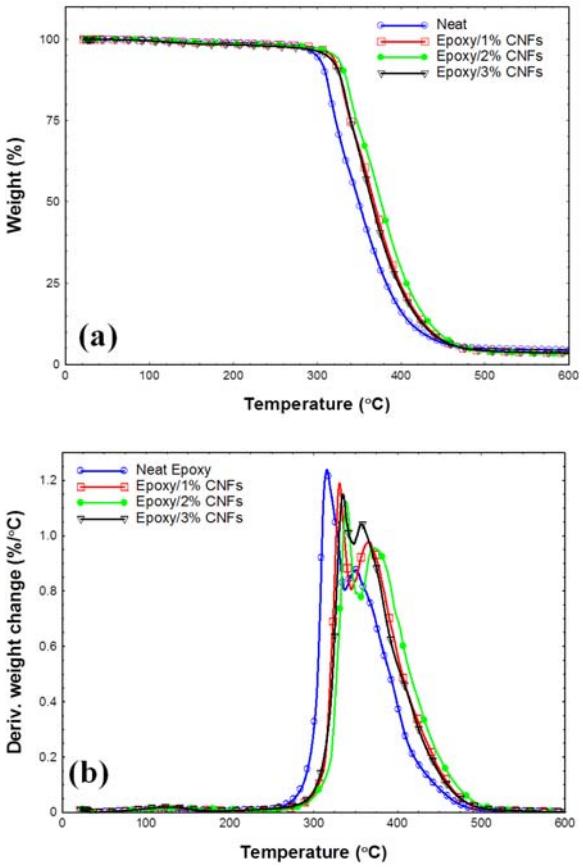

Fig. 9. (a) TG, and (b) DTG curves of neat epoxy and epoxy/CNFs nanocomposites.

4. Conclusions

In this study, silane treated cellulose nanofibers were incorporated into the DGEBA epoxy resin in order to improve both mechanical and thermal properties of nanocomposites. The chemical reaction and structural analysis was evaluated by FTIR analysis. Incorporation of CNFs into matrix increases flexure strength, flexure modulus, storage modulus, glass transition temperature and decomposition temperatures. Maximum improvement was observed for 2 % loading of CNFs as it facilitates maximum crosslinking with epoxy polymers. The highest flexure strength and modulus were improved by 22.5 % and 31.7 % after addition of 2 % CNFs. Furthermore, storage modulus was 22.3 % higher than neat epoxy for 2 % loading of CNFs at room temperature, while T_g was improved approximately 18 %. Thermal stability of composite was improved probable due to the catalytic effect of CNFs. Cellulose nanofibers (CNFs) enhance both first and second decomposition temperature with a maximum of 19 and 14 °C respectively over neat system.

Acknowledgements

The authors are grateful to the NSF-CREST (grant No. 1137681) and NSF-EPSCoR (grant No. 1158862) for the financing support to carry out this research.

References

[1]. F. W. Herrick, R. L. Casebier, J. K. Hamilton, K. R. Sandberg, Microfibrillated cellulose: morphology and accessibility, *J. Appl. Polym. Sci.: Appl. Polym. Symp.; (United States)*, ITT Rayonier Inc., Shelton, WA, 1983.

[2]. N. Hayashi, T. Kondo, M. Ishihara, Enzymatically produced nano-ordered short elements containing cellulose Iβ crystalline domains, *Carbohydrate Polymers*, Vol. 61, No. 2, 2005, pp. 191-197.

[3]. T. Saito, S. Kimura, Y. Nishiyama, A. Isogai, Cellulose nanofibers prepared by TEMPO-mediated oxidation of native cellulose, *Biomacromolecules*, Vol. 8, No. 8, 2007, pp. 2485-2491.

[4]. W. Chen, H. Yu, Y. Liu, P. Chen, M. Zhang, Y. Hai, Individualization of cellulose nanofibers from wood using high-intensity ultrasonication combined with chemical pretreatments, *Carbohydrate Polymers*, Vol. 83, No. 4, 2011, pp. 1804-1811.

[5]. M. A. S. Azizi Samir, F. Alloin, A. Dufresne, Review of recent research into cellulosic whiskers, their properties and their application in nanocomposite field, *Biomacromolecules*, Vol. 6, No. 2, 2005, pp. 612-626.

[6]. W. J. Orts, J. Shey, S. H. Imam, G. M. Glenn, M. E. Guttman, J.-F. Revol, Application of cellulose microfibrils in polymer nanocomposites, *Journal of Polymers and the Environment*, Vol. 13, No. 4, 2005, pp. 301-306.

[7]. T. Nishino, I. Matsuda, K. Hirao, All-cellulose composite, *Macromolecules*, Vol. 37, No. 20, 2004, pp. 7683-7687.

[8]. A. Brandt, J. Gräsvik, J. P. Hallett, T. Welton, Deconstruction of lignocellulosic biomass with ionic liquids, *Green Chemistry*, Vol. 15, No. 3, 2013, pp. 550-583.

[9]. M. Abdelmouleh, S. Boufi, M. N. Belgacem, A. Dufresne, A. Gandini, Modification of cellulose fibers with functionalized silanes: effect of the fiber treatment on the mechanical performances of cellulose–thermoset composites, *Journal of Applied Polymer Science*, Vol. 98, No. 3, 2005, pp. 974-984.

[10]. X. Li, L. G. Tabil, S. Panigrahi, Chemical treatments of natural fiber for use in natural fiber-reinforced composites: a review, *Journal of Polymers and the Environment*, Vol. 15, No. 1, 2007, pp. 25-33.

[11]. J. W. Gilman, D. L. VanderHart, T. Kashiwagi, Thermal decomposition chemistry of poly (vinyl alcohol), in *Proceedings of the American Chemical Society Symposium Series* 599 *on Fire and Polymers II: Materials and Test for Hazard Prevention*1994, pp. 161-185.

[12]. S. Liang, Q. Huang, L. Liu, K. L. Yam, Microstructure and molecular interaction in glycerol plasticized

chitosan/poly (vinyl alcohol) blending films, *Macromolecular Chemistry and Physics*, Vol. 210, No. 10, 2009, pp. 832-839.
[13]. P.-Y. Kuo, N. Yan, M. Sain, Influence of cellulose nanofibers on the curing behavior of epoxy/amine systems, *European Polymer Journal*, Vol. 49, No. 12, 2013, pp. 3778-3787.
[14]. M. Nuruddin, R. Gupta, A. Tcherbi-Narteh, M. Hosur, S. Jeelani, Synergistic Effect of Graphene Nanoplatelets and Nanoclay on Epoxy Polymer Nanocomposites, *Advanced Materials Research, Trans Tech Publications*, 2015, pp. 155-159.
[15]. A. Valadez-Gonzalez, J. Cervantes-Uc, R. Olayo, P. Herrera-Franco, Effect of fiber surface treatment on the fiber–matrix bond strength of natural fiber reinforced composites, *Composites Part B: Engineering*, Vol. 30, No. 3, 1999, pp. 309-320.
[16]. M. Nuruddin, A. Chowdhury, S. Haque, M. Rahman, S. Farhad, M. S. Jahan, A. Quaiyyum, Extraction and characterization of cellulose microfibrils from agricultural wastes in an integrated biorefinery initiative, *Cellulose Chem. Technol.*, Vol. 45, No. 5-6, 2011, pp. 347-354.
[17]. M. Nuruddin, M. Hosur, M. Uddin, D. Baah, S. Jeelani, A novel approach for extracting cellulose nanofibers from lignocellulosic biomass by ball milling combined with chemical treatment, *Journal of Applied Polymer Science*, Vol. 133, No. 9, 2016, pp. 1-10.
[18]. M. Jiang, M. Zhao, Z. Zhou, T. Huang, X. Chen, Y. Wang, Isolation of cellulose with ionic liquid from steam exploded rice straw, *Industrial Crops and Products*, Vol. 33, No. 3, 2011, pp. 734-738.
[19]. A. N. Frone, D. M. Panaitescu, D. Donescu, C. I. Spataru, C. Radovici, R. Trusca, R. Somoghi, Preparation and characterization of PVA composites with cellulose nanofibers obtained by ultrasonication, *BioResources*, Vol. 6, No. 1, 2011, pp. 487-512.
[20]. A. Alemdar, M. Sain, Isolation and characterization of nanofibers from agricultural residues–Wheat straw and soy hulls, *Bioresource Technology*, Vol. 99, No. 6, 2008, pp. 1664-1671.
[21]. R. Li, J. Fei, Y. Cai, Y. Li, J. Feng, J. Yao, Cellulose whiskers extracted from mulberry: A novel biomass production, *Carbohydrate Polymers*, Vol. 76, No. 1, 2009, pp. 94-99.
[22]. W. Zhang, X. Yang, C. Li, M. Liang, C. Lu, Y. Deng, Mechanochemical activation of cellulose and its thermoplastic polyvinyl alcohol ecocomposites with enhanced physicochemical properties, *Carbohydrate Polymers*, Vol. 83, No. 1, 2011, pp. 257-263.
[23]. Y. Yamashita, C. Sasaki, Y. Nakamura, Development of efficient system for ethanol production from paper sludge pretreated by ball milling and phosphoric acid, *Carbohydrate Polymers*, Vol. 79, No. 2, 2010, pp. 250-254.
[24]. Y. Nishiyama, J. Sugiyama, H. Chanzy, P. Langan, Crystal structure and hydrogen bonding system in cellulose Iα from synchrotron X-ray and neutron fiber diffraction, *Journal of the American Chemical Society*, Vol. 125, No. 47, 2003, pp. 14300-14306.
[25]. M. S. Jahan, A. Saeed, Z. He, Y. Ni, Jute as raw material for the preparation of microcrystalline cellulose, *Cellulose*, Vol. 18, No. 2, 2011, pp. 451-459.
[26]. M. Salam, M. Hosur, S. Zainuddin, S. Jeelani, Improvement in Mechanical and Thermo-Mechanical Properties of Epoxy Composite Using Two Different Functionalized Multi-Walled Carbon Nanotubes, *Open Journal of Composite Materials*, Vol. 3, No. 2A, 2013, pp. 1-9.
[27]. S. Zainuddin, M. Hosur, Y. Zhou, A. T. Narteh, A. Kumar, S. Jeelani, Experimental and numerical investigations on flexural and thermal properties of nanoclay–epoxy nanocomposites, *Materials Science and Engineering: A*, Vol. 527, 2010, pp. 7920-7926.

Published by International Frequency Sensor Association (IFSA) Publishing, S. L., 2017 (http://www.sensorsportal.com).

Sensors & Transducers, Vol. 210, Issue 3, March 2017, pp. 9-16

www.sensorsportal.com

Sensors & Transducers

Published by IFSA Publishing, S. L., 2017
http://www.sensorsportal.com

Development of Perovskite Sensitized Thin Film Solar Cells Based on Graphene Oxide/TiO_2 Photoanodes

[1] Momina KHANNAM, [1] Shyamalima SHARMA, [2] Ranoo BHARGAV, [2] Asit PATRA and [1, *] Swapan Kumar DOLUI

[1] Department of Chemical Sciences, Tezpur University, Napaam, Tezpur, Dist. Sonitpur, Assam-784028, India

[2] Physics of Energy Harvesting Division, CSIR-National Physical Laboratory, Dr. K. S. Krishnan Road, Pusa, New Delhi-110 012, India

[*] Tel.: 9957198489

[*] E-mail: dolui@tezu.ernet.in

Received: 9 January 2017 /Accepted: 3 March 2017 /Published: 31 March 2017

Abstract: Graphene oxide/TiO_2(GO/TiO_2) nanocomposites with different concentrations of GO were prepared by a self-assemble method. The synthesized GO/TiO_2 nanocomposites are characterized by X-ray diffraction (XRD), scanning electron microscopy (SEM), and transmission electron microscopic (TEM) analysis. Using these GO/TiO_2 nanocomposites as an electron collection layer a series of solid state perovskite sensitized solar cells were fabricated. The photovoltaic properties like short circuit current density and photo conversion efficiency of the fabricated device were evaluated. It was noticed that the nanocomposites has significant effects on the photovoltaic properties of the device. With increase in the amount of GO in the nanocomposites the short circuit current density of the devices increased from 1.79 to 4.65 $mAcm^{-2}$ and the photo conversion efficiency increased from 0.413 to 1.34 %.

Keywords: Nanocomposites, Perovskite, Solar cells, Graphene oxide, PCE.

1. Introduction

Now a days, the growing energy demand can be fulfilled to a large extent by utilizing a small fraction of solar radiation. Different solar cells such as amorphous and nanocrystalline Si [1], inorganic compound semiconductors [2], quantum dot solar cells (QDSCs) [3], dye-sensitized solar cells (DSSCs) [4], organic solar cells (OSCs) [5] and now perovskite-based meso-superstructured solar cells (MSSCs) [6] have been developed to achieve the needs. Evolving from liquid electrolyte based DSSCs, solid-state perovskite-based solar cells, made by using methylammonium lead iodide ($CH_3NH_3PbI_3$) perovskite materials coated upon the surface of mesoscopic TiO_2 substrates, have shown a very promising efficiency. Organo-metal halide perovskites with low loss in photovoltaic operation have been employed as the absorber layer in hybrid solar cells. The organo-metal can be synthesized by a simple solution based synthetic route from abundant sources like C, N, Pb, and halogens [7]. With large absorption coefficient [8], higher carrier mobility [9], and direct band gap lead halide inorganic layer is an attractive class of materials as light harvesters in heterojunction solar cells.

For the first time Miyasaka and co-workers reported a methylammonium lead iodide "perovskite sensitized" solar cell by employing a liquid electrolyte in a conventional dye-sensitized solar cell (DSSC) architecture which gives an efficiency of 3.8 % [10]. Perovskite can be used also as an efficient light harvester as well as a HTM in the fabricated devices. However, to get a better efficiency, HTM is used

which collects the holes and transfers them to the back electrode. Solar cells employing methylammonium lead iodide perovskite absorber materials on mesoscopic TiO_2 have shown very promising efficiency. The conduction and valence band of the methylammonium lead iodide injects electron into the TiO_2 and whole transport to the back contact respectively. Now a days, a wide variety of organic polymer hole-conductors are used in these perovskite solar cells [11-13]. The most outstanding among these hole-conducting polymers is spiro-OMeTAD (2,2′,7,7′-tetrakis(N,N-di-p-methoxy phenylamine)-9,9′-spirobifluorene) which gives a very high PCE of 9.7 % as reported by Kim and his co-workers [14].

In many growing technologies, TiO_2 has drawn special attention with the advantage that it can prevent shunting and leakage currents under reverse bias [15]. In general, TiO_2 coated conductive substrate is used as an electron collection layer which plays a very important role in thin-film solar cells by facilitating selective charge collection. However, these materials have some major drawback as it requires high-temperature processing to increase their crystallinity and charge carrier mobility [16].

In the meantime, the two dimensional material graphene have got numerous fundamental development with a number of unique properties. Graphene is identified as one of the strongest materials with very high thermal and electrical conductivity [17]. In addition, graphene possesses high charge mobility [18-19] as well as high optical transmittance [20-21]. With these unique properties of graphene, it find diverse field applications like photovoltaics, photocatalysis, nanoelectronics, sensors, etc. [22-24]. With the introduction of graphene in TiO_2 based nanocomposites, the strong interfacial interaction among the components facilitated the high conductivity and better electrical properties of such materials [25-27].

Inspired from the foregoing discussion, we have developed a series of nanocomposites based on graphene oxide (GO) and nano TiO_2. The synthesized GO/TiO_2 then employed as the electron selective contact to fabricate organo metal halide perovskite solar cell. The photovoltaic properties like short circuit current density and the photo conversion efficiency of the fabricated device were evaluated as a function of GO content.

2. Experimental Section

2.1. Reagents

Sodium nitrate ($NaNO_3$), potassium permanganate ($KMnO_4$), sodium dodecyl sulfate ($CH_3(CH_2)_{11}OSO_3Na$) (Merck), $TiCl_3$ (Merck), Sodium sulfate (Na_2SO_4), Hydrogen peroxide (H_2O_2) were purchased from Merck India.Methylamine (aqueous, 40 %), hydroiodic acid (aqueous, 57 %), ITO-coated glass, PbI_2&DMF, P3HT, Graphite powder were purchased from Sigma Aldrich India.

2.2. Synthesis of GO/TiO_2 Nanocomposites

2.2.1. Synthesis of Graphene Oxide

Graphene oxide was synthesized from natural graphite by using Hummers method [28]. Briefly, the method is graphite (5 g), $NaNO_3$ (2.5 g) and H_2SO_4 (120 mL) were mixed in a 500 mL beaker and the mixture was stirred vigorously in an ice bath for 30 min. Under constant stirring 15 g of $KMnO_4$ was added to the above suspension in a very controlled way so that the reaction temperature remains below 20 °C The mixture was kept under stirring for 12 h at room temperature, followed by the addition of 150 mL of distilled water and kept for 24 h under constant stirring. Then 50 mL of 30 % H_2O_2 was added to the mixture and stirred for another 6 h. Finally, the obtained product was washed with 5 % HCl and followed by distilled water so that the pH of the filtrate becomes 7 and dried in vacuum oven. The obtained graphene oxide was then dispersed and exfoliated in deionized water by using an ultrasonic bath for 40 min. The obtained graphene oxide suspension was then used for the synthesis of GO/TiO_2 composites.

2.2.2. Synthesis of Graphene Oxide/TiO_2 Composites

GO/TiO_2 composites were synthesized by a previously reported self-assembly method [29]. The graphene oxide suspension (1.3 gL^{-1}) as obtained was diluted with water and sodium dodecyl sulfate was added. To this mixture an aqueous solution of $TiCl_3$ (0.12 mol L^{-1}) was added and kept for 1 h under constant stirring. To the mixture, 10 ml of 0.6 M Na_2SO_4 solution and 5 mL of 1 wt % H_2O_2 solution was added and continued stirring for another 1 h at 90 °C. The final precipitates of the reactions were separated and washed with water and ethanol and then dried at 70 °C. Finally, the dried product was calcinated at 400°C for 2 h. Four sets of GO/TiO_2 nanocomposites viz. GO/TiO_2-A, GO/TiO_2-B, GO/TiO_2-C & GO/TiO_2-D having GO wt% of 0.25, 0.5, 1 & 2.5 respectively were synthesized by taking different amounts of graphene oxide, water and sodium dodecyl sulfate accordingly. The compositions of the prepared GO/TiO_2 nanocomposites are given in Table 1.

Table 1. The compositions of the prepared GO/TiO_2 nanocomposites.

TiO_2	GOTiO_2-A (0.25 wt%)	GOTiO_2-B (0.5 wt%)	GOTiO_2-C (1 wt%)	GOTiO_2-D (2.5 wt%)
GO (ml)	1.85	3.7	7.4	18.5
SDS (ml)	0.11	0.22	0.44	1.1

2.3. Synthesis of Methylammonium Iodide

Methylammonium iodide was synthesized by reacting 10 mL of methylamine (40 %, aqueous) and 10.8 mL of hydroiodic acid (57 %, aqueous) in a round bottom flask under constant stirring at 0 °C for 2 h. The product of the reaction was recovered by evaporating the solvents at 50 °C in a rotary evaporator. The obtained yellowish product was then washed three times with diethyl ether and dried. The whitish solid was collected and dried in a vacuum oven at 60 °C for 24 h [30].

2.4. Fabrication of the Perovskite Based Solar Cells

The ITO-coated glass substrate was cleaned before fabrication by ultrasonicating in detergent and deionized water followed by treating with boiled acetone and isopropanol and dried in air. There after a thin compact blocking layer of GO/TiO_2 composites were spin coated (2000 rpm for 60 seconds) onto the ITO film followed by annealed at 200 °C for 60 minutes. The synthesis of methylammonium lead iodide on the TiO_2 composite layer was carried out by spin coating the precursor solution at 2000 rpm for 60 seconds, which was prepared by dissolving the equimolecular mixture of CH_3NH_3I and PbI_2 in DMF under glove box conditions. Then the film was annealed at 100 °C for 45 minutes in a hotplate. The change of color of the film upon drying confirms the formation of methylammonium lead iodide. The P3HT layer was then spin coated by employing the P3HT/Chlorobenzene solution (20 mg mL^{-1}) at 1500 rpm for 45 seconds. Finally, the fabrication was completed by the counter electrode deposition on the prepared film by thermal evaporation of aluminium at a pressure of 2×10^{-5} Pa. The active area of the fabricated solar cells was assessed and found to be 0.04 cm^2. The photovoltaic characteristics of the fabricated solar cells were evaluated with the help of a Keithley SourceMeter and under illumination with a simulated (AM 1.5) solar light at 1 sun (100 mW cm^{-2}).

2.5. Measurements

2.5.1. X-ray Diffractometer (XRD)

The XRD measurements were carried out in a Rigaku X-ray diffractometer (Miniflex, UK) using CuKα (λ=0.154 nm) radiation at a scanning rate of 2° min^{-1} with an angle (2θ) ranging from 10° to 80° to study the structural characteristics of the synthesized nanocomposites.

2.5.2. Ultraviolet-visible (UV-vis) Spectroscopy

The optical property of MWCNT@TiO_2 nanocomposites were measured by using UV-Visible diffuse reflectance spectra in the range 200–800 nm using Shimadzu UV-2550 UV–visible spectrophotometer.

2.5.3. Scanning Electron Microscopy (SEM)

The surface morphologies of the prepared samples were studied by using a Jeol-JSM-6390L V scanning electron microscope at an accelerating voltage of 5-15 kV. The surface of the samples was Pt-coated before the scanning.

2.5.4. Transmission Electron Microscopy (TEM)

To study the distribution of the of particles within the nanocomposites, TEM analysis was done in a JEOL, JEM 2100 transmission electron microscope at an accelerating voltage of 200 kV.

2.6. Photovoltaic Test

The photocurrent voltage characteristics curves of the fabricated gel electrolyte based DSSCs were carried out using a 100 mW cm^{-2} xenon arc lamp in ambient atmosphere. The performance parameters of the fabricated devices i.e. the cell fill factor (FF) and cell power conversion efficiency (Η) were calculated by following Eqn. (1) and Eqn. (2) respectively.

$$FF = \frac{J_{max} \times V_{max}}{J_{sc} \times V_{oc}}, \quad (1)$$

$$\eta(\%) = \frac{FF \times J_{sc} \times V_{oc}}{P_{in}} \times 100, \quad (2)$$

where V_{max} and J_{max} are the maximum current density and voltage respectively at the point of maximum power of the photocurrent density versus voltage plot. J_{sc} is the short circuit current density (mA cm^{-2}), V_{oc} is the open circuit voltage (V) and P_{in} is the intensity of the incident white light.

3. Results and Discussions

3.1. UV-Visible Analysis

To study the optical property of the prepared GO/TiO_2 nanocomposites, UV-Visible analysis was recorded in the range of 200-800 nm and the spectra are shown in Fig. 1(a).

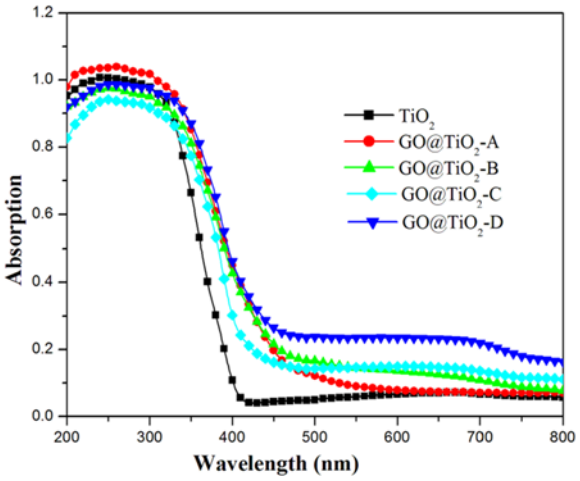

Fig. 1(a). UV-vis absorption spectra for TiO_2 and GO@TiO_2 nanocomposites.

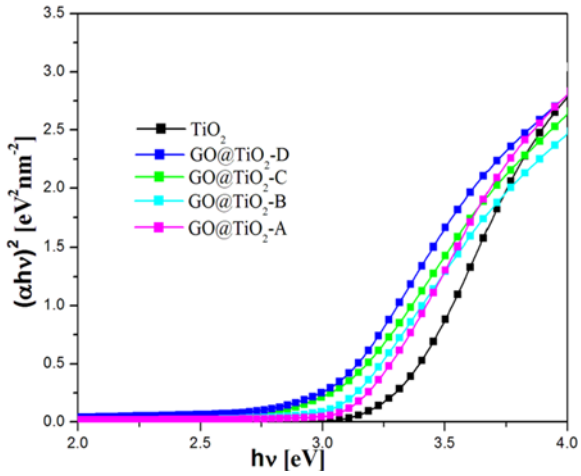

Fig. 1(b). Tauc's plot for optical band-gap calculation for TiO_2 and GO@TiO_2 nanocomposites.

All the nanocomposites shows the same absorption profile with a steep absorption edge at around 400 nm which are in the UV region of electromagnetic radiation which is caused by the bonding effect between GO and TiO_2. This kind of typical absorption in the UV region can be attributed to the intrinsic band gap absorption of TiO_2 resulting from the electron transition from the valance band to the conduction band of TiO_2 [31]. The presence of different amounts of GO in the nanocomposites significantly influences the optical properties of the material. The light absorption intensity for the GO/TiO_2 nanocomposites is observed to be increased with increasing GO content. In addition, a peak broadening is also noticed with increasing GO content.

Optical band gap calculations are carried out using the Tauc's relationship. The Tauc's equation for band gap calculations is described as,

$$(\alpha h\upsilon)^{1/n} = C(h\upsilon - E_g), \qquad (3)$$

where α is the absorption coefficient of the solid at a certain value of wavelength λ, h is the Planck's constant, C is the proportionality constant, υ is the frequency of light, E_g is the band gap energy and n=1/2 for direct allowed band gap. Fig. 1(b) shows the relationship of (αhυ)1/2 vs photon energy (hυ=1239/λ) for TiO_2 and also the GO/TiO_2 nanocomposites.

It shows that the band gap for the bare TiO_2 is 3.20 eV, whereas the band gaps for GO/TiO_2 nanocomposites are 3.06, 3.0, 2.89 & 2.84 eV corresponding to GO/TiO_2-A, GO/TiO_2-B, GO/TiO_2-C & GO/TiO_2-D respectively. This result in turn supports the qualitative observation of a red shift in the absorption edge of GO/TiO_2 nanocomposites as compared to the bare TiO_2. There is a possibility that some of the unpaired π electrons of GO can bonded with the free electrons present on the surface of TiO_2 nanoparticles to form Ti-O-C structure, resulting in the shifting of valence band and reduction in the band gap [32].

3.2. Powder X-ray Diffractometer (XRD)

The X-ray diffraction patterns for the GO and the GO/TiO_2 composites with different weight % of TiO_2 are shown in Fig. 2.

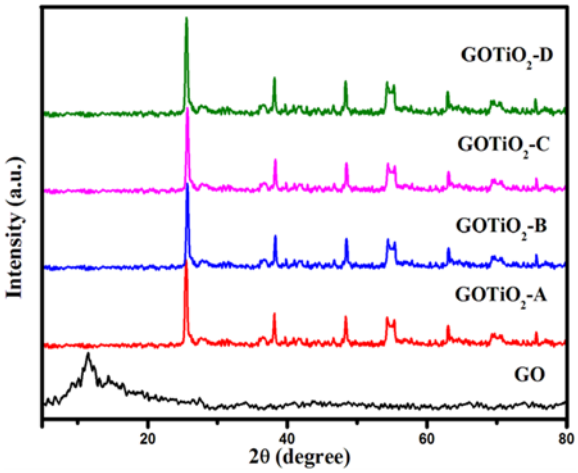

Fig. 2. XRD patterns of GO, GOTiO2-A, GOTiO2-B, GOTiO2-C & GOTiO2-D.

The neat GO exhibits a broad scattering peak at 2θ value of 11.5° corresponding to the plane (001) with an interlayer spacing of 7.43 Å [33]. The observed XRD patterns of the GO/TiO_2-A, GO/TiO_2-B, GO/TiO_2-C & GO/TiO_2-D represents the pure anatase phase of TiO_2 which is in turn confirmed by the reported JCPDs [34]. The reflection of (001) diffraction plane of GO is not observed in the XRD pattern of GO/TiO_2 composites which can be attributed to the fact that the regular stack of GO is disturbed by the intercalation of anatase TiO_2 [39, 41].

Thus, the XRD pattern of the GO/TiO_2 composites confirms the homogeneous distribution of anatse TiO_2

within the GO stacks. Furthermore, the existence of grapheme oxide in GO/TiO_2 nanocomposites can be clearly elucidated by Raman analysis.

3.3. Raman Spectra

Raman spectroscopy is a powerful tool to analyze the crystalline quality of the carbon and the defect mediated peaks. Fig. 3 shows the Raman spectrum of GO (inset graph in Fig. 3) and GO/TiO_2 nanocomposite. In the Raman spectrum first order dominant vibrational modes, D band 1351 cm^{-1} corresponds to the A1g symmetry mode of sp3 carbon indicates about the order or disorder in the system [34] and G band 1599 cm^{-1} corresponds to the vibrational mode of sp2 carbon provides information about the doubly degenerate E2g mode of the Brillonium zone centre [35].

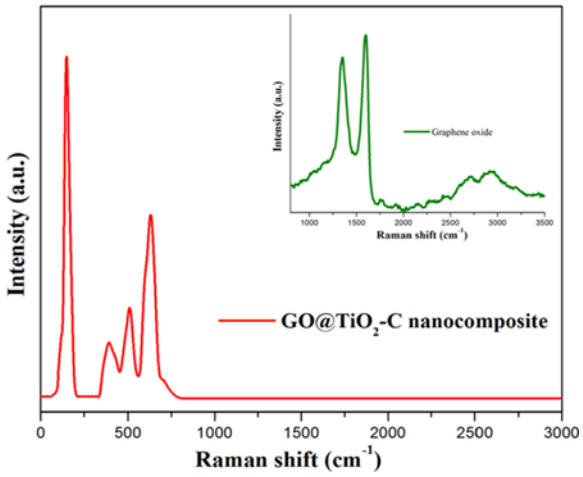

Fig. 3. Raman Spectra for GO and GO@TiO_2-C nanocomposite.

The second order vibrational bands, 2D1 & 2D2 arises at 2717.36 cm^{-1} & 2928.62 cm^{-1} respectively originates from a two phonon double resonance Raman process and provides information on the stacking order of graphene with no of layers and shows often a doublet with increasing no of graphene layers.

Another overtone weak band 2D/ is observed at 3194.23 cm^{-1} [36]. The intensity of G band is stronger than D band. In plane crystallite size, La can be calculated from the intensity ratio of the G band to the D band by using the formula, La= 4.4 (LG/LD). The obtained La value is 4.89, [38] from this it can be concluded that the sample contains highly disordered and randomly arranged graphene sheets. The shape of the 2D band is sensitive to the no of layers of graphene and chemical doping. When GO combines with TiO_2, the crystal structure of carbon changes obviously. There are four specific vibration modes are located at around 141 (E(g1)), 391 (B1g(1)), 514 (A1g+B1g(2)) & 634 cm^{-1} (Eg(2)) indicating the presence of the anatase phase of TiO_2 in the sample [39].

3.4. The Morphological Study of the Samples

3.4.1. SEM Analysis & EDX

The surface characteristics of the GO and the GO/TiO_2 nanocomposites are investigated with SEM analysis and the micrographs are shown in Fig. 4. For the pure GO a flat multilayered structure with stacked GO sheets is observed at higher magnifications (Fig. 4(a)) [40]. After introducing TiO_2 into the GO sheets (Fig. 4(c)), the SEM micrograph shows that the flat layered structure of the GO is disappeared and a rough surface morphology of the GO/TiO_2 nanocomposites is noticed. The change in the morphology of the GO/TiO_2 nanocomposites from the pure GO can be attributed to the successful incorporation of TiO_2 into the GO sheets. The energy dispersive X-ray spectrum (EDX) of the GO sheets and GO/TiO_2 nanocomposites indicates the successful distribution of TiO_2 nanoparticles into the GO sheets (Fig. 4(b) and Fig. 4(d)). The introduction of TiO_2 into the GO is confirmed from the elemental typical mapping images of titanium, oxygen and carbon.

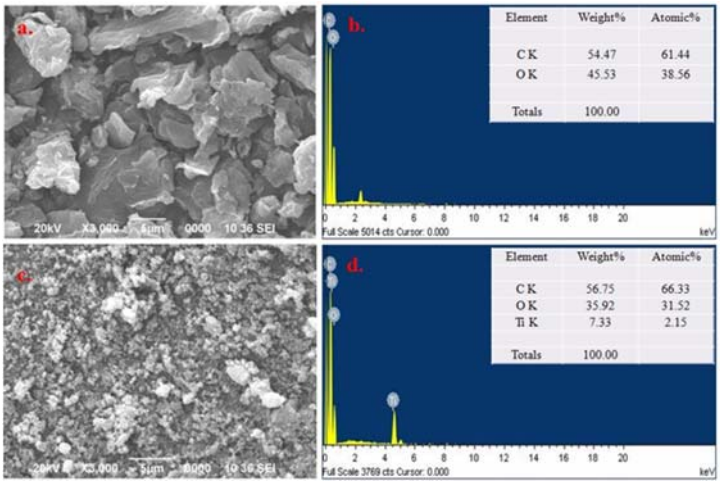

Fig. 4. SEM images & of EDX-spectrum of the GO (a & b) and GO@TiO_2-D nanocomposite (c & d).

3.4.2. TEM Analysis

The TEM micrographs of pure GO and GO/TiO_2 nanocomposites (GOTiO_2-D) are shown in Fig. 5. Layered and flake like structure with some wrinkles are observed in TEM micrographs of pure GO (Fig. 5(a)). The TEM micrographs of GO at high magnification (Fig. 5(b)) shows a completely amorphous and disordered structure [41]. A well dispersed TiO_2 nanoparticles on the surface of GO sheets are observed form the TEM micrographs of the nanocomposites Fig. 5(c & d). Moreover, the TiO_2 nanoparticles are homogeneously and closely dispersed on the GO sheets and thereby facilitate the electron transfer process in the solar cells.

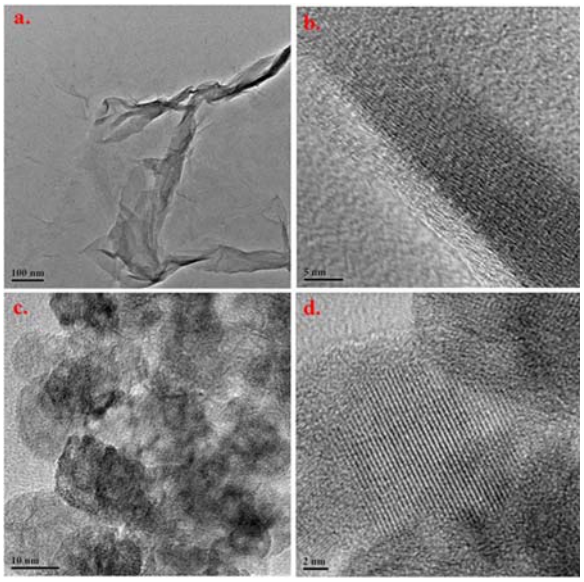

Fig. 5. TEM micrographs of the GO (a & b) and GO@TiO_2-D nanocomposite (c & d).

3.5. Photovoltaic Performance of the Fabricated Devices

Photovoltaic properties of the fabricated perovskite sensitized solar cells are examined by using different GO/TiO_2 composites having the device structure ITO/GO/TiO_2 nanocomposite/$CH_3NH_3PbI_3$/P3HT/Al. The photovoltaic performance parameters are summarized in Table 2 and the J-V curves are shown in Fig. 6.

Table 2. Device parameters of the GO/TiO_2 nanocomposite based solid state perovskite sensitized solar cells.

Sample	Jsc (mA cm^{-2})	Voc (V)	FF	PCE, η (%)
TiO_2 only	0.775	0.3656	0.426	0.121
GOTiO_2-A	1.785	0.453	0.496	0.401
GOTiO_2-B	2.771	0.505	0.434	0.608
GOTiO_2-C	3.812	0.507	0.546	1.055
GOTiO_2-D	5.286	0.5326	0.501	1.42

Here we investigate the performance of perovskite sensitized solar cells using different concentrations of GO in the TiO_2 nanocomposite which acts as the n-type charge collection electrode.

The mean solar cell performance parameters of the fabricated devices were measured under stimulated 100 mW cm^{-2} sunlight. We observed that, there is a clear enhancement in the device parameter of the fabricated devices by the introduction of GO in the TiO_2. By using the TiO_2 nanoparticles the short circuit current density (J_{sc}) and fill factor are found to be 0.81 mA cm^{-2} and 0.30 respectively. With increasing GO concentration in the electron collection layer both the Jsc and FF increases upto 4.65 mA cm^{-2} and 0.56 respectively.

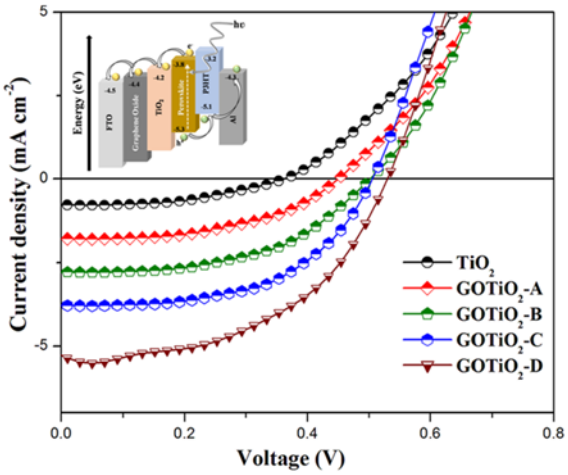

Fig. 6. Photocurrent density versus voltage plot of TiO_2, GOTiO_2-A, GOTiO_2-B, GOTiO_2-C & GOTiO_2-D.

Enhancement in the efficiency of the devices with the incorporation of the GO into TiO_2 can be described from the facts that GO has a work function that lies in-between that of the ITO and the conduction band of TiO_2. As a result of which GO containing TiO_2 acts as a better electron collector as compared to TiO_2 alone by reducing the energy barrier at the material interfaces and also due to the superior charge mobility of GO. In this device structure the organometal halide perovskite, methylammonium lead iodide acts as the absorber, coated upon the electron collection layer. While the interdigitated P3HT collects the holes and transfers them to the back electrode.

4. Conclusions

This work successfully demonstrates the application of two different combinations of graphene oxide with organo metal halide perovskite. Also the study of the synthesized GO/TiO_2 nanocomposites showed that with increase in the GO content there occurs enhancement in the optical properties. The homogeneous distribution of TiO_2 nanoparticles

within the GO stacks is confirmed by the XRD analysis, which can be further confirmed from the SEM and TEM micrographs that TiO_2 nanoparticles are homogeneously and closely dispersed on the GO sheets. The purpose of using GO/TiO_2 nanocomposites in perovskite sensitized solar cells is also beneficial as it behaves well as the electron collection layer. As a result of which there is a significant enhancement in the photovoltaic parameters of the solar cells. It has also been spotted form the study that the incorporation of high concentration of GO in the nanocomposite results in the enhancement of the device parameters i.e. VOC, JSC and PCE due to the superior charge mobility of GO.

Acknowledgements

The authors would like to acknowledge University Grant Commission (UGC), India, for providing Junior Research Fellowship (JRF) under Maulana Azad National Fellowship (MANF) scheme for financial assistance and Department of Electronics and Information Technology, Ministry of Communications & Information Technology India for their financial support (Sanction No. 1 (11)/2012-EMCD dated 05-03-2013). Authors are also very much grateful to SAIF, North-Eastern Hill University, India and SAIC, Tezpur University, India for analytical support.

References

[1]. M. A. Green, K. Emery, Y. Hishikawa, W. Warta, E. D. Dunlop, Solar cell efficiency tables (version 41), *Progress in Photovoltaics: Research and Applications,* Vol. 21, Issue 1, 2013, pp. 1-11.

[2]. P. Jackson, D. Hariskos, E. Lotter, S. Paetel, R. Wuerz, R. Menner, W. Wischmann, M. Powalla, New world record efficiency for Cu(In,Ga)Se_2 thin-film solar cells beyond 20 %, *Progress in Photovoltaics: Research and Applications,* Vol. 19, Issue 7, 2011, pp. 894-897.

[3]. A. Nozik, Quantum dot solar cells, *Physica E: Low-dimensional Systems and Nanostructures*, Vol. 14, Issue 1-2, 2002, pp. 115-120.

[4]. B. Oregan, M. Gratzel, A Low-cost, High-efficiency Solar Cell Based on Dye-sensitized Colloidal TiO_2 Films, *Nature*, Vol. 353, No. 6346, 1991, pp. 737-740.

[5]. G. Yu, J. Gao, J. C. Hummelen, F. Wudl, A. J. Heeger, Polymer Photovoltaic Cells: Enhanced Efficiencies via a Network of Internal Donor-Acceptor Heterojunctions, *Science*, Vol. 270, Issue 5243, 1995, pp. 1789-1791.

[6]. M. M. Lee, J. Teuscher, T. Miyasaka, T. N. Murakami, H. J. Snaith, Efficient hybrid solar cells based on meso-superstructured organometal halide perovskites, *Science*, Vol. 338, Issue 6107, 2012, pp. 643-647.

[7]. W. Zhang, M. Saliba, S. D. Stranks, Y. Sun, X. Shi, U. Wiesner, H. J. Snaith, Enhancement of Perovskite-Based Solar Cells Employing Core–Shell Metal Nanoparticles, *Nano Letters*, Vol. 13, Issue 9, 2013, pp. 4505-4510.

[8]. A. Kojima, M. Ikegami, K. Teshima, T. Miyasaka, Highly Luminescent Lead Bromide Perovskite Nanoparticles Synthesized with Porous Alumina Media, *Chemistry Letters*, Vol. 41, Issue 4, 2012, pp. 397-399.

[9]. C. R. Kagan, D. B. Mitzi, C. D. Dimitrakopoulos, Organic-Inorganic Hybrid Materials as Semiconducting Channels in Thin-Film Field-Effect Transistors, *Science*, Vol. 286, Issue 5441, 1999, pp. 945-947.

[10]. A. Kojima, K. Teshima, Y. Shirai, T. Miyasaka, Organometal Halide Perovskites as Visible-Light Sensitizers for Photovoltaic Cells, *Journal of the American Chemical Society,* Vol. 131, Issue 17, 2009, pp. 6050-6051.

[11]. J. Burschka, N. Pellet, S. J. Moon, R. Humphry-Baker, P. Gao, M. K. Nazeeruddin, M. Grätzel, Sequential deposition as a route to high-performance perovskite-sensitized solar cells, *Nature*, Vol. 499, 2013, pp. 316-319.

[12]. J. H. Heo, S. H. Im, J. H. Noh, T. N. Mandal, C. Lim, J. A. Chang, Y. H. Lee, H. Kim, A. Sarkar, M. K. Nazeeruddin, M. Grätzel, S. I. Seok, Efficient inorganic–organic hybrid heterojunction solar cells containing perovskite compound and polymeric hole conductors, *Nature Photonics*, Vol. 7, 2013, pp. 486-491.

[13]. J. H. Noh, S. H. Im, J. H. Heo, T. N. Mandal, S. I. Seok, Chemical Management for Colorful, Efficient, and Stable Inorganic–Organic Hybrid Nanostructured Solar Cells, *Nano Letters*, Vol. 13, Issue 4, 2013, pp. 1764-1769.

[14]. H. S. Kim, C. R. Lee, J. H. Im, K. B. Lee, T. Moehl, A. Marchioro, S. J. Moon, R. Humphry-Baker, J. H. Yum, J. E. Moser, M. Grätzel, N. G. Park, Lead iodide perovskite sensitized all-solid-state submicron thin film mesoscopic solar cell with efficiency exceeding 9 %, *Scientific Reports*, Vol. 2, 2012, pp. 1-7.

[15]. V. Thavasi, V. Renugopalakrishnan, R. Jose, S. Ramakrishna, Controlled electron injection and transport at materials interfaces in dye sensitized solar cells, *Materials Science and Engineering: R Reports*, Vol. 63, Issue 3, 2009, pp. 81-99.

[16]. B. S. Ong, C. S. Li, Y. N. Li, Y. L. Wu, R. Loutfy, Stable, Solution-Processed, High-Mobility ZnO Thin-Film Transistors, *Journal of the American Chemical Society*, Vol. 129, Issue 10, 2007, pp. 2750-2751.

[17]. C. Lee, X. Wei, J. W. Kysar, J. Hone, Measurement of the Elastic Properties and Intrinsic Strength of Monolayer Graphene, *Science*, Vol. 321, Issue 5887, 2008, pp. 385-388.

[18]. S. Chen, Q. Wu, C. Mishra, J. Kang, H. Zhang, K. Cho, W. Cai, A. A. Balandin, R. S. Ruoff, Thermal conductivity of isotopically modified graphene, *Nature Materials*, Vol. 11, No. 3, 2012, pp. 203-207.

[19]. A. A. Balandin, S. Ghosh, W. Bao, I. Calizo, D. Teweldebrhan, F. Miao, C. N. Lau, Superior Thermal Conductivity of Single-Layer Graphene, *Nano Letters*, Vol. 8, Issue 3, 2008, pp. 902-907.

[20]. J. H. Chen, C. Jang, S. Xiao, M. Ishigami, M. S. Fuhrer, Intrinsic and extrinsic performance limits of graphene devices on SiO_2, *Nature Nanotechnology*, Vol. 3, 2008, pp. 206-209.

[21]. A. K. Geim, K. S. Novoselov, The rise of graphene, *Nature Materials*, Vol. 6, No. 3, 2007, pp. 183-191.

[22]. Q. Y. He, S. X. Wu, Z. Y. Yin, H. Zhang, Graphene-based electronic sensors, *Chemical Science*, Vol. 3, 2012, pp. 1764-1772.
[23]. X. Huang, Z. Zeng, Z. Fan, J. Liu, H. Zhang, Graphene-Based Electrodes. *Advanced Materials*, Vol. 24, Issue 45, 2012, pp. 5979-6004.
[24]. Z. Yin, J. Zhu, Q. He, X. Cao, C. Tan, H. Chen, Q. Yan, H. Zhang, Graphene-Based Materials for Solar Cell Applications, *Advanced Energy Materials,* Vol. 4, Issue 1, 2014, pp. 1-9.
[25]. Y. Zhang, Z. R. Tang, X. Fu, Y. J. Xu, Engineering the Unique 2D Mat of Graphene to Achieve Graphene-TiO_2 Nanocomposite for Photocatalytic Selective Transformation: What Advantage does Graphene Have over Its Forebear Carbon Nanotube?, *ACS Nano*, Vol. 5, Issue 9, 2011, pp. 7426-7435.
[26]. C. Zhu, S. Guo, P. Wang, L. Xing, Y. Fang, Y. Zhai, S. Dong, One-pot, water-phase approach to high-quality graphene/TiO_2 composite nanosheets, *Chemical Communications*, Vol. 46, No. 38, 2010, pp. 7148-7150.
[27]. Y. Liang, H. Wang, H. S. Casalongue, Z. Chen, H. Dai, TiO_2 Nanocrystals Grown on Graphene as Advanced Photocatalytic Hybrid Materials, *Nano Research*, Vol. 3, Issue 10, 2010, pp. 701-705.
[28]. W. S. Hummers, R. E. Offeman, Preparation of Graphitic Oxide, *Journal of the American Chemical Society*, Vol. 80, Issue 6, 1958, pp. 1339.
[29]. D. H. Wang, D. W. Choi, J. Li, Z. G. Yang, Z. M. Nie, R. Kou, D. H. Hu, C. M. Wang, L. V. Saraf, J. G. Zhang, Self-Assembled TiO_2-Graphene Hybrid Nanostructures for Enhanced Li-Ion Insertion, *ACS Nano*, Vol. 3, Issue 4, 2009, pp. 907-914.
[30]. L. Etgar, P. Gao, Z. Xue, Q. Peng, A. K. Chandiran, B. Liu, M. K. Nazeeruddin, M. Grätzel, Mesoscopic $CH_3NH_3PbI_3/TiO_2$ Heterojunction Solar Cells, *Journal of the American Chemical Society*, Vol. 134, Issue 42, 2012, pp. 17396-17399.
[31]. K. Dai, L. Lu, Q. Liu, G. Zhu, Q. Liua, Z. Liua, Graphene oxide capturing surface-fluorinated TiO_2 nanosheets for advanced photocatalysis and the reveal of synergism reinforce mechanism, *Dalton Transactions*, Vol. 43, Issue 5, 2014, pp. 2202-2210.
[32]. Y. W. Jun, M. F. Casula, J. H. Sim, S. Y. Kim, J. Cheon, A. P. Alivisatos, Surfactant-Assisted Elimination of a High Energy Facet as a Means of Controlling the Shapes of TiO_2 Nanocrystals, *Journal of the American Chemical Society*, Vol. 125, Issue 51, 2003, pp. 15981-15985.
[33]. P. G. Liu, K. C. Gong, P. Xiao, M. Xiao, Preparation and characterization of poly(vinyl acetate)-intercalated graphite oxide nanocomposites, *Journal of Materials Chemistry*, Vol. 10, No. 4, 2000, pp. 933-935.
[34]. Y. W. Jun, M. F. Casula, J. H. Sim, S. Y. Kim, J. Cheon, A. P. Alivisatos, Surfactant-Assisted Elimination of a High Energy Facet as a Means of Controlling the Shapes of TiO_2 Nanocrystals, *Journal of the American Chemical Society,* Vol. 125, Issue 51, 2003, pp. 15981-15985.
[35]. J. Lu, J. X. Yang, J. Wang, A. Lim, S. Wang, K. P. Loh, One-pot synthesis of fluorescent carbon nanoribbons, nanoparticles, and graphene by the exfoliation of graphite in ionic liquids, *ACS Nano*, Vol. 3, Issue 8, 2009, pp. 2367-2375.
[36]. A. C. Ferrari, J. C. Meyer, V. Scardaci, C. Casiraghi, M. Lazzeri, F. Mauri, S. Piscanec, D. Jiang, K. S. Novoselov, S. Roth, A. K. Geim, Raman Spectrum of Graphene and Graphene Layers, *Physical Review Letters*, Vol. 97, No. 18, 2006, pp. 187401-187404.
[37]. M. A. Pimenta, G. Dresselhaus, M. S. Dresselhaus, L. A. Cancado, A. Jorio, R. Saito, Studying disorder in graphite-based systems by Raman spectroscopy, *Physical Chemistry Chemical Physics*, Vol. 9, 2007, pp. 1276-1290.
[38]. A. C. Ferrari, Raman spectroscopy of graphene and graphite: Disorder, electron–phonon coupling, doping and nonadiabatic effects, *Solid State Communications*, Vol. 143, 2007, pp. 47-57.
[39]. Y. Lei, L. D. Zhang, J. C. Fan, Fabrication, characterization and Raman study of TiO_2 nanowire arrays prepared by anodic oxidative hydrolysis of $TiCl_3$, *Chemical Physics Letters*, Vol. 338, Issue 4-6, 2001, pp. 231-236.
[40]. L. L. Zhang, S. Zhao, X. N. Tian, X. S. Zhao, Layered Graphene Oxide Nanostructures with Sandwiched Conducting Polymers as Supercapacitor Electrodes, *Langmuir*, Vol. 26, Issue 22, 2010, pp. 17624-17628.
[41]. G. Wang, J. Yang, J. Park, X. Gou, B. Wang, H. Liu, J. Yao, Facile Synthesis and Characterization of Graphene Nanosheets, *The Journal of Physical Chemistry C,* Vol. 112, Issue 22, 2008, pp. 8192-8195.

Sensors & Transducers, Vol. 210, Issue 3, March 2017, pp. 17-19

www.sensorsportal.com

Sensors & Transducers

Published by IFSA Publishing, S. L., 2017
http://www.sensorsportal.com

In-situ Elevated Temperature Mechanical Performance of MWCNT/epoxy Nanocomposite

*** Bhanu Pratap Singh, Dinesh Kumar Rathore, Sarat Chandra Mohanty, Rajesh Kumar Prusty and Bankim Chandra Ray**

Composite Materials Group, Metallurgical and Materials Engineering Department,
National Institute of Technology, Rourkela, India-769008
* E-mail: bpsingh208021@gmail.com

Received: 9 January 2017 /Accepted: 3 March 2017 /Published: 31 March 2017

Abstract: The present investigation has been focused on the effects of multi-walled carbon nanotube (MWCNT) addition on the mechanical performance of epoxy under different in-service elevated temperature environments. Room temperature flexural test results revealed that addition of 0.1 wt. % MWCNT into epoxy resin resulted in modulus and strength enhancement of 21 % and 9 % respectively. With increase in service temperature, significant decrement in both modulus and strength was noticed for both materials (neat epoxy and MWCNT/epoxy nanocomposite), but the rate of degradation was found to be quite drastic for the nanocomposite. At 90 °C temperature, the CNT/epoxy nanocomposite exhibited inferior modulus and strength, which are 41 % and 59 % lower than neat epoxy respectively. The variation trend in elastic modulus with temperature obtained from both flexural testing and DMA for both these materials was also analyzed. It was found that addition of 0.1 % CNT in the epoxy reduced the glass transition temperature by about 16°C.

Keywords: Multi-walled carbon nanotube (MWCNT), Nanocomposite

1. Introduction

Replication of the unique properties of nano-fillers in the polymer is the key target to manipulate the mechanical, thermal and/or electrical properties of polymer based materials. In the last couple of decades, many nano-sized materials have been successfully synthesized, but none of them have been globally acknowledged as much as carbon nano-tube (CNT). The motivation behind reinforcing a polymer by CNT is due to its extra-ordinary strength (as high as 22 GPa), modulus (order of 1 TPa), low density and extremely high aspect ratio (500 - 100000). The potential exploitation of CNT for achieving the desirable mechanical properties lies in:

1) Good interfacial bonding between the polymer and CNT;

2) Uniform dispersion to avail high interfacial area to facilitate effective stress transfer.

Many research articles have reported the beneficial mechanical performance of CNT reinforced polymers at room temperature [1-2]. Addition of CNT into polymeric materials has shown remarkably improved cryogenic mechanical performance [3-4]. But, to the best of authors' knowledge there is a dearth of open literature reporting the elevated temperature performance of CNT/polymer nanocomposites. "Whether the strength enhancement mechanism still remains valid at elevated temperature environment", this question has been tried to answer in the current article.

2. Experimental Details

The polymer used in the current study was a Diglycidyl ether of Bisphenol A type epoxy resin with Triethylene tetra amine as hardener, which were manufactured by Atul Industries, India. The MWCNT (6-9 nm outer diameter with 5 μm length) used for reinforcing the epoxy resin was purchased from Sigma-Aldrich. 0.1 wt. % MWCNT (w.r.t. epoxy) was initially weighed and then mixed in 150 ml acetone. This acetone/MWCNT mixture was then stirred at 1000 rpm for 30 minutes followed by 30 minutes of ultra-sonication. The mixture was then transferred to a flask containing epoxy resin which was preheated at 70°C for 30 minutes. This epoxy/acetone/MWCNT mixture was then stirred at 70°C temperature and 1000 rpm till complete evaporation of acetone is ensured. The remaining epoxy/MWCNT suspension is then ultra-sonicated for 1 hour. After sonication this suspension was kept in vacuum for 18 hours. Required amount of hardener (10 wt. % of resin as specified by the manufacturer) was then added to the suspension and mixed gently using a glass rod for 2 minutes and then slowly poured into the moulds of appropriate dimensions. Neat epoxy was also poured into moulds only after mixing required amount of hardener. All the moulds were then again placed in vacuum for 10 minutes followed by room temperature curing for 24 hours. The solidified samples were then taken out from the moulds and fine polished to make all the surfaces smooth. Post-curing of all the samples were then carried out in an oven at 120 °C for 6 hours. Flexural test was then performed on neat epoxy and CNT/epoxy nanocomposites in an Instron 5967 attached with an environmental chamber at various temperatures (room temperature (30 °C), 70 °C and 90°C) at a loading speed of 1 mm/min as per ASTM D790. Thermo-mechanical properties of both epoxy and CNT/epoxy nanocomposite was evaluated by Netzsch DMA 242E in a temperature range of 40-170 °C at a heating rate of 5°C/min and 1 Hz frequency. Fractured surfaces after flexural testing were then observed using scanning electron microscope (SEM).

3. Results and Discussion

The results of flexural tests are shown in Fig. 1. Results revealed that addition of 0.1 wt. % CNT in epoxy resulted 9 % and 21 % enhancement in strength and modulus, when tested at room temperature. But, it can also be seen from Fig. 1(a) that the failure strain is reduced by 20 % due to this addition of CNT into epoxy. With increase in temperature both modulus and strength of both the materials continue to decrease, but interestingly the rate of decrement is relatively higher for the nanocomposite than the neat epoxy. At 70 °C temperature, the relative decrement in strength for epoxy and CNT/epoxy nanocomposite was 21 % and 41 % respectively compared to their respective room temperature strength. Similarly, the modulus was found to be reduced by 5 % and 20 % for epoxy and CNT/epoxy nanocomposite respectively. When the test was performed at 90 °C temperature, the nanocomposite was found to exhibit strength and modulus which were 59 % and 41 % lower than neat epoxy. The reduction in strength and modulus for neat epoxy can be explained in terms of polymer softening, increased polymer chain mobility which results in lower resistance to applied load. Further, the rate of this degradation is more as the polymer approaches its glass transition temperature (T_g). In comparison to neat epoxy, the nanocomposite exhibits fairly high rate of degradation due to the differential co-efficient of thermal expansion of CNT ($0.73–1.49\times10^{-5}$ K^{-1} [3]) and epoxy (6.2×10^{-5} K^{-1} [5]). Hence, the radial expansion of epoxy is faster than CNT which induces a residual stress at the CNT/epoxy interface. This residual stress increases with temperature and/or external stress and ultimately gets relieved by interfacial debonding which reduces the strength of the material drastically.

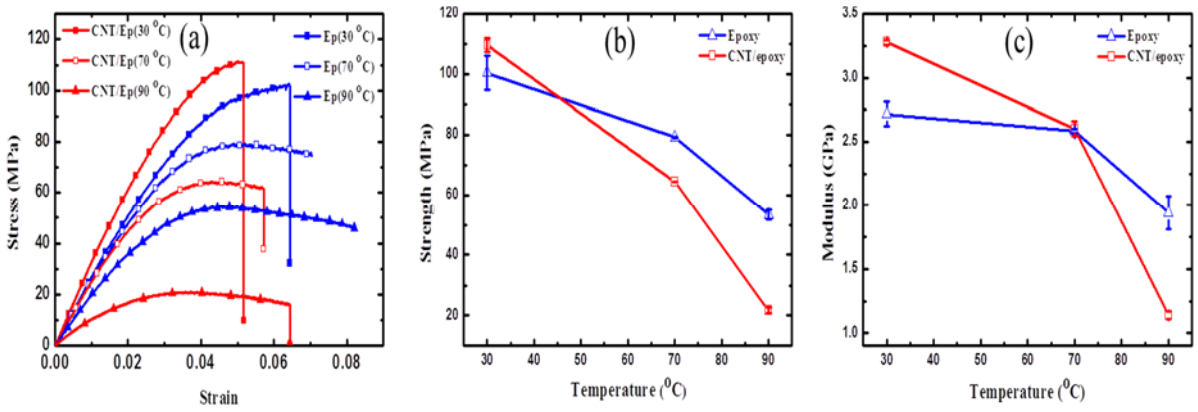

Fig. 1. Variation in flexural (a) stress-strain plots, (b) strength and (c) modulus of epoxy (Ep) and CNT/epoxy nanocomposite (CNT/Ep) at various in-situ elevated temperature.

From Fig. 2, it can be seen that the storage modulus (E′) also shows the similar trend as that of flexural modulus with temperature. At a lower temperature the nanocomposite exhibits higher E′ than the neat epoxy, but after a temperate of 90 °C, epoxy exhibits a higher E′ than nanocomposite. The difference in magnitude of the elastic modulus and transition temperature obtained from flexural testing and DMA might be attributed towards their differential thermal history. The T_g (obtained from the onset of E′-temperature plot) for the nanocomposite is 16 °C lower than the neat polymer. This might be due to penetration of the finely dispersed CNTs into the inter-chain region of the resin which hinders formation of crosslinks during curing.

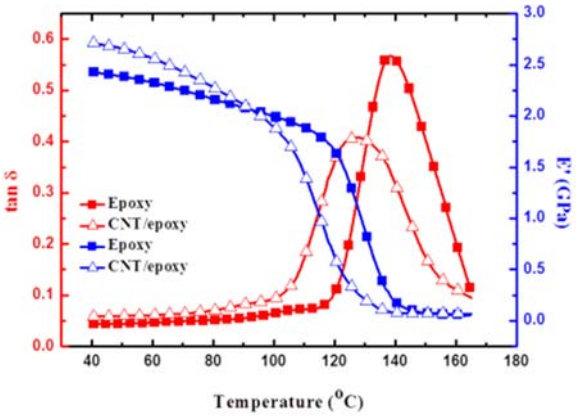

Fig. 2. Variation in termomechanical behavior of epoxy and CNT/epoxy nanocomposites.

Mirror, mist and hackle zones [6] were observed as shown in Fig. 3 in both materials at all testing temperatures. Fig. 3(a) and Fig. 3(b) represent the hackle zones of neat epoxy and nanocomposite respectively for room temperature tested samples showing distinct appearance. The mist zone of epoxy and nanocomposite at 70 °C is shown in Fig. 3(c) and Fig. 3(d) respectively.

4. Conclusions

From the present investigation it can be concluded that CNT reinforced epoxy remains a suitable candidate over neat epoxy at room temperature, but beyond a critical temperature a negative reinforcement effect was noticed. This confirms that the positivity of the CNT/epoxy nanocomposite over neat epoxy is in-service temperature dependent.

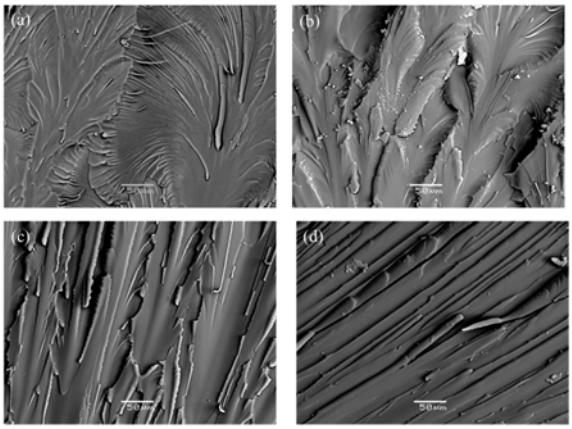

Fig. 3. SEM micro-graph of fractured surfaces of (a) epoxy and (b) CNT/epoxy nanocomposite at room temperature, (c) epoxy and (d) CNT/epoxy nanocomposite at 70 °C.

References

[1]. Schadler L. S., Giannaris S. C., Ajayan P. M., Load Transfer in Carbon Nanotube Epoxy Composites, *Applied Physics Letters*, Vol. 73, No. 6, 1998, pp. 3842-3844.

[2]. Kathi J., Rhee K.-Y., Lee J. H., Effect of chemical functionalization of multi-walled carbon nanotubes with 3-aminopropyltriethoxysilane on mechanical and morphological properties of epoxy nanocomposite, *Composites Part A: Applied Science and Manufacturing*, Vol. 40, No. 6, 2009, pp. 800–809.

[3]. Chen Z.-K., Yang J.-P., Ni Q.-Q., Fu S.-Y., Huang Y.-G., Reinforcement of epoxy resins with multi-walled walled carbon nanotubes for enhancing cryogenic mechanical properties, *Polymer*, Vol. 50, No. 19, 2009, pp. 4753–4759.

[4]. Prusty R. K., Rathore D. K., Shukla M. J., Ray B. C., Flexural behaviour of CNT-filled glass/epoxy composites in an in-situ environment emphasizing temperature variation, *Composites Part B*: *Engineering*, Vol. 83, 2015, pp. 166–174.

[5]. Huang C. J., Fu S. Y., Zhang Y. H., Lauke B., Li L. F., Ye L., Cryogenic properties of SiO_2/epoxy nanocomposites, *Cryogenics*, Vol. 45, No. 6, 2005, pp. 450–454.

[6]. Greenhalgh E. S., Failure analysis and fractography of polymer composites, *Elsevier*, 2009.

Sensors & Transducers, Vol. 210, Issue 3, March 2017, pp. 20-28

www.sensorsportal.com

Sensors & Transducers

Published by IFSA Publishing, S. L., 2017
http://www.sensorsportal.com

Possible Lead Free Nanocomposite Dielectrics for High Energy Storage Applications

*** Srinivas Kurpati and Ramesh Singampalli**
Department of Physics, GITAM University, Nagadenahalli, Bengaluru-562163, India
Tel.: 080-28098000, fax: 080-28098002
* E-mail: srinkura@gmail.com

Received: 9 January 2017 /Accepted: 3 March 2017 /Published: 31 March 2017

Abstract: There is an increasing demand to improve the energy density of dielectric capacitors for satisfying the next generation material systems. One effective approach is to embed high dielectric constant inclusions such as lead zirconia titanate in polymer matrix. However, with the increasing concerns on environmental safety and biocompatibility, the need to expel lead (Pb) from modern electronics has been receiving more attention. Using high aspect ratio dielectric inclusions such as nanowires could lead to further enhancement of energy density. Therefore, the present brief review work focuses on the feasibility of development of a lead-free nanowire reinforced polymer matrix capacitor for energy storage application. It is expected that Lead-free sodium Niobate nanowires ($NaNbO_3$) and Boron nitride will be a future candidate to be synthesized using simple hydrothermal method, followed by mixing them with polyvinylidene fluoride (PVDF)/ divinyl tetramethyl disiloxanebis (benzocyclobutene) matrix using a solution-casting method for Nanocomposites fabrication. The energy density of $NaNbO_3$ and BN based composites are also be compared with that of lead-containing ($PbTiO_3$/PVDF) Nano composites to show the feasibility of replacing lead-containing materials from high-energy density dielectric capacitors. Further, this paper explores the feasibility of these materials for space applications because of high energy storage capacity, more flexibility and high operating temperatures. This paper is very much useful researchers who would like to work on polymer nanocomposites for high energy storage applications.

Keywords: Dielectrics, Polymers, Nanowires, Nanocomposites, Energy storage devices.

1. Introduction

The development of high energy density storage systems with reduced size is highly demanded in many applications, e.g., consumer electronics, space-based and land-based pulsed power applications, commercial defibrillators, etc. [1]. The electrostatic energy density that can be stored in a material is directly proportional to its dielectric permittivity at the local field and the square of the operational electric field. This necessitates that modern materials for high energy density should not only posses high dielectric permittivity, but also provide high operational electric fields with low dissipation factors. The apparent absence of one single-phase material exhibiting such a combination of properties emphasizes the need to integrate two or more materials with complimentary properties, thus, in turn, creating a composite with performance far better than that of its constituents. Ferroelectric oxides have high dielectric permittivity, but suffer from low dielectric strengths. Polymers, on the other hand, have high breakdown field tolerances, but are limited to low dielectric constants. A diphasic composite consisting of these two could provide a material with high dielectric constant [2] and high breakdown field, affording high storage density for a

given thickness. The properties of such composites can be tailored through material selection and composition, as well as through percolation and connectivity of phases present within [3-4]. Recent efforts to obtain high energy density materials have primarily focused on randomly dispersed nano- or micron-sized ceramic particulates in a polymer matrix.

The dielectric properties of nanocomposites have been found to be better in comparison to microcomposites and neat polymers. Various proposed models with some experimental evidence have attributed this property enhancement to the interfacial effects related to filler-polymer interactions in nanocomposites. In this regard, this paper has focused on finding the ways to enhance the energy storage capacity of polymer nanocomposites by concentrating on interfacial interactions between polymer and filler particle surfaces within an applied field. The main objectives of this research paper are:

1) To modify the surface of nano-sized particles ceramic particles with bifunctional organophosphate coupling agents so as to achieve a covalent interface when used within an epoxy polymer matrix composites.

2) To study the influence of covalent interface on electrical properties, especially dielectric breakdown strength of polymer nanocomposite dielectrics compared to physically adsorbed interface based nanodielectrics and neat polymer.

3) To study the influence of electronic nature of surface functionalized filler particles on dielectric properties of their composites in epoxy. The electron donating and electron accepting functional groups were used as surface modifying reagents, attached via an organophosphate ligand on to the surface of filler particles.

4) To enhance the energy density of polymer nanocomposites by compromising the decrease in dielectric breakdown strength with increase in permittivity at higher filler particle volume concentration [5].

It was found that interface layers in the nanocomposites might be more conductive than the polymer matrix, which mitigated the space charge accumulation and field concentration by fast charge dissipation. Zhang and coworkers demonstrated large enhancement in the electric energy density and electric displacement level in the nanocomposites of P(VDF-TrFE-CFE) terpolymer/ZrO_2 nanoparticles [6]. Through the interface effect, the presence of 1.6 vol% of ZrO_2 nanoparticles raised the maximum electric displacement D from 0.085 C/m^2 under 400 MV/m in the neat terpolymer to more than 0.11 C/m^2 under 300 MV/m in the nanocomposites. The dielectric nanocomposites composed of P(VDF-TrFECTFE) [7] and surface-functionalized TiO2 nanoparticles with comparable dielectric permitivities and homogeneous nanoparticle dispersions were prepared [8]. It was found that the presence of the nanoscale filler favors the formation of smaller crystalline domains and a higher degree of crystallinity in the polymer. In drastic contrast to their weak-field dielectric behavior, substantial enhancements in electric displacement and energy density at high electric fields have been demonstrated in the nanocomposites.

Miniaturization and the current need for high-power density, high voltage capacitors and power-storage devices has stimulated a new field of research interest in polymer nanocomposites as composite dielectrics (C) [9-15]. By incorporating high permittivity inorganic nanoparticles into a polymer matrix with low dielectric loss and high breakdown strength, one may be able to develop new composite materials that have improved dielectric properties, dielectric strength, permittivity and dielectric losses, and retain unique attributes of polymers.

The most distinctive feature of polymer nanocomposites in comparison with conventional microcomposites is the participation of interfacial surface area between the nanoparticles and the polymer matrix. The smaller the size of the embedded nanoparticles, the larger the surface area to volume ratio, which leads to larger interfacial regions [16-17]. For filler nanoparticles with modest loadings, the surface area associated with the internal interfaces becomes dominant in nanocomposites compared to microcomposites [18]. The properties of these interface areas may differ substantially from those of both the base polymer matrix and the nanoparticle material [18-19]. From literature, polymer nanocomposites with metal oxide nanoparticle fillers exhibited enhanced electrical breakdown strength and voltage endurance compared to their unfilled or micrometer sized particle filled counterparts.

While the use of nanowire could lead to higher energy density capacitor, most of the high dielectric constant inclusions used has lead- (Pb-) containing materials, such as PZT and PLZT, which make the resulting nanocomposites toxic and not compatible with biological applications. Expelling lead from commercial applications and materials such as solders, glass, and gasoline has been receiving extensive attention because of the concerns regarding its toxicity. Therefore, our present work focuses on the development of a lead-free nanowire reinforced polymer capacitor with comparable dielectric properties to lead-containing capacitors.

The dielectric constant and breakdown strength of nanocomposites with volume fractions ranging from 5 % to 30 % were experimentally tested to determine the energy densities of both nanocomposites. Testing results have shown that the NNO/PVDF composites have higher dielectric constants, lower dielectric loss, and comparable energy density. Therefore, this may demonstrate the feasibility of developing lead-free high-energy polymer capacitors to ultimately replace lead-containing ones. Further, BN nanosheets are thus envisaged to be one of the best fillers in composites owing to the highly insulating and thermoconductive properties. The fabricated PMMA/ BN composite plastics are, thus, envisaged to be valuable for diverse functional applications in many fields, especially for

the new-generation thermoconductive insulating long-lifetime packaging materials [21].

2. Role of Interface

Incorporation of nanoparticles into polymer matrix for developing nanocomposites, which has produced interesting results in last few years, has led researchers to investigate mechanisms for the improved dielectric properties. Researchers have emphasized the critical role of the interfacial region and present hypotheses for multiscale phenomena operating in polymer nanocomposites dielectrics [18-19]. Fig. 1 shows the physical description of the interfacial region in polymer nanocomposites [18]. In thermoplastics, the interfacial polymer can exhibit changes in crystallinity, group mobility, chain conformation, molecular weight, and chain entanglement density. There is an additional complication of changes in cross link density, in thermosets, due to small molecule migration to or from the interface.

The interfacial region has a direct impact on the dielectric properties of the composites. Therefore it is important to study the interfacial region. A multi-core model was proposed, which tries to capture the charge behavior and structure of the interfacial region. The metal oxide nanoparticle has a surface charge, which creates a Stern layer at the 2D interface, which is screened by a charged layer in the polymer. The next layer is a diffuse double layer of charge with around 10 nm of radial depth in a resistive medium (polymer). Since the diffusion double layer is a region of mobile charge, both the dispersion of nanoparticles and the resulting dielectric properties in the polymer nanocomposites have significant influence.

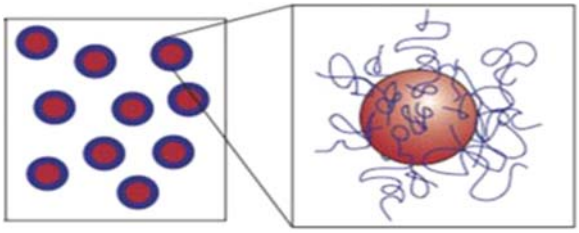

Fig. 1. Physical depiction of the interface re Based on the interfacial structure, hypotheses to explain the impact of interfacial region on the dielectric properties are summarized as following: [18].

Based on the interfacial structure, hypotheses to explain the impact of interfacial region on the dielectric properties are summarized as following [18].

The interfacial region becomes more dominant, as the size of the filler is reduced. The density and perhaps the depth of trap sites are altered due to the change in local structure which affects the carrier mobility and energy. The carriers are accelerated over shorter distances and have reduced energy if they are trapped more often and same is the case for carriers that are scattered. As a result, the dielectric life time of the polymer is increased (Fig. 2).

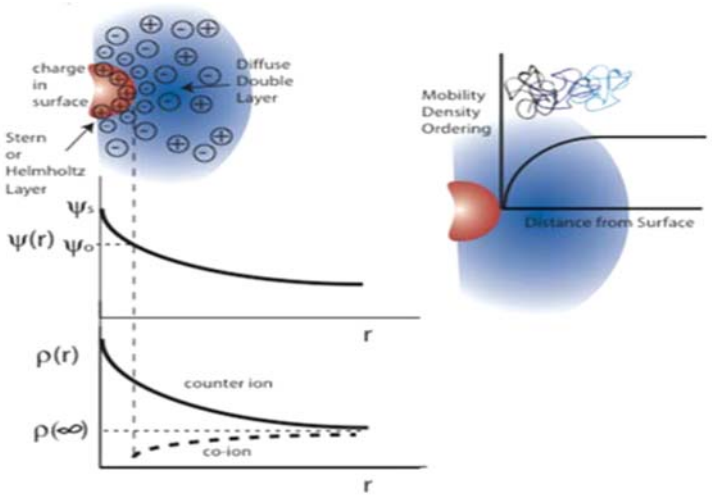

Fig. 2. Physical depiction of the interface region in polymer nanocomposites [19].

The voltage required for charge injection is increased as the homocharge resulting from carrier trapping mitigates the electric field at the electrodes. Thus the voltage required for the short term breakdown is also increased. The breakdown strength becomes the function of the rate of measurement (A.C., D.C., or impulse) as the charge takes time to build up. As the nanocomposites have larger interfacial area, it increases the probability for scattering. Scattering may become the primary mechanism for the increase in the breakdown strength of nanocomposites during impulse test conditions, since significant shielding homocharge cannot be accumulated in such a short time. Because interfacial area is so large, while some of the above mechanisms may operate in micron sized filler filled polymer

composites, they are then overshadowed by the large defects the micron scale fillers introduce and the field enhancements they create. Microcomposites exhibit Maxwell-Wagner interfacial polarization, which is generally finite in nanocomposites and depends on filler concentration and filler material [18-19]. Electroluminescence, photoluminescence, thermally stimulated currents, X-ray secondary emission spectroscopy and electron paramagnetic resonance provided experimental evidence to suggest the working of the hypothesis [18, 20].

3. Surface Modification of Nanoparticles

As the properties of polymer nanocomposites are often influenced by the interfacial region, control of interface becomes very important. Failure to control the interface results in aggregation or agglomeration of nanoparticles in polymer matrix, which leads undesirable properties due to poor film quality and inhomogeneities [12]. Thus, proper dispersion of nanoparticles in polymer nanocomposites plays an important role in polymer nanocomposites. Without proper dispersion and distribution of filler particles in polymer, the high surface area of nano-sized particles is compromised and the aggregates can act as defects, which limits properties [22].

The most common method to achieve proper dispersion is to modify the surface of nanoparticles. The first aspect of modifying the surface of nanoparticles is to attain stabilization of particles against agglomeration to accomplish homogeneous nanocomposites. The second aspect is to render the guest material (nanoparticle filler) compatible with host material (polymer). The third interest in nanoparticles modification is to enable their self-organization [23]. Surface modification of nanoparticles can be obtained by using suitable surfactants that yield an adsorptive interface or by grafting organic groups on the surface of metal oxide nanoparticles, e.g., using phosphates, phosphonates or silanes as coupling agents or dispersants which yields stable and complex organic oxide interface [24-25].

4. Role of Volume Fraction

Previous studies have shown that as the volume fraction of the high permittivity component, nano particle fillers, is increased, the effective permittivity of the nanocomposites also increases [26-28]. However, increasing the volume fraction of the nanoparticles typically decreases the apparent dielectric breakdown strength of the nanocomposite due to the enhancement of the local electric field in the host material [29] and nanocomposites with large volume fractions of nanoparticles typically exhibit porosity that is detrimental to their dielectric performance. Therefore, the role of volume fraction of high permittivity nanoparticles on the dielectric properties (permittivity, loss and breakdown strength) is important and should be rationally chosen in order to maximize the stored electrical energy density.

Many mixing models like parallel model, series model, Lichteneckers rule exist which are able to predict electrical properties based on the dc conductivity/resistivity and work best for dilute composites at low volume fractions [30]. Another popular method of predicting the properties of composites is percolation theory, which is based on the assumption that the properties will change when the second phase is totally connected, i.e., percolated, from one side of the composite to the other [31]. The volume fraction at which percolation occurs is called the "percolation threshold." Percolation threshold depends on many factors, including the connectivity of the phases, the size of each phase, the shape of each phase and the wetting behavior of the phases. Percolation models allow for a large, orders of magnitude, change of properties over a very small concentration range [32].

As a mixing system, composites filled with inorganic fillers are ideal objects from the point of view of percolation theory. When the concentration of fillers is low, the composites will behave more like the insulating matrix. Once the volume fraction of fillers nears the percolation threshold, for example, 16 % or 19 % considering impurities, the electrical properties of the composites can be obviously changed by the channels formed in which charge carriers connect inorganic fillers [33]. The percolation threshold for a 2-dimentional system is accurately predicted as 50 % by effective medium theory and the predicted percolation threshold for 3-dimentional system is at 33 % by effective medium theory [33-34].

5. Dielectric Breakdown

The dielectric material will suddenly begin to conduct current if the voltage across it becomes too high. This phenomenon is called „dielectric breakdown" [35] and the maximum voltage that can be applied without breaking is called „dielectric breakdown strength". In solid dielectrics, electrical breakdown usually results in permanent damage.

The breakdown in a dielectric material is controlled by several mechanisms shown in [36-37]. Under a variety of field stresses, the breakdown suffered by dielectric materials presents a very strong time dependent relationship and can be divided into five or more kinds by breakdown speed. Electrical, thermal and electromechanical breakdown mechanisms are known as the short-term breakdown or degradation mechanisms [38] mechanisms and the others are long term Fig. 3. Schematic depicting times and electric fields at which various electrical breakdown in polymers and composite dielectrics is limited by high field carrier injection and charge trapping electrode-dielectric interface [37].

Electromechanical breakdown is controlled by mechanical properties of dielectric material under high electrical stress and structural parameters. Generally large changes in dielectric breakdown strength at temperatures approaching glass transition temperature are attributed to be related to electromechanical breakdown mechanism (Fig. 3). Where gas is present inside any voids in the dielectric material, gas gets ionized leading to breakdown or discharge within the void under high electric fields leading to the phenomenon known as partial discharge breakdown.

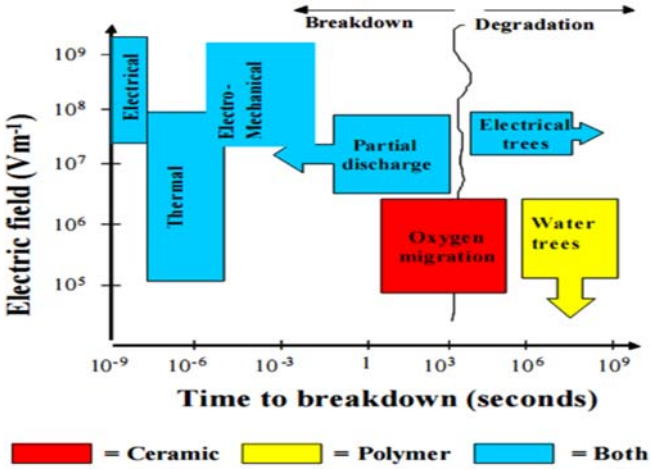

Fig. 3. Schematic depicting times and electric fields at which various electrical breakdown in polymers and composite dielectrics is limited by high field carrier injection and charge trapping electrode-dielectric interface [37].

The discharge damages the structure of the materials and voids or cracks becomes larger, which can be considered as degradation, which erodes the dielectric resulting in breakdown. Discharge may also take place in surface of the dielectric if the surface is contaminated by dirt, water or any other impurities.

Various factors influence the dielectric breakdown event, which include temperature; defects and inhomogenity of material; thickness, area and volume of the material; duration of time for which the dielectric is subjected to electric field; surface conditions and the method of placing the electrodes; area of the electrodes; composition of the electrodes; moisture (humidity) and other contaminations; aging and mechanical stress.

6. Feasiblity $NaNbO_3$-PVDF Based Nanocomposite

It was found that interface layers in the nanocomposites might be more conductive than the polymer matrix, which mitigated the space charge accumulation and field concentration by fast charge dissipation. Zhang and coworkers demonstrated large enhancement in the electric energy density and electric displacement level in the nanocomposites of (PVDF-TrFE-CFE) terpolymer/ZrO_2 nanoparticles. Through the interface effect, the presence of 1.6 vol % of ZrO_2 nanoparticles raised the maximum electric displacement D from 0.085 C/m^2 under 400 MV/m in the neat terpolymer to more than 0.11 C/m^2 under 300 MV/m in the nanocomposites. The dielectric nanocomposites composed of P(VDF-TrFECTFE) and surface-functionalized TiO_2 nanoparticles with comparable dielectric permittivities [38-40] and homogeneous nanoparticle dispersions were prepared. It was found that the presence of the nanoscale filler favors the formation of smaller crystalline domains and a higher degree of crystallinity in the polymer. In drastic contrast to their weak-field dielectric behavior, substantial enhancements in electric displacement and energy density at high electric fields have been demonstrated in the nanocomposites. However, with the increasing concerns on environmental safety and biocompatibility, the need to expel lead (Pb) from modern electronics has been receiving more attention. Using high aspect ratio dielectric inclusions such as nanowires could lead to further enhancement of energy density. Therefore, the present review focuses on the development of a lead-free nanowire reinforced polymer matrix capacitor for energy storage application. Lead-free sodium niobate nanowires ($NaNbO_3$) were synthesized using hydrothermal method, followed by mixing them with polyvinylidene fluoride (PVDF) matrix using a solution-casting method for nanocomposites fabrication. Capacitance and breakdown strength of the samples were measured to determine the energy density. The energy density of $NaNbO_3$/PVDF composites was also compared with that of lead-containing ($PbTiO_3$/PVDF) nanocomposites and previously developed $Pb(Zr0.2Ti0.8)O_3$/PVDF composites to show the feasibility of replacing lead-containing materials. The energy density of $NaNbO_3$/PVDF capacitor is comparable to those of lead-containing ones, indicating the possibility of expelling lead from high-energy density dielectric capacitors.

Ceramics are the other common material broadly used in dielectric capacitors [41]. Compared with polymers, ceramics such as $BaTiO_3$, $Pb(Zrx Ti1-x)O_3$ (PZT), and lanthanum doped PZT (PLZT) have significantly higher relative dielectric constants. However, the breakdown strength of ceramics is typically two orders of magnitude lower than dielectric polymers [42]. Moreover, due to its fragility and brittleness, it is difficult to manufacture ceramic capacitors with desired capacity for energy storage applications [43].

Therefore, a good deal of research effort has been devoted to combine the high dielectric constant of ceramics and high breakdown strength of polymers through the composite approach. To date, many research groups increased the energy density of dielectric capacitors using a nano composite approach, including barium titanate ($BaTiO_3$) nano particles reinforced polycarbonate (PC) [44] and poly(vinylidene fluoride- co-hexafluoropropylene) (PVDF-HFP) [45], modified BaTiO3 nanoparticle with PVDF [46-47], tanium dioxide (TiO_2) nanoparticles with PVDF terpolymer [48], calcium copper titanate (CCT) reinforced polyimide [49], ,silver nanoparticle/poly (vinyl pyrrolidone) core-shell structure for high dielectric constant and low loss epoxy matrix composite [50] and PZT or PLZT powders reinforced PVDF [51-52].

Recently, Andrews, *et al.* developed a micromechanics model to show that using higher aspect ratio nanowires instead of nanoparticle inclusions could lead to significant increase in the dielectric constant of the nanocomposites [53]. Further, Tang, *et al.* [54] experimentally demonstrated that the use of nanowires instead of nanoparticles could significantly increase the dielectric energy density of the nanocomposites.

7. Preparation of NNO/PVDF Nanocomposites

The fabrication process of the NNO/PVDF nanocomposites utilized a two-step procedure; NNO nanowires were first synthesized using hydrothermal technique, r followed by dispersing nanowires in PVDF and dimethylformamide (DMF) solution to form nanocomposites by solution casting method. Samples with volume fractions ranging from 5 % to 30 % were prepared to study the nanowire volume fraction influence on energy density.

6.1. NaNbO3 Nanowires Synthesis

Sodium niobite nanowires were synthesized following a hydrothermal method developed by Jung, *et al.* [20]. In a typical process, a 12 M NaOH solution was prepared by dissolving 33.6 g of NaOH (Acros Organics, 98 %) into 70 mL of deionized water (DI).

Subsequently, 3.5 g of Nb_2O_5 (Aldrich, 99.99 %) were added into the NaOH solution. After stirring for a period of 30 minutes at room temperature, the mixture was transferred into a 160 mL Teflon lined stainless steel autoclave with a fill factor of 80 %. The autoclave was placed inside an electrical oven to undergo hydrothermal reaction at 180 °C for 4 h. After cooling down to room temperature, white precipitate was filtered, washed with DI water for several times, and dried at 80 °C for 12 h. Finally, NNO powders were annealed at 550 °C for 4 h in order to obtain crystallized NNO nanowires [55].

PVDF and DMF (99.8 %) were mixed at a 1:10 weight ratio and heated up at 80 °C for 30 minutes to fully dissolve the PVDF. Nanocomposites were prepared by dispersing NNO or PTO nanowires into PVDF/DMF solution by manual stirring and horn sonication until a homogeneous mixture was obtained. Subsequently, solution was casted onto a PTFE film and dried at 80°C for 6 h [55]. In order to achieve a consistent thickness over the entire film, nanocomposites were hot pressed at 160 °C for 15 minutes under a constant pressure of 1 ton. Finally, top and bottom surfaces of nanocomposites were coated with silver paint as electrodes for electrical testing. The fabrication process of the nanocomposites is schematically shown in Fig. 4 [55].

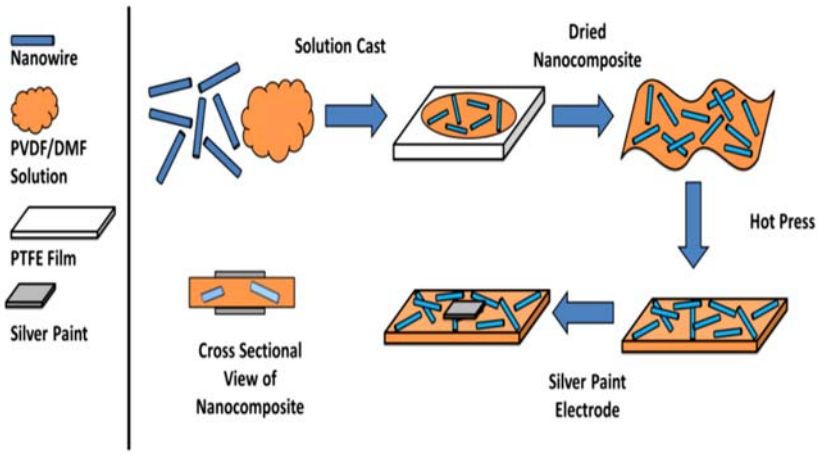

Fig. 4. Preparation steps involved in nanocomposite [55].

The breakdown voltages were measured according to standard (Experimental setup utilized a 30 kV high voltage power supply and a digital oscilloscope, both connected to a 20 MHz function/arbitrary waveform generator In order to avoid arcing prior to breakdown, nanocomposites were held inside a 500 mL beaker filled with silicon oil. Breakdown voltage was recorded through a digital multimeter connected to the high voltage power supply.

The morphology of the synthesized NNO nanowires (NWs) is shows that NNO NWs have an average diameter of 400 nm with length up to 20 μm. As indicated from the SEM images, homogeneous dispersion of the nanowires throughout the entire sample is achieved and no voids are shown in the samples. As expected, SEM images displayed random orientation of nanowires inside the polymer matrix. After the characterization of dielectric constant and loss of the nanocomposites, breakdown strength testing is carried out to fully understand the energy density [55].

Recently, Penn state team [56] developed the boron nitride polymer composite it can handle high temperatures exceeding 480 °F under high voltage application. This material is easy to manufacture by first combining the nanosheets and the polymer. Then the polymer has to be cured using light or heat to generate crosslinks. As the nanosheets measure only around 2 nm in thickness and 400 nm in lateral size, they stay flexible. The combined material offers exceptional dielectric properties such as heat resistance, higher voltage capability and bendability. This composite polymer is made of divinyltetramethyldisiloxanebis (benzocyclobutene) surrounding boron nitride nano sheets. Boron nitride is structurally similar to graphene and forms sheets a single atom thick. The resulting material exhibits superior properties compared to anything already out there. In order to see how good this new dielectric really is, the team compared its properties to the best polymeric dielectrics on the market. They examined the dielectric constant at 10^4 Hz alternating current, a frequency common in power conditioning, and 300 °C. Under these conditions, they saw minor variations (less than 1.7 percent) compared to eight percent for the best existing system. They also looked at how the dielectric constant changed under direct current and found similar results [56].

8. Conclusions

In this paper we have made a thorough investigation of Pb free nanocomposites for high energy density applications. Expelling lead from commercial applications and materials such as solders, glass, and gasoline has been receiving extensive attention because of the concerns regarding its toxicity. Therefore, our present work focuses on the development of a lead-free nanowire reinforced polymer capacitor with comparable dielectric properties to lead-containing capacitors. We have also emphasized the critical role of the interfacial region and present hypotheses for multiscale phenomena operating in polymer nanocomposites dielectrics. Further, increasing the volume fraction of the nanoparticles typically decreases the apparent dielectric breakdown strength of the nanocomposite due to the enhancement of the local electric field in the host material. The dielectric constant and breakdown strength of nanocomposites with volume fractions ranging from 5 % to 30 % were experimentally tested to determine the energy densities of both nanocomposites. Recent research suggests that the NNO/PVDF composites have higher dielectric constants, lower dielectric loss, and comparable energy density. Therefore, this may demonstrate the feasibility of developing lead-free high-energy polymer capacitors to ultimately replace lead-containing ones.

Acknowledgements

I would like to acknowledge Prof. Vijaya Bhaskara Raju, Director of GITAM Institute of Technology, GITAM University Bengaluru Campus, India for his constant encouragement to finish this work.

References

[1]. K. M. Slenes, P. Winsor, T. Scholz, M. Hudis, Pulse power capability of high energy density capacitors based on a new dielectric material, *IEEE Transactions on Magnetics*, Vol. 37, No. 1, 2001, pp. 324-327.

[2]. C. A. Randall, S. Miyazaki, K. L. More, A. S. Bhalla, R. E. Newnham, Structural-property relationships in dielectrophoretically assembled $BaTiO_3$ nanocomposites, *Mater. Lett.*, Vol. 15, No. 1-2, 1992, pp. 26-30.

[3]. C. P. Bowen, R. E. Newnham, C. A. Randall, Dielectric properties of dielectrophoretically assembled particulate-polymer composites, *J. Mater. Res.*, Vol. 13, No. 1, 1998, pp. 205-210.

[4]. A. Randall, D. V. Miller, J. H. Adair, A. S. Bhalla, Processing of Electroceramic-Polymer Composites Using the Electrorheological Effect, *J. Mater. Res.,* Vol. 8, No. 4, 1993, pp. 899-904.

[5]. Application Note 1217-1, Basics of measuring the dielectric properties of materials, Hewlett Packard Literature Number 5091-3300E, 1992, pp. 6.

[6]. G. J. Johnson, Solid State Tesla Coil, Chap. 3 Lossy Capacitors, 2001, available online at http://www.eece.ksu.edu/~gjohnson/

[7]. O. E. Gouda, A. M. Thabet, H. H. El-Tamaly, How to Get Low Dielectric Losses in Binary and Multi-mixtures Dielectrics at High Frequency, in *Proceedings of the 39th International Universities Engineering Conference*, Vol. 3, 2004, pp. 1237-1240.

[8]. M. Lanagan, Glass Ceramic Materials for Pulsed Power Capacitors, *NSF Center for Dielectric Studies Meeting*, Albuquerque, NM, May 2004.

[9]. Y. Xiaojun, Y. Zhimin, M. Changhui, D. Jun, Dependence of dielectric properties of BT particle size in EP/BT composites, *Rare Metals*, Vol. 25, No. 6, 2006, pp. 250-254.

[10]. Y. Cao, P. C. Irwin, K. Younsi, The Future of Nanodielectrics in the *Electrical* Power Industry, *IEEE Transactions on Dielectrics and Electrical Insulation*, Vol. 7, No. 5, 2004, pp. 797-807.

[11]. F. Ciuprina, I. Plesa, P. V. Notingher, T. Tudorache, D. Panaitescu, Dielectric Properties of Nanodielectrics with Inorganic Fillers, in *Proceedings of the CEIDP Annual Report Conference on Electrical Insulation and Dielectric Phenomena*, 2008, pp. 682-685.

[12]. P. Kim, S. C. Jones, P. J. Hotchkiss, J. N. Haddock, B. Kippelen, S. R. Marder, J. W. Perry, Phosphonic Acid-Modified Barium Titanate Polymer Nanocomposites with High Permittivity and Dielectric Strength, *Advanced Materials*, Vol. 19, 2007, pp. 1001-1005.

[13]. S. Ramesh, B. A. Shutzberg, C. Huang, J. Gao, E. P. Giannelis, Dielectric Nanocomposites for Integral Thin Film Capacitors: Materials Design, Fabrication and Integration Issues, *IEEE Transactions on Advanced Packaging*, Vol. 26, 2003, pp. 17-24.

[14]. Y. Bai, Z.-Y. Cheng, V. Bharti, H. S. Xu, Q. M. Zhang, High-dielectric-constant ceramic-powder polymer composites, *Applied Physics Letters*, Vol. 76, No. 25, 2000, pp. 3804-3806.

[15]. S. Liang, S. R. Chong, E. P. Giannelis, Barium Titanate/Epoxy Composite Dielectric Materials for Integrated Thin Film Capacitors, in *Proceedings of the 48th Electronic Components and Technology Conference*, 1998, pp. 171-175.

[16]. T. J. Lewis, Interfaces: nanometric dielectrics, *Journal of Physics D: Applied Physics*, Vol. 38, No. 2, 2005, pp. 202-212.

[17]. J. K. Nelson, Y. Hu, Nanocomposite dielectrics – properties and implications, *Journal of Physics D: Applied Physics*, Vol. 38, No. 2, 2005, pp. 213-222.

[18]. M. Roy, J. K. Nelson, R. K. MacCrone, L. S. Schadler, C. W. Reed, R. Keefe, W. Zenger, Polymer Nanocomposite dielectrics – the Role of the Interface, *IEEE Transactions on Dielectrics and Electrical Insulation*, Vol. 12, No. 4, 2005, pp. 629-642.

[19]. R. C. Smith, C. Liang, M. Landry, J. K. Nelson, L. S. Schadler, The Mechanisms Leading to the Useful Electrical Properties of Polymer Nanodielectrics, *IEEE Transactions on Dielectrics and Electrical Insulation*, Vol. 15, pp. 187-196.

[20]. J. K. Nelson, Overview of Nanodielectrics: Insulating Materials of the Future, in *Proceedings of the IEEE Electrical Insulation Conference and Electrical Manufacturing Expo*, 2007, pp. 229-235.

[21]. X. Wang, *et al.*, Large-surface-area BN nanosheets and their utilization in polymeric composites with improved thermal and dielectric properties, *Nanoscale Research Letters*, Vol. 7, 2012, pp. 662.

[22]. P. M. Ajayan, L. S. Schadler, P. V. Brawn, Nanocomposite Science and Technology, *Wiley-VCH: Weinheim*, Germany, 2003, pp. 1-223.

[23]. M.-A. Neouze, U. Schubert, Surface Modification and Functionalization of Metal and Metal Oxide Nanoparticles by Organic Ligands, *Monatshefte fur Chemie*, Vol. 139, No. 3, 2008, pp. 183-195.

[24]. M. Hosokawa, K. Nogi, M. Naito, T. Yokoyama (Ed.), Nanoparticle Technology Handbook, *Elvesier*, Oxford, UK, 2007.

[25]. T. P. Schuman, S. Siddabattuni, O. Cox, F. Dogan, Improved Dielectric Breakdown Strength of Covalently-Bonded Interface Polymer-Particle Nanocomposites, *Composite Interfaces*, Vol. 17, No. 8, 2010, pp. 719-731.

[26]. N. Jayasundere, B. V. Smith, Dielectric Constant for Binary Piezoelectric 0-3 Composites, *Journal of Applied Physics*, Vol. 73, No. 5, 1993, pp. 2462-2466.

[27]. Y. Rao, J. Qu, T. Marinis, C. P. Wong, A Precise Numerical Prediction of Effective Dielectric Constant for Polymer-Ceramic Composite Based on Effective Medium Theory, *IEEE Transactions on Advanced Packaging Technologies*, Vol. 23, No. 4, 2000, pp. 680-683.

[28]. J. P. Calame, Finite Difference Simulations of Permittivity and Electric Field Statistics in Ceramic-Polymer Composites for Capacitor Applications, *Journal of Applied Physics*, Vol. 99, No. 8, 2006, pp. 084101-1–084101-11.

[29]. C. Huang, Q. Zhang, Enhanced Dielectric and Electromechanical Responses in High Dielectric Constant All-Polymer Percolative Composites, *Advanced Functional Materials*, Vol. 14, No. 5, 2004, pp. 501-506.

[30]. J. G. Head, N. M. White, P. S. Gale, Modification of the Dielectric Properties of Polymeric Materials, in *Proceedings of the 5th International Conference on Dielectric Materials, Measurement and Applications*, Issue 27-30, 1988, pp. 61-64.

[31]. D. S. McLachlan, M. Blaskiewicz, R. E. Newnham, Electrical Resistivity of Composites, *Journal of American Ceramic Society*, Vol. 73, No. 8, 1990, pp. 2187-2203.

[32]. J. R. Kokan, R. A. Gerhardt, R. Ruh, D. S. McLachlan, Dielectric Spectroscopy of Insulator/Conductor Composites, in *Materials Research Society Symposium Proceedings*, Electrically Based Microstructural Characterization II, Edited by R. A. Gerhardt, M. A. Alim and S. R. Taylor, *Materials Research Society*, Pittsburgh, PA, Vol. 500, 1998, pp. 341-346.

[33]. R. Zallen, The Physics of Amorphous Solids, *John Wiley & Sons*, New York, 2004, pp. 135-191.

[34]. S. Kirkpatrick, Percolation and Conduction, *Reviews of Modern Physics*, Vol. 45, No. 4, 1973, pp. 574-588.

[35]. C. Mukherjee, K. Bardhan, M. Heaney, Predictable Electrical Breakdown in Composites, *Physical Review Letters*, Vol. 83, No. 6, 1999, pp. 1215-1218.

[36]. M. Lanagan, High Power Capacitors and Energy Storage, presented at *Materials Day*, University Park, Penn State University, April 2008.

[37]. L. A. Dissado, L. C. Fothergill, Electrical Degradation and Breakdown in Polymers, *Peter Peregrins Ltd.*, London, UK, 1992.

[38]. S. Li, G. Yin, G. Chen, J. Li, S. Bai, L. Zhong, Y. Zhang, Q. Lei, Short-term breakdown and long-term failure in nanodielectrics, *IEEE Transactions on Dielectrics and Electrical Insulation*, Vol. 17, No. 5, 2010, pp. 1523-1535.

[39]. J. J. O'Dwyer, The Theory of Dielectric Breakdown of Solids, *Oxford University Press*, London, UK, 1964, pp. 1-123.

[40]. J. Claude, Y. Lu, Q. Wang, Effect of Molecular Weight on the Dielectric Breakdown Strength of Ferroelectric Poly(vinylidene fluoride-chlorotrifluoroethylene)s, *Applied Physics Letters*, Vol. 91, Issue 21, 2007, 212904.

[41]. Z. Tian, X. Wang, L. Shu, *et al.*, Preparation of nano BaTiO3-based ceramics for multilayer ceramic capacitor application by chemical coating method, *Journal of the American Ceramic Society*, Vol. 92, No. 4, 2009, pp. 830-833.

[42]. M. Unruan, T. Sareein, J. Tangsritrakul, *et al.*, Changes in dielectric and ferroelectric properties of Fe3+/Nb5+ hybrid doped barium titanate ceramics under compressive stress, *Journal of Applied Physics*, Vol. 104, No. 12, 2008, Article ID 124102.

[43]. O. Guillon, J. Chang, S. Schaab, S.-J. L. Kang, Capacitance enhancement of doped barium titanate dielectrics and multilayer ceramic capacitors by a post-sintering thermo mechanical treatment, *Journal of the American Ceramic Society*, Vol. 95, No. 7, 2012, pp. 2277-2281.

[44]. S. S. Ibrahim, A. A. Al Jaafari, A. S. Ayesh, Physical characterizations of three phase polycarbonate nanocomposites, *Journal of Plastic Film and Sheeting*, Vol. 27, No. 4, 2011, pp. 275-291.

[45]. L. Xie, X. Huang, C. Wu, P. Jiang, Core-shell structured poly(methyl methacrylate)/$BaTiO_3$ nanocomposites prepared by in situ atom transfer radical polymerization: a route to high dielectric constant materials with the inherent low loss of the base polymer, *Journal of Materials Chemistry*, Vol. 21, No. 16, 2011, pp. 5897-5906.

[46]. P. Kim, N. M. Doss, J. P. Tillotson, *et al.*, High energy density nanocomposites based on surface-modified BaTiO3 and a ferroelectric polymer, *ACS Nano*, Vol. 3, No. 9, 2009, pp. 2581-2592.

[47]. Y. P. Mao, S. Y. Mao, Z.-G. Ye, Z. X. Xie, L. S. Zheng, Sizedependences of the dielectric and ferroelectric properties of $BaTiO_3$/polyvinylidene fluoride nanocomposites, *Journal of Applied Physics*, Vol. 108, No. 1, 2010, Article ID 014102.

[48]. Z.-M. Dang, J.-K. Yuan, J.-W. Zha, T. Zhou, S.-T. Li, G.-H. Hu, Fundamentals, processes and applications of high-permittivity polymer-matrix composites, *Progress in Materials Science*, Vol. 57, No. 4, 2012, pp. 660-723.

[49]. L. Ni, X. M. Chen, Dielectric relaxations and formation mechanism of giant dielectric constant step in $CaCu_3Ti_4O_{12}$ ceramics, *Applied Physics Letters*, Vol. 91, No. 12, 2007. Article ID 122905

[50]. A. Chen, K. Kamata, M. Nakagawa, T. Iyoda, H. Wang, X. Li, Formation process of silver-polypyrrole coaxial nanocables synthesized by redox reaction between $AgNO_3$ and pyrrole in the presence of poly(vinylpyrrolidone), *Journal of Physical Chemistry B*, Vol. 109, No. 39, 2005, pp. 18283-18288.

[51]. P. Barber, S. Balasubramanian, Y. Anguchamy, *et al.*, Polymer composite and nanocomposite dielectric materials for pulse power energy storage, *Materials*, Vol. 2, 2009, pp. 1697-1733.

[52]. D. K. Das-Gupta, K. Doughty, Polymer-ceramic composite materials with high dielectric constants, *Thin Solid Films*, Vol. 158, No. 1, 1988, pp. 93-105.

[53]. C. Andrews, Y. Lin, H. A. Sodano, The effect of particle aspect ratio on the electroelastic properties of piezoelectric nanocomposites, *Smart Materials and Structures*, Vol. 19, No. 2, 2010. Article ID 025018.

[54]. H. Tang, Y. Lin, C. Andrews, H. A. Sodano, Nanocomposites with increased energy density through high aspect ratio PZT nanowires, *Nanotechnology*, Vol. 22, No. 1, 2011. Article ID 015702.

[55]. Miguel Mendoza, Md Ashiqur Rahaman Khan, Mohammad Arif Ishtiaque Shuvo, Alberto Guerrero, Yirong Lin, Development of Lead-Free Nanowire Composites for Energy Storage Applications, *International Scholarly Research Network ISRN Nanomaterials*, Vol. 2012, 2012, pp. 1-8. Article ID 151748.

[56]. Qi Li, Lei Chen, Guangu Zhang, *et al.*, Flexible high-temperature dielectric materials from polymer nanocomposites, *Nature*, Vol. 523, 2015, pp. 576-579.

Published by International Frequency Sensor Association (IFSA) Publishing, S. L., 2017 (http://www.sensorsportal.com).

Sensors & Transducers, Vol. 210, Issue 3, March 2017, pp. 29-31

www.sensorsportal.com

Sensors & Transducers

Published by IFSA Publishing, S. L., 2017
http://www.sensorsportal.com

Conducting Polymer PEDOT:PSS: An Emerging Material for Flexible and Transparent Electronics

[1*] Anupama CHANDA, [2] Shalik Ram JOSHI, [3] Rakesh SAHOO, [2] Shikha VARMA, [4] Kwangsoo NO

[1] Dr. H. S. Gour Central University, Sagar-470003, M. P, India
[2] Institute of Physics, Bhubaneswar-751005, Odisha, India
[3] Institute of Minerals and Materials Technology, Bhubaneswar-751013, Odisha, India
[4] KAIST, 291 Daehak-ro, Yuseong-gu, Daejeon 34141, Republic of Korea
[1] Tel: 07582265459
[*] E-mail: anupamamatsc@gmail.com

Received: 9 January 2017 /Accepted: 3 March 2017 /Published: 31 March 2017

Abstract: A one dimensional variable range hopping type conduction is observed in Poly (3, 4-ethylenedioxythiophene): polystyrenesulfonate (PEDOT:PSS) films obtained by a spin coating technique on polyethylene naphthalate (PEN) substrate and the mechanism behind enhancement in conductivity in 3 % dimethyle sulfoxide (DMSO) doped PEDOT:PSS film is due to the phase segregation of PSS on the surface and reduction of energy barrier between the conducting grains. Enhanced conductivity of PEDOT:PSS films and transparency more than 80 % in the visible region makes PEDOT:PSS films suitable for flexible and transparent optoelectronic devices.

Keywords: PEDOT-PSS, Conductivity, Variable range hopping, XPS, UV-Vis.

1. Introduction

In the recent years there has been an increasing interest in the field of organic electronics due to its light-weight, high flexibility, and easy processability. Indium-tin oxide (ITO) has been widely used as the transparent electrode in flexible devices, but due to its limitation in mechanical flexibility, large use and high cost there is a great demand for an alternative solution like organic based electrodes with both high transparency and high conductivity. Poly (3,4-ethylenedioxythiophene): polystyrenesulfonate (PEDOT : PSS) has been emerged as a promising material in the field of optoelectronic devices due to its high conductivity and transparency along with other attractive polymer properties like the ease of synthesis and high degree of flexibility [1-3]. It has been widely used as a buffer layer in organic electronics. It has a higher work function (5.2 eV) over ITO (4.5-5.14 eV). Great effort has been given to research to get higher luminous intensity and higher external efficiency in the Organic Light Emitting Diodes (OLEDs) using PEDOT:PSS anode [4, 5]. Although, commercially available PEDOT : PSS (Baytron P, Bayer Corporation) has a conductivity of less than 1 S/cm, recently, it is observed that the conductivity of PEDOT : PSS (PH-1000) films can be enhanced by three orders of magnitude by undergoing different processing steps or by doping with various additives [6-9]. There are several reports on the mechanism of enhanced conductivity of PEDOT:PSS due to additives, but the subject is still under debate. In this study, we obtain conductivities as high as 980 S/cm for PEDOT:PSS (PH1000 from H. C.Starck)

with the addition of 3 at% Dimethyl sulfoxide (DMSO) and the mechanism of conductivity enhancement is explained by taking into theoretical consideration along with X ray Photoelectron Spectroscopy (XPS) study.

2. Experimental

2.1. Materials and Methods

In this work PEDOT:PSS (Clevios PH1000, Heraeus Clevios GmbH, Germany) was used as the starting material to which DMSO (3 at%) (Sigma-Aldrich) was added and mixed well before deposition. Films were deposited on glass substrates by using a spin coating technique (4000 rpm, 40 sec) and after deposition, films were annealed at 140 ^{o}C for 1h in the air. Before deposition of the films, oxygen plasma treatment (for 3 min at 100 Watt) was carried out on the substrates to increase the adhesion of the films.

2.2. Characterization

After deposition and annealing of the films, the temperature dependent resistivity measurement of the films was performed using four probe method and the transmittance study was done from UV-Visible spectra using Shimadzu UV-VIS spectrophotometer. XPS analysis was carried out in a VG Microtech-ESCA2000 Multilab instrument to study the chemical states of the surface.

3. Results and Discussion

Fig. 1 shows the transmittance spectra of undoped and 3 % DMSO doped PEDOT:PSS films taken from a UV-Visible spectrophotometer. Transmittance of more than 80 % in the visible region in 3 % DMSO doped PEDOT:PSS films was observed from UV-Visible spectra. Fig. 2 indicates conductivity versus temperature plot obtained by a four probe method and the data were fitted with a function [10]

$$\sigma = \sigma_0 e^{-\left(\frac{T_0}{T}\right)^{\alpha}} \qquad (1)$$

where σ is the conductivity at temperature T and σ_o is the conductivity at infinite temperature. α = 1/(1+D) denotes the signature of variable range hopping for D dimension. T_o is the effective energy barrier for hopping of charge carriers between localized states. The corresponding parameters obtained after fitting the experimental data with the above function is given in Table 1 from which the value of α is found to be 0.48 for 3 % DMSO doped PEDOT:PSS films giving D=1.08 which indicates one dimensional hopping conduction mechanism is suitable for the films. The conductivity at room temperature is observed to be enhanced 4 orders of magnitude in 3% DMSO doped films as compared to undoped PEDOT:PSS films. Also, it is noted that T_o drops (from 1940 to 305) by the addition of DMSO suggesting that the effective energy barrier for 3% doped film is decreased which leads to an increase in conductivity. In Fig. 2 solid line (black) indicates the experimental plot and dash line (red) indicates the fitted plot.

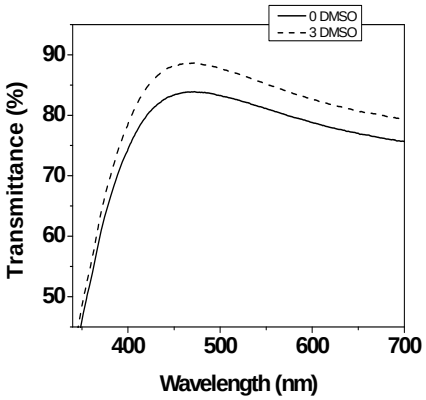

Fig. 1. Transmittance spectra of undoped and 3 % DMSO doped PEDOT:PSS films.

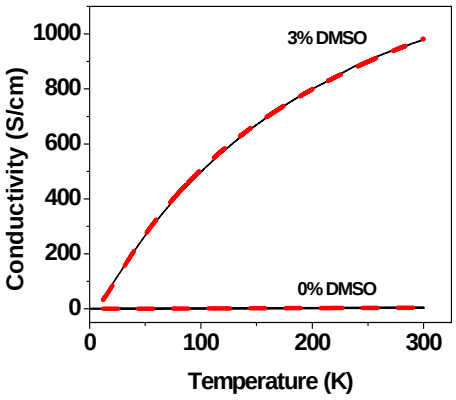

Fig. 2 Temperature versus conductivity of PEDOT:PSS films.

Table 1. Parameters obtained using Eq. (1).

DMSO (%)	σ_{300}(S/cm)	σ_0 (S/cm)	α	T_o (K)
0	0.1	38	0.42	1940
3	980	2690	0.48	305

Fig. 3 (a, b) shows the XPS spectra of sulphur for undoped and 3 % DMSO doped PEDOT:PSS films along with its deconvolution. It can be seen from the deconvoluted spectra that various components of S ($2p_{3/2}$, $2p_{1/2}$) signal are coming from PEDOT, PSS-, PSSNa, PSSH. From the spectra PEDOT to PSS ratio was calculated and was found to be decreased from 3.7 for pristine to 2.91 for 3 % DMSO doped films which indicates phase segregation with an excess of PSS on

the surface. The increase in conductivity due to 3 % DMSO doped film is associated with the reduction of insulating PSS shell surrounding conducting PEDOT grains and maintaining a good connection between the PEDOT grains. This enhances the transportation of carriers between the PEDOT grains easy which in turn increases the conductivity.

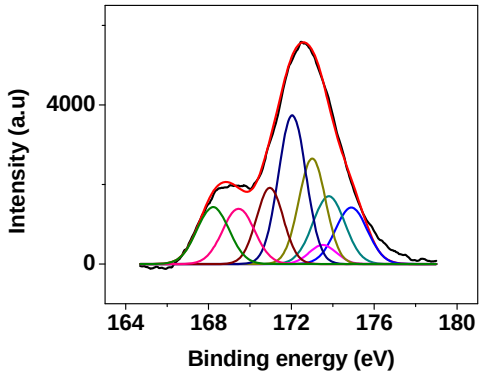

Fig. 3 (a) XPS spectra of undoped PEDOT:PSS film.

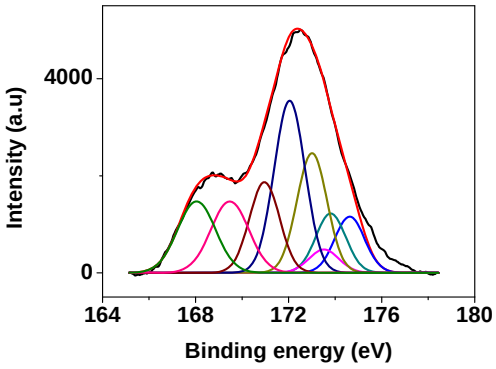

Fig. 3 (b) XPS spectra of 3 % DMSO doped PEDOT:PSS film.

4. Conclusion

In conclusion, a one dimensional variable range hopping type conduction is observed in PEDOT:PSS films and the mechanism behind enhancement in conductivity in 3 % DMSO doped PEDOT:PSS film is due to the phase segregation of PSS on the surface and reduction of energy barrier between the conducting grains. Enhanced conductivity of PEDOT:PSS films and transparency more than 80 % in the visible region makes PEDOT:PSS films suitable for flexible and transparent optoelectronic devices.

Acknowledgements

The first author (Anupama Chanda) would like to acknowledge UGC for providing financial support from Start-up grant project to carry out the research.

References

[1]. G. Hewang and F. Jonas, Poly (alkylenedioxythiophene)s - new, very stable conducting polymers, *Advance Functional Materials*, Vol 4, Issue 2, 1992, p. 116.

[2]. L. B. Groenendaal, F. Jonas, D. Freitag, H. Pielartzik, and J. R. Reynolds. Poly(3,4-ethylenedioxythiophene) and its derivatives: past, present, and future, *Advanced Materials*, Vol. 12, Issue 7, 2000, pp. 481–494.

[3]. Q. Pei, G. Zuccarrelo, M. Ahlskogt, O. Inganas. Electrochromic and highly stable poly(3,4-ethylenedioxythiophene) switches between opaque blue-black and transparent sky blue, *Polymer*, Vol. 35, Issue 12, 1994, pp. 1347.

[4]. K. Fehse, K. Walzer, K. Leo, W. Lovenich and A. Elschner. Highly Conductive Polymer Anodes as Replacements for Inorganic Materials in High-Efficiency Organic Light-Emitting Diodes, *Advance Materials*, Vol. 19, Issue 3, 2007, pp. 441.

[5]. M. Vosgueritchian, D. J. Lipomi and Z. Bao. Highly conductive and transparent PEDOT: PSS films with a fluorosurfactant for stretchable and flexible transparent electrodes, *Advance Functional Materials*, Vol. 22, Issue 2, 2012, pp. 421.

[6]. B. P. A. Levermore, L. Chen, X. Wang, R. Das and D. D. C. Bradley. Fabrication of Highly Conductive Poly(3,4-ethylenedioxythiophene) Films by Vapor Phase Polymerization and Their Application in Efficient Organic Light-Emitting Diodes, *Advance Materials*, Vol. 19, Issue 17, 2007, pp. 2379.

[7]. Y. H. Kim, C. Sachse, M. L. Machala, C. May, L. Muller- Meskamp and K Leo, Highly Conductive PEDOT:PSS Electrode with Optimized Solvent and Thermal Post-Treatment for ITO-Free Organic Solar Cells, *Advance Functional Materials*, Vol. 21, Issue 6, 2011, pp. 1076.

[8]. D. Alemu, H. Y. Wei, K. C. Ho and C. W. Chu, Highly conductive PEDOT: PSS electrode by simple film treatment with methanol for ITO-free polymer solar cells, *Energy Environmental Science*, Vol. 5, Issue 11, 2012, pp. 9662.

[9]. D. A. Mengistie, M. A. Ibrahem, P. C. Wang, and C. W. Chu. Highly conductive PEDOT:PSS treated with formic acid for ITO-free polymer solar cells, *ACS Applied Materials Interfaces,* Vol. 26 , Issue 6, 4, 2014, pp. 2292.

[10]. N. Mott and E. A. Davis, Electronic Processes in Non Crystalline Materials, *Clarendon Press*, Oxford, 1979.

Sensors & Transducers, Vol. 210, Issue 3, March 2017, pp. 32-37

www.sensorsportal.com

Sensors & Transducers

Published by IFSA Publishing, S. L., 2017
http://www.sensorsportal.com

Preparation, Characterization and Spectroscopic Investigations of PEOX-PVOH Blend Films

[1,*] Manohara S. R., [1] Rajashekara T. N., [1] Shubha A., [1] Subhranshu S. S., [2] Murugendrappa M. V. and [3] Navya P. N.

[1] Nano-Composites and Materials Research Lab, Department of Physics, Siddaganga Institute of Technology, Tumakuru-572103, Karnataka, India
[2] Department of Physics, BMS College of Engineering, Bengaluru-560019, Karnataka, India
[3] Department of Biotechnology, Siddaganga Institute of Technology, Tumakuru-572103, Karnataka, India
[*] Tel.: +91-816-228 2696, fax: +91-816-228 2994
[*] E-mail: sr.manohara@yahoo.com

Received: 9 January 2017 /Accepted: 3 March 2017 /Published: 31 March 2017

Abstract: A stable and free standing polymer blend films of poly (2-ethyl-2-oxazoline) [PEOX] and poly(vinyl alcohol) [PVOH] were prepared by solution casting technique at different weight percentages (70/30, 50/50, 30/70). The prepared blends were characterized by scanning electron microscopy (SEM), and ultraviolet-visible (UV-Vis) and Fourier transform infrared (FTIR) spectroscopy. Various optical properties such as absorption band edge, direct and indirect band gap, and optical activation energy were obtained by UV-Vis spectral analysis. FTIR analysis confirms the specific hydrogen bonding between $–CH_3$ groups of PEOX and –OH groups of PVOH, and also the hydrophilic nature of the blends.

Keywords: Polymer blend, Solution casting, Band edge, Band gap, Optical spectroscopy.

1. Introduction

The studies on water soluble polymers like poly(vinyl alcohol), poly(ethylene oxide), poly(acryl amide), poly(vinyl pyrrolidone), poly(2-ethyl-2-oxazoline) etc. has a considerable interest due to their bio-compatibility, which in turn find applications in field of bio-medical and pharmacy.

Poly(2-ethyl-2-oxazoline) [PEOX] is an amorphous, water soluble, non-ionic, and thermoplastic polymer. PEOX belongs to the group of polymers known as poly(oxazolines) and is called as tertiary amide polymer. Poly(oxazolines) are useful in a various applications, including biocompatible materials for drug delivery and steric stabilizers [1-3]. PEOX has good Newtonian characteristics, shear stability, melt flow and is a potential substitute for PVOH and poly(vinyl pyrrolidone), and has good thermal stability [4]. US Food and Drug Administration (FDA) have approved PEOX for use as an indirect food additive. Liposomes on which PEOX was grafted have been shown to circulate for a long time in the blood and to be associated with a reduction of the clearance rates in spleen and liver [5]. PEOX is readily soluble in water and softens at 110 to 120 °C with a thermal stability up to 380 °C, and hence it's both solution and melt can be used in adhesive applications [6, 7]. It combines very well with many polymers to form polymer blend, and thus, can be used to improve the properties of polymer system [7-10]. PEOX is used as a compatibilizing agent in various personal care products and medical field due to its

water solubility, dispersant properties and bio-compatibility [11-13]. This polymer also finds its application in photo resists inks and coatings [14, 15]. PEOX is a pH responsive polymer, in addition to being hydrophilic, which enables very specific control of drug delivery and release at the appropriate site through pH cues [16-18].

Polyvinyl alcohol [PVOH] is a water soluble, bio-compatible, odorless, tasteless and non-toxic polymer. PVOH is not known to occur as a natural product. The physical properties and specific functions of PVOH depend on the degree of polymerization and the degree of hydrolysis. The key characteristics of PVOH are outstanding film forming, high binding strength, adhesive and emulsifying properties [19]. It has resistance to oils, grease and solvents, and also has high tensile strength and flexibility as well as high aroma and oxygen barrier properties. PVOH is ecological advantageous due to its bio-degradability and combustion does not generate any residues. It can react with many type of functional groups since it has number of hydroxyl groups. Polyvinyl alcohol with high molecular weight is useful for preparing gel which possesses both high strength and modulus, and, hence, it is used for the production of fibers, films and gels. It is a useful industrial, medical and biometric material [20]. PVOH finds application in textile, paper making, and variety of coatings. Physically and chemically modified PVOH is helpful in biomedical applications. Due to its water solubility and bio-degradable properties, PVOH is widely used as packing material for chemicals such as detergent, cleanser, disinfector, laundry powder, pesticide and dye stuff. It has broad industrial applications due to its chemical resistance and physical properties. PVOH is useful, as modifier and thickener, in water transfer printing process and hard contact lens solution as a lubricant, and for making protective chemical-resistant gloves.

Blending of polymers is an interesting way of making new materials with attractive properties. The properties of the blend can be tailored by varying the composition and processing conditions. To the best knowledge of authors, there are no reports on optical properties and the interaction study of PEOX-PVOH polymer blends. Therefore, in the present study, an attempt is made to prepare PEOX-PVOH polymer blends by solution casting method with an aim to make blends with enhanced properties. This investigation will be quite helpful for understanding compatibility and miscibility of the polymer blends.

2. Experimental

2.1. Preparation of PEOX-PVOH Polymer Blends

Poly (2-ethyl-2-oxazoline) [M_w: 500000] and poly(vinyl alcohol) [M_w: 85000-124000] were obtained from Sigma-Aldrich, India and used as received. The PEOX-PVOH polymer blend films were prepared by solution casting method in three different weight percentages (wt%) [70/30, 50/50, 30/70] using deionized water (DI water) as a solvent. PEOX and PVOH were first separately disolved in the DI water, and then both polymer solutions were mixed homogeneously using a magnetic stirrer at about 60 °C. This homogeneous solution was poured into the petridishes and kept in vacuum oven (at 60 °C) for evaporation of solvent for 4 days. The fully dried films were peeled off from the petridishes, and heated in a vacuum oven at 100 °C for 3 h to remove residual water and to make cross linking reaction. For the purpose of comparison, pure PEOX and pure PVOH films were also prepared. Thickness of the obtained films was in the range of 120-180 μm.

2.2. Measurements

Surface morphology of the pure PEOX, PVOH, and blend films was studied by a scanning electron microscope (Tescan Vega3, Czech Republic). Ultraviolet-Visible (UV-Vis) absorption spectra of the samples were recorded in the wavelength range of 200-800 nm using UV-Vis spectrophotometer (Shimadzu 1800, Japan). Fourier transform infrared (FTIR) spectra of samples were obtained in the spectral range of 400-4000 cm^{-1} using Bruker Alpha FTIR spectrometer. Thickness of these samples was measured using digital vernier (Aerospace, India) which has least count of 0.01 mm.

3. Results and Discussion

3.1. Morphological Characterization

Fig. 1a-e shows SEM images of pure PEOX, pure PVOH, and PEOX/PVOH blend films. SEM images show that the polymer surfaces (blend and pure) have heterogeneous type of morphology which may be due to the irregular shaped clusters formed by polymer chains. This may be attributed to the formation of hydrogen bonding between polymers chains.

3.2. UV-Vis Spectral Analysis

UV-Vis spectra of pure PEOX, pure PVOH, and PEOX/PVOH blend films are shown in Fig. 2a. It can be observed that, there is an increase in the absorbance, and absorption edges are slightly shifted toward lower wavelength with the increase of weight percentage of PVOH in the PEOX/PVOH blend system. However, absorption plays an important role in the optical properties of polymers. The relationship between absorption coefficient, α, and photon energy can be expressed as [21, 22]:

$$\alpha h\nu = A(h\nu - E_g)^r , \quad (1)$$

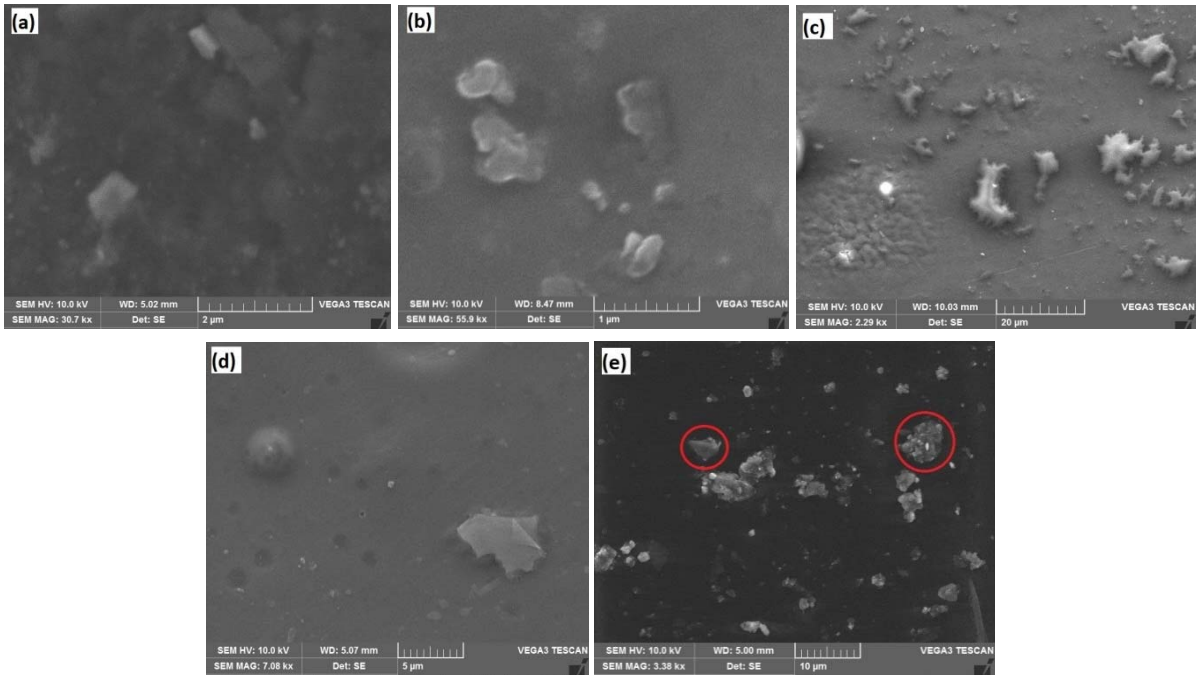

Fig. 1. SEM images of (a) pure PEOX, (b) 70/30, (c) 50/50, (d) 30/70, and (e) pure PVOH.

where α is the absorption coefficient, A is the parameter that depends on the transition probability, h is the Planck's constant, ν is the frequency of photon, E_g is the optical energy gap of the substance, r is the parameter that gives the type of electron transition. Two distinct linear relations can be found from equation (1), one for r = 1/2 (direct transition), and other for r = 2 (indirect transition) [23].

The position of the absorption edge, the direct band gap and indirect band gap were obtained from the plots of absorption coefficient (α) versus photon energy ($h\nu$), $(\alpha h\nu)^2$ versus $h\nu$, and $(\alpha h\nu)^{1/2}$ versus $h\nu$, respectively, and are shown in Fig. 2 (b-d). The values of the absorption edge and the direct/indirect band gap were determined by extrapolating the linear portions of these curves to zero absorption in the large absorption region. The values of various optical parameters are shown in Table 1. The optical activation energy has been determined using the Urbach rule [24],

$$\alpha = B\exp(h\nu / E_a), \tag{2}$$

where B is the constant and E_a is the activation energy which represents the width of the tail of localized states in forbidden band gap. The values of E_a are calculated by taking the reciprocal of slopes obtained from the plot of $\ln\alpha$ versus photon energy ($h\nu$) as shown in Fig 2e, and are listed in Table 1.

From the Table 1, it can be seen that, the values of absorption edge, direct and indirect band gap increases with increasing PVOH weight percentage in PEOX/PVOH blend, and they become maximum for 30/70 wt% PEOX/PVOH blend. The increase in the optical energy gap values is due the interaction between the polymer chains [25, 26] and the formation of some bonds [27]. This shows that as a result of blending, there is a change in the number of final states in the band gap [23, 28]. The increase in the number of defects which led to increase in the density of localized states in the band structure also led to increase of optical energy gap [29].

Table 1. Absorption edge, optical energy gap (direct and indirect), and activation energy values of pure PEOX, pure PVOH, and PEOX/PVOH blends.

PEOX/PVOH blends	Absorption edge (eV)	Direct band gap (eV)	Indirect band gap (eV)	Activation energy E_a (eV)
Pure PEOX	5.02	5.09	4.92	0.69
70/30	4.92	4.97	4.81	0.53
50/50	4.95	5.01	4.84	0.59
30/70	4.97	5.03	4.87	0.67
Pure PVOH	5.27	5.41	5.05	0.55

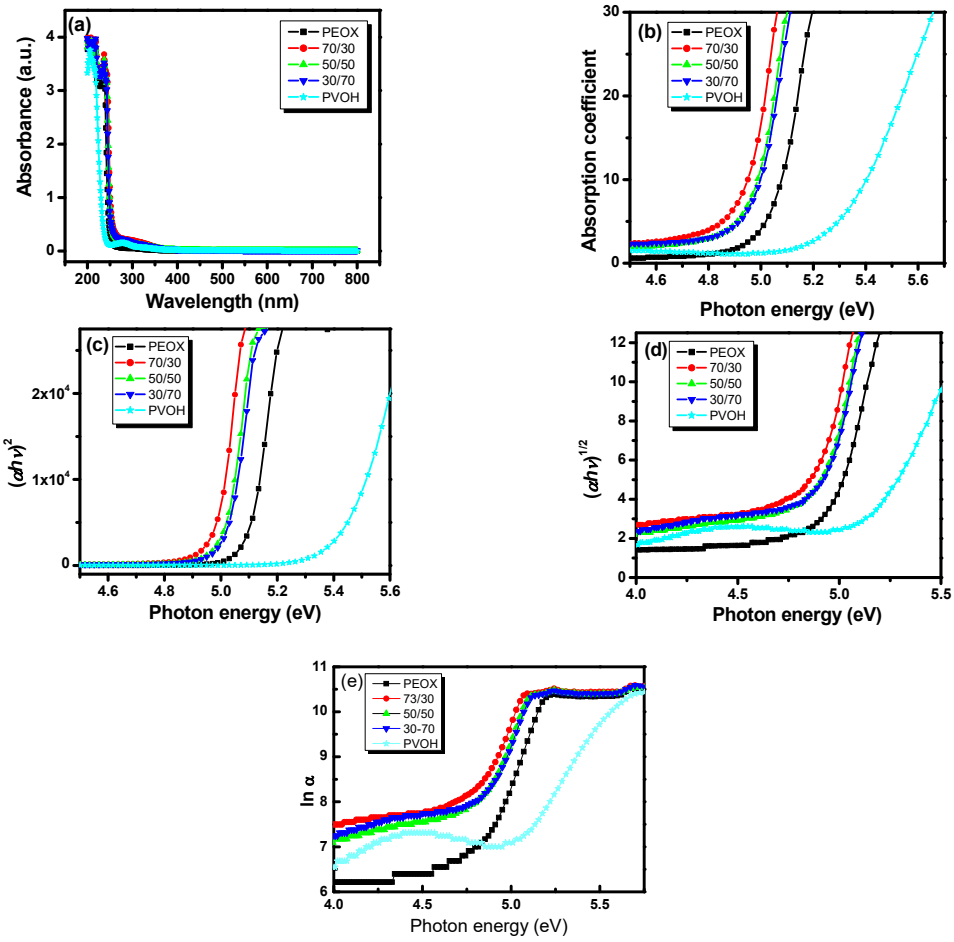

Fig. 2. Plot of (*a*) absorbance versus wavelength (λ), (*b*) absorption coefficient versus photon energy, (*c*) $(\alpha h\nu)^2$versus photon energy, (*d*) $(\alpha h\nu)^{1/2}$ versus photon energy, and (*e*) lnα versus photon energy.

3.3. FTIR Spectral Analysis

FTIR spectroscopic characterization is carried out to find out whether there will be a shift in the peaks in the spectra of blends due to the various interactions between polymers, e.g. hydrogen bonding. FTIR spectra of pure PEOX, pure PVOH, and PEOX/PVOH blends are shown in Fig. 3. Wave numbers for various spectral peaks and their assignments for all the prepared polymer blends are listed in Table 2 [30].

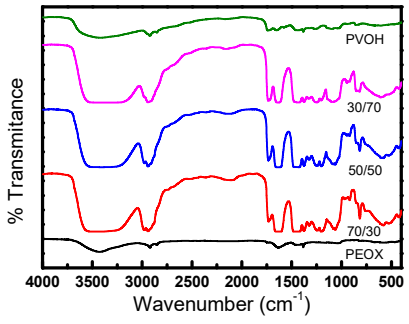

Fig. 3. FTIR spectra of pure PVOH, pure PVA, 70/30, 50/50 and 30/70 blends.

PEOX shows strong absorption band at 3436 cm^{-1} indicating –OH stretching vibrations. The peaks at 2929 and 1631 cm^{-1} are assigned to –CH_2 asymmetric stretching and amide C=O stretching, respectively. The two peaks at 1442 and 1035 cm^{-1} are attributed due to the CH_3 bending and C–N stretching, respectively. PVOH as two strong absorption peaks at 3510 and 2980 cm^{-1} which can be assigned to –OH stretching and –CH_2 asymmetric stretching, respectively. The band corresponding to C=O symmetric stretching occurred at about 1738 cm^{-1}. The bands at 1636, 1455 and 1377 cm^{-1} correspond to C=C stretching, C–H bending, and –CH_2 bending, respectively.

FTIR spectra for PEOX-PVOH polymer blends clearly shows that, there is a clear shift of absorption bands indicating the formation of strong intermolecular bonding between –CH_3 groups in PEOX and –OH groups in PVOH. The 30/70 wt % PEOX-PVOH blend has a maximum shift in the higher wave number side evidencing a formation of strong hydrogen bond. As the PVOH content in the blend increases, the peak intensity diminishes.

Table 2. Assignments of the FTIR characterization of bands of the pure PEOX, pure PVOH and PEOX-PVOH blends.

Wave no. (cm^{-1})	Peak Assignment (PEOX)	Wave no. (cm^{-1})	Peak Assignment (PVOH)	70/30	50/50	30/70
3436	–OH stretching	3421	–OH stretching	3510	3414	3450
2929	$–CH_2$ asymmetric stretching	2922	$–CH_2$ asymmetric stretching	2980	2978	2942
1631	Amide C=O stretching	1738	C=O symmetric stretching	1732	1731	1731
1442	CH_3 bending	1653	C=C stretching	1636	1636	1637
1035	C–N stretching	1437	C–H bending	1455	1432	1427
---	---	1383	$–CH_2$ bending	1377	1375	1376

3. Conclusions

The results shows that PEOX-PVOH polymer blends have been prepared successfully by solution casting method. UV-Vis spectra studies confirm the interaction between PEOX and PVOH, and hence, a structural variation occurred in blend system. This variation decreases with increasing concentration of PVOH, which is reflected in the form of increase in the optical energy gap of the blends. Hence, from this study it can be concluded that, the blend of PEOX/PVOH with 30/70 wt% is most suitable and compatible with enhanced properties. FTIR spectra confirms that, increased bond strength is due to the intermolecular bonding interactions between $–CH_3$ groups of PEOX and –OH groups of PVOH and the interaction is maximum for 30/70 wt% blend.

Acknowledgements

One of the authors (SRM) is thankful to the Vision Group on Science and Technology (VGST), Department of Information Technology, Biotechnology and Science & Technology, Government of Karnataka for providing the financial support under project no. KSTePS/VGST/03/CISEE/ 2015-2016/GRD-470.

References

[1]. F. C. Gaertner, R. Luxenhofer, B. Blechert, R. Jordan and M. Essler, Synthesis, biodistribution and excretion of radiolabeled poly(2-alkyl-2-oxazoline)s, *Journal of Controlled Release*, Vol. 119, Issue 3, 2007, pp. 291-300.

[2]. A. Mero, G. Pasut, L. D. Via, M. W. M. Fijten, U. S. Schubert, R. Hoogenboom and F. M. Veronese, Synthesis and characterization of poly(2-ethyl 2-oxazoline)-conjugates with proteins and drugs: Suitable alternatives to PEG-conjugates?, *Journal of Controlled Release*, Vol. 125, Issue 2, 2008, pp. 87-95.

[3]. S. C. Lee, C. Kim, I. C. Kwon, H. Chung and S. Y. J. Jeong, Polymeric micelles of poly(2-ethyl-2-oxazoline)-block-poly(ε-caprolactone) copolymer as a carrier for paclitaxel, *Journal of Controlled Release*, Vol. 89, Issue 3, 2003, pp. 437-446.

[4]. http://www.sigmaaldrich.com/catalog/product/ aldrich/372846?lang=en&region=IN

[5]. S. Zalipsky, C. B. Hansen, J. M. Oaks and T. M. Allen, Evaluation of blood clearance rates and biodistribution of poly(2-oxazoline)-grafted liposomes, *Journal of Pharmaceutical Sciences*, Vol. 85, Issue 2, 1996, pp. 133-137.

[6]. T. T. Chiu, B. P. Thill and W. J. Fairchok, Poly(2-ethyl-2-oxazoline): A New Water- and Organic-Soluble Adhesive, in Water-soluble polymers, *American Chemical Society,* Chapter 23, 1986, pp. 425-433.

[7]. H. Keskkula and D. R. Paul, Miscibility of polyethyloxazoline with thermoplastic polymers, *Journal of Applied Polymer Science*, Vol. 31, Issue 5, 1986, pp. 1189-1197.

[8]. D. Christova, R. Velichkova, W. Loos, E. J. Goethals and F. D. Prez, New thermo-responsive polymer materials based on poly(2-ethyl-2-oxazoline) segments, *Polymer*, Vol. 44, Issue 8, 2003, pp. 2255-2261.

[9]. H. Keskkula and D. R. Paul, Thermal behavior of polyethyloxazoline, *Journal of Applied Polymer Science*, Vol. 31, Issue 3, 1986, pp. 941-950.

[10]. H. Keskkula, D. R. Paul, P. Young and R. S. Stein, Diffusion of miscible polymers in multilayer films, *Journal of Applied Polymer Science*, Vol. 34, Issue 5, 1987, pp. 1861-1877.

[11]. H. H. Trieu, T. Carls, R. Lim, E. C. Lange, K. M. Anderson, and A. Bruneau, Interosteotic implant comprising a metallic or polymeric material for treatment of spinal disorders, 2007.

[12]. S. D. Jensen, Peroxide/poly(2-ethyl-2-oxazoline) gel compositions of good stability for bleaching of teeth, hair, laundry, 2007.

[13]. M. Torizuka, H. Suzuki, K. Fujiwara, T. Oda, N. Tanaka and K. Rindo, Emulsified, water-in-oil type composition and skin cosmetic preparation, 1997.

[14]. D. K. Hood, Coating composition for forming an inkjet-printable coating on a substrate, 2007.

[15]. K. Kuwahara, H. Nanbu, A. Ibi and Y. Fukuyama, Polymer dispersant for pigment and nonaqueous pigment dispersion containing it, 2007.

[16]. C. H. Wang, C. H. Wang and G. H. Hsiue, Polymeric micelles with a pH-responsive structure as intracellular drug carriers, *Journal of Controlled Release*, Vol. 108, Issue 1, 2005, pp. 140-149.

[17]. G. H. Hsiue, C. H. Wang, C. L. Lo, C. H. Wang, J. P. Li and J. L. Yang, Environmental-sensitive micelles based on poly(2-ethyl-2-oxazoline)-b-poly(l-lactide) diblock copolymer for application in drug delivery, *International Journal of Pharmaceutics*, Vol. 317, Issue 1, 2006, pp. 69-75.

[18]. J. J. Liaw, Integrated semiconductor structure for static random access memory (sram) cells, 2007.

[19]. L. W. Chan, J. S. Hao and P. W. S. Heng, Evaluation of permeability and mechanical properties of composite, *Chemical and Pharmaceutical Bulletin*, Vol. 47, Issue 10, 1999, pp. 1412-1416.

[20]. http://www.sigmaaldrich.com/catalog/product/aldrich/363146?lang=en&region=IN

[21]. J. Tauc, R. Grigorovici and A. Vanku, Optical properties and electronic structure of amorphous germanium, *Physica Statatus Solidi (b)*, Vol. 15, Issue 2, 1966, pp. 627-637.

[22]. M. A. Gaffer and A. Abu El-Fadl, Effect of doping and irradiation on optical parameters of triglycine sulphate single crystals, *Crystal Research Technology*, Vol. 34, Issue 7, 1999, pp. 915-923.

[23]. N. L. Singh, A. Sharma and D. K Avasthi. Effects of high energy (MeV) ion beam irradiation on polyethylene terephthalate, *Nuclear Instruments and Methods in Physics Research Section B*, Vol. 206, 2003, pp. 1120-1123.

[24]. F. Urbach, The long-wavelength edge of photographic sensitivity and of the electronic absorption of solids, *Physical Review*, Vol. 92, Issue 5, 1953, pp. 1324.

[25]. A. Buttafava, G. Consolati, L. DiLandro and M. Mariani, γ-irradiation effects on polyethylene terephthalate studied by positron annihilation lifetime spectroscopy, *Polymer*, Vol. 43, Issue 26, 2002, pp. 7477-1781.

[26]. R. Mishra, et al., Optical and electrical properties of some electron and proton irradiated polymers, *Nuclear Instruments and Methods in Physics Research Section B*, Vol. 168, Issue 1, 2000, pp. 59-64.

[27]. L. Shahada, M. E. Kassem, H. I. Abdelkader and H.M. Hassan, Optical and electrical properties of a new polymer, *Journal of Applied Polymer Science*, Vol. 65, Issue 9, 1997, pp. 1653-1657.

[28]. M. M. El-Samanoudy and A. H. Ammar, Some physical and optical properties of the a-$Se_{85}Sb_xS_{15-x}$ film system, *Physica Statatus Solidi (b)*, Vol. 187, Issue 2, 2001, pp. 611-621.

[29]. C. H. Cholakis, W. Zingg and M. V. Sefton, Effect of heparin–pva hydrogel on platelets in a chronic canine arterio-venous shunt, *Journal of Biomedical Material Research*, Vol. 23, Issue 4, 1989, pp. 417-441.

[30]. D. Pavia, G. M. Lampman, G. S. Kriz, J. R. Vyvyan, Introduction to spectroscopy, 5th edition, *Cengage Learning*, 2015.

Published by International Frequency Sensor Association (IFSA) Publishing, S. L., 2017 (http://www.sensorsportal.com).

Sensors & Transducers, Vol. 210, Issue 3, March 2017, pp. 38-41

www.sensorsportal.com

Sensors & Transducers

Published by IFSA Publishing, S. L., 2017
http://www.sensorsportal.com

Green Synthesis and Characterizations of Flower Shaped CuO Nanoparticles for Biodiesel Application

[1] Rintu Varghese, [2] Joy Prabu H. and [3*] Johnson I.

[1, 2, 3] Centre for Nanoscience and Applied Thermodynamics, Department of Physics,
St. Joseph's College, Trichy – 620002, Tamilnadu, India
[*] E-mail: jnaadarsh@hotmail.com

Received: 9 January 2017 /Accepted: 3 March 2017 /Published: 31 March 2017

Abstract: Nanomaterials are primary candidates to play a key role in energy future. In this work, plant-mediated green synthesis of CuO nanoparticles was studied. The CuO nanoparticles were used as the catalysts for the production of biodiesel from coconut oil. An aqueous extract of Centella Asiatica leaves was used as a bio-reducing agent for the synthesis of CuO nanoparticles. This biocatalyst was characterized by using different techniques (FTIR, UV-Vis spectroscopy, XRD, FESEM with EDX) which were confirmed the formation of CuO nanoparticles. Further, the presences of FAME (Fatty Acid Methyl Ester) groups at the produced biodiesel were confirmed using both the GC-MS and FTIR analysis. From this work, it has been concluded that the plant extract mediated synthesis of CuO nanoparticles is quite simple, cost-effective and environmentally friendly. The produced biodiesel from coconut oil is considered to be a potential source for alternative conventional fuel.

Keywords: Green synthesis, Biodiesel, GCMS, Nanoparticles.

1. Introduction

Recently researchers are very much interested in producing biofuel, using nanomaterials as catalysts in an efficient way [1-3]. Nanomaterials have high catalytic activity, large specific surface area, high resistance to saponification reaction and good rigidity when compared with their bulk counterpart [4-7]. The available reports on biodiesel production using nanomaterials are relatively few [8-11].

The plant extract mediated synthesis of CuO nanoparticles is cost effective and eco- friendly [12-15]. Moreover, the plant extracts are possibly enriched with the presence of broad ranges of biomolecules such as alkaloids, terpenoids, phenols, and flavonoids etc. which were considered as bio-reducing agent [16-20]. Centella Asiatica is an important medicinal plant in Siddha and Ayurveda [21-23].

In the present work, the synthesized bio CuO nanoparticles were used as catalysts for the production of biodiesel. All the characterization studies clearly proved the formation of nanoparticles. The presence of methyl ester groups in the produced biodiesel was confirmed using both gas chromatography-mass spectrometry (GC-MS) and infrared spectroscopy (FTIR).

2. Materials and Methods

2.1. Materials

All the reagents were of analytical grade and they were used without further purification. Copper acetate [Cu $(CH_3COO)_2$] and Methanol (99.9 % purity) were obtained from Merck, Germany. The plant Centella Asiatica has been collected from remote villages of

Trichy. Coconut oil was purchased from a local market.

2.2. Preparation of CuO Nanocatalyst

The leaves (20 g) collected have been washed and boiled with de-ionized water for 15 minutes. The sample was taken out and kept in a place to attain the room temperature. Again it was filtered successively through filter paper and stored at 4 °C. The aqueous copper acetate and leaf extracts were taken in 4:1 ratio and the solution was exposed to sunlight for 3 hours. After the completion of the reaction, the precipitate was centrifuged (8000 rpm) and dried in hot air oven at 80 ^{0} C.

2.3. Transesterification Procedure

The flask was filled with the reaction mixture (1:3 oil/methanol and 1 wt. % of CuO) and mixed thoroughly at a constant temperature of 60 ^{0}C with the help of a magnetic stirrer. After the completion of the reaction, the mixture was cooled to room temperature and the top layer of the biodiesel phase has been separated.

3. Results and Discussion

3.1. UV-Vis Analysis

In Fig. 1 an observed peak at 393 nm is assigned to the surface plasmon resonance band of the CuO nanoparticles. This is analogous with the existing literature values [24].

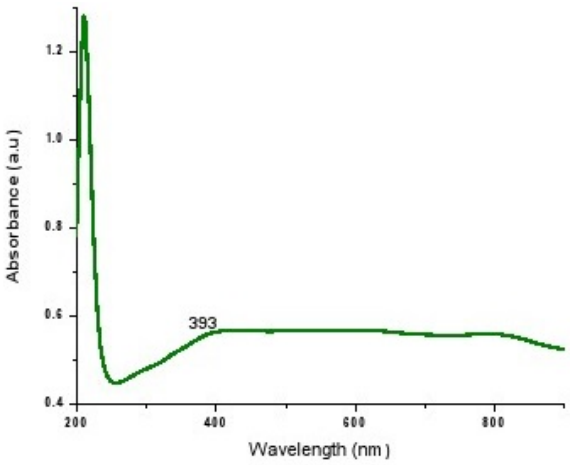

Fig. 1. UV-Vis graph of CuO nanoparticles.

3.2. FTIR Analysis

In the Fig. 2 the peak at 1079 cm^{-1} indicates the presence of C-O stretching and the peak at 1618 cm^{-1} represents ketone group suggesting the presence of flavonones. The C-H stretches of alkanes appear at 2934 cm^{-1} and the peak at 3430 cm^{-1} mainly corresponds to the O-H groups.

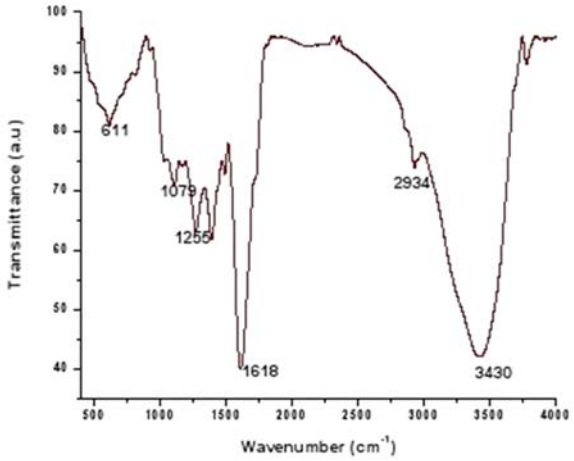

Fig. 2. FTIR pattern of CuO nanoparticles.

3.3. XRD Analysis

No impurity peaks other than CuO were observed in the XRD pattern in Fig. 3. The major peaks at 32.4^0, 35.5^0, 38.7^0, 48.8^0 and 66.2^0 are incomparable with JCPDS card no (65-2309). The average crystallite size of the CuO nanoparticles calculated by Debye–Scherer's formula is 40 nm.

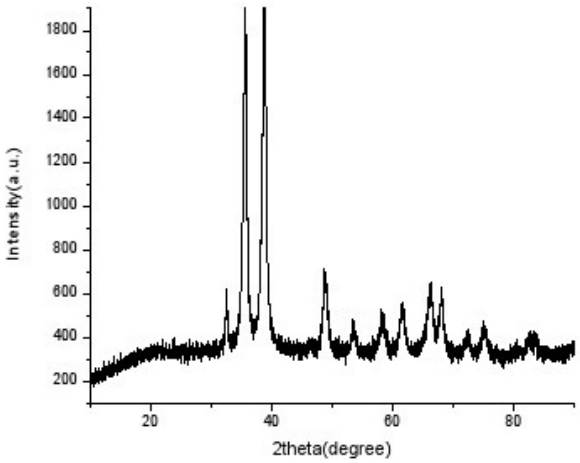

Fig. 3. XRD pattern of CuO nanoparticles.

3.4. FESEM with EDX Analysis

The surface morphology of the nanoparticles was obtained by Field Emission Scanning Microscopy (FESEM). The bio-reduced CuO nanoparticles resemble small spherical flower shape (Fig. 4). The EDX result of Fig. 5 shows the elemental composition of Cu, O along with some C and P.

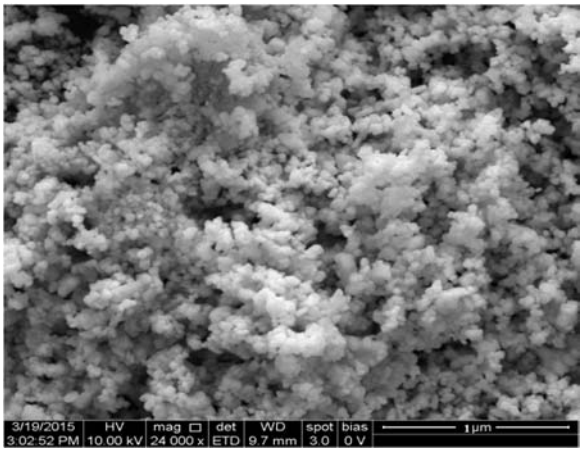

Fig. 4. FESEM image of CuO nanoparticles.

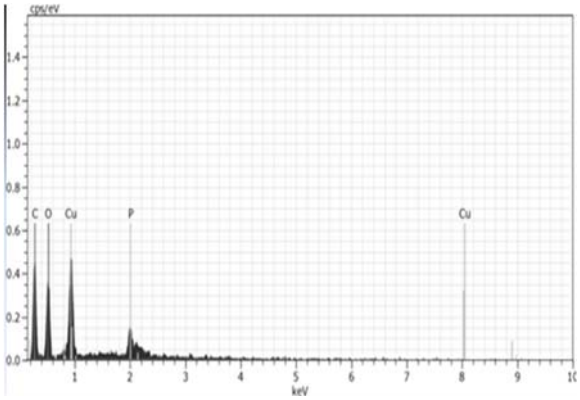

Fig. 5. EDX analysis of CuO nanoparticles.

3.5. GCMS Analysis

The composition of coconut oil and the biodiesel were determined using GC-MS analysis. The chemical composition of coconut oil and biodiesel is briefly listed in Table 1. The maximum FAME conversion calculated is 78.58 %. The most abundant FAME found in the coconut oil biodiesel is 10-Bromodecanoic acid methyl ester.

Table 1. GC-MS composition analysis.

Type of fatty acid (FA)	Composition analysis		Total weight (%)	
	coconut oil	coconut oil biodiesel	coconut oil	coconut oil biodiesel
Saturated	12:0 14:0 8:0 16:0 10:0 18:0	16:0 8:0 11:0 14:0	94.15	18.21
Un-saturated	18:1 18:2	11:1 16:1 18:1	5.85	78.58

3.6. FTIR Analysis

The FTIR spectrum of produced biodiesel from coconut oil is shown in Fig. 6. From the literature, coconut oil biodiesel samples are very much similar to that of standard petrodiesel and biodiesel sample [20]. The two bands observed at 1459.56 cm^{-1} and 1748.33 cm^{-1} in sample indicate the presence of two groups namely methyl (CH_3) and ester respectively.

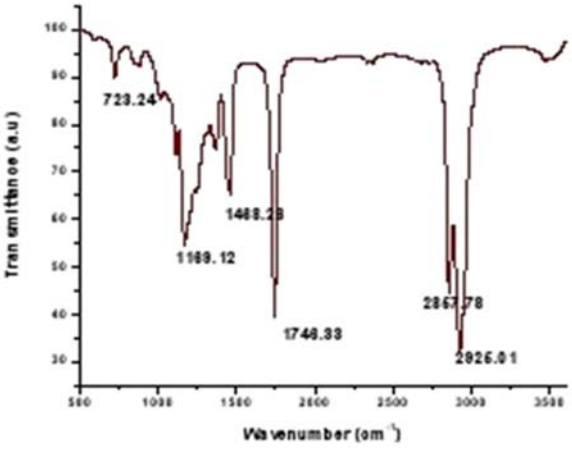

Fig. 6. FTIR spectra of biodiesel from coconut oil.

4. Conclusion

The production of biodiesel from coconut oil with methanol was successfully synthesized using CuO nanocatalyst. The biocatalyst was characterized using different techniques which confirm the formation of CuO nanoparticles. The presence of FAME groups at the produced biodiesel also confirmed by using GC-MS and FTIR analysis. The study demonstrates that the leaves of Centella Asiatica are content-rich and good sources for the fabrication of CuO nanoparticles. In conclusion, the biodiesel synthesized from coconut oil can be considered as the potential source of energy which can easily replace all the other alternative conventional fuels.

References

[1]. Alhassan F. H., Rashid U., Taufiq-Yap Y. H., Optimization of simultaneous production of waste cooking oil based-biodiesel using iron-manganese doped zirconia-supported molybdenum oxide nanoparticles catalyst, *Journal of Renewable and Sustainable Energy*, 8, 2016, p. 033101.

[2]. Alves M. B., Medeiros F., Sousa M. H., Rubim J. C., Suarez P. A., Cadmium and Tin Magnetic Nanocatalysts Useful for Biodiesel Production, *Journal of the Brazilian Chemical Society*, 25, 2014, pp. 2304-2313.

[3]. De S., Luque R., Nanomaterials for the Production of Biofuels. Nanomaterials for Sustainable Energy, *Springer*, 2016, p. 559-582.

[4]. Rengasamy M., Mohanraj S., Vardhan S. H., Balaji R., Pugalenthi V., Transesterification of castor oil using nano-sized iron catalyst for the production of biodiesel, *Journal of Chemical and Pharmaceutical Sciences*, 974, 2014, pp. 2115.

[5]. Mguni L. L., Meijboom R., Jalama K., Biodiesel production over nano-MgO supported on titania, *World Acad Sci, Eng Technol,* 64, 2012.

[6]. Babu P. S., Mamilla V. R., Methanolysis of castor oil for production of biodiesel, *International Journal of Advanced Engineering Technology,* 3, 2012, pp. 146-148.

[7]. Luo F., Chen Z., Megharaj M., Naidu R., Biomolecules in grape leaf extract involved in one-step synthesis of iron-based nanoparticles, *RSC Advances*, 4, 2014, pp. 53467-53474.

[8]. Wu H., Zhang J., Wei Q., Zheng J., Zhang J., Transesterification of soybean oil to biodiesel using zeolite supported CaO as strong base catalysts, *Fuel Processing Technology,* 109, 2013, pp. 13-18.

[9]. Tahvildari K., Anaraki Y. N., Fazaeli R., Mirpanji S., Delrish E., The study of CaO and MgO heterogenic nano-catalyst coupling on transesterification reaction efficacy in the production of biodiesel from recycled cooking oil, *Journal of Environmental Health Science and Engineering*, 13, 2015, p. 1.

[10]. Mukenga M., Biodiesel production over supported Zinc Oxide nano-particles: Faculty of Engineering and the Built Environment, *University of Johannesburg*, 2012.

[11]. Mukenga M., Muzenda E., Jalama K., Meijboom R., Biodiesel production from soybean oil over TiO2 supported nano-ZnO, World Academy of Science, Engineering and Technology, *International Journal of Chemical, Molecular, Nuclear, Materials and Metallurgical Engineering*, 6, 2012, pp. 6-10.

[12]. Atta A. M., El-Mahdy G. A., Al-Lohedan H. A., Ezzat A. O., Electrochemical behaviour of Mild Steel in Acidic Medium Based on Eco-Friendly Stabilized Monodisperse Silver Nanocomposite, *Int J Electrochem Sci,* 9, 2014, pp. 8226-8238.

[13]. Genuino H., Huang H., Njagi E., Stafford L., Suib S. L., A review of green synthesis of nanophase inorganic materials for green chemistry applications, *Handbook of Green Chemistry,* 2012.

[14]. Shivakumar Singh P., Vidyasagar G., Green synthesis, characterization and antimicrobial activity of Silver Nanoparticles by using Sterculia foetida L. young leaves aqueous extract, *International Journal of Green Chemistry and Bioprocess,* 4, 2014, pp. 1-5.

[15]. Joy Prabu H., Johnson I., Flower-Shaped CuO Nanostructure Synthesized by Sonochemical Method and the effect of NaOH concentrations, *International Journal of Advanced Research,* 3, 2015, pp. 1091 – 1096.

[16]. Sini S., Malathy N., Phytochemical characteristics of Ichnocarpus frutescens. (L) R. Br., *Ancient science of life,* 25, 2006, pp. 71-75.

[17]. Saboo S. S., Tapadiya G., Metku M., Vaidya V., Khadabadi S., Pharmacognostic and Physicochemical investigation of Pterospermum acerifolium Willd leaves (Sterculiaceae), *Pharmacognosy Journal*, Issue Vol.2, Issue 6, February 2010, pp. 83–89.

[18]. Geethalakshmi R., Sarada D., Marimuthu P., Evaluation of antimicrobial and antioxidant potentials of Trianthema decandra L., *Asian Journal of Biotechnology*, 2, 2010, pp. 225-231.

[19]. Ramalakshmi C., Ranjitsingh A., Kalirajan K., Kalirajan A., Athinarayanan G., Mariselvam R. A., Preliminary screening of the Medicinal Plant Couroupita guianensis for its Antimicrobial Potential against Clinical and Fish-borne pathogens, *Elixir Appl Biol,* 57, 2013, pp. 1405514057.

[20]. Johnson I., Prabu H. J., Green synthesis and characterization of silver nanoparticles by leaf extracts of Cycas circinalis, Ficus amplissima, Commelina benghalensis and Lippia nodiflora, *International Nano Letters,* 2015, 5, pp. 43-51.

[21]. Gohil K. J., Patel J. A., Gajjar A. K., Pharmacological review on Centella asiatica: a potential herbal cure-all, *Indian Journal of Pharmaceutical Sciences,* 72, 2010, pp. 546.

[22]. Babykutty S., Padikkala J., Sathiadevan P., Vijayakurup V., Azis T., Srinivas P., et al., Apoptosis induction of Centella asiatica on human breast cancer cells, *African Journal of Traditional, Complementary and Alternative Medicines*, 6, 2009.

[23]. Zheng C. J., Qin L., Chemical components of Centella asiatica and their bioactivities, *Journal of Chinese Integrative Medicine,* 5, 2007, pp. 348-351.

[24]. Rahman A., Ismail A., Jumbianti D., Magdalena S., Sudrajat H., Synthesis of copper oxide nano particles by using Phormidium cyanobacterium, *Indonesian Journal of Chemistry*, 9, 2010, pp. 355-60.

[25]. Hussain S. T., Ali S. A., Bano A., Mahmood T., Use of nanotechnology for the production of biofuels from butchery waste, *International Journal of the Physical Sciences*, 6, 2011, pp. 7271-7279.

Sensors & Transducers, Vol. 210, Issue 3, March 2017, pp. 42-49

www.sensorsportal.com

Sensors & Transducers

Published by IFSA Publishing, S. L., 2017
http://www.sensorsportal.com

Application of Acoustic Techniques in Thermal Power Plants

[1] T. K. Sai and [2] K. A. Reddy
[1] NTPC, Delhi, Indian 110003
[2] KITSW, Warangal, India 506003
[1] Tel.: 91 9440918146
[1] E-mail: tksai123@rediffmail.com

Received: 25 January 2017 /Accepted: 3 March 2017 /Published: 31 March 2017

Abstract: In the power plant, for over two decades, use of acoustic techniques were limited only to detect steam leaks in the Boiler. Even this application has certain limitations like interfering background noises, sound wave attenuations, and inaccessibility of desired sensor locations. For these reasons a proper specialized technique, generally unique to a given application, be employed to ensure optimum sensitivity. This paper presents an innovative approach towards use of acoustic techniques in a 500 MW thermal power plant. The application areas include clinker /sagging detection, steam leak detection and combustion optimization. In the steam leak detection and combustion optimization, the present day limitations are overcome. The use of acoustic technology to detect clinker formation is a new concept. All the three applications are designed and implemented in a 500 MW power plant.

Keywords: Distributed control system, Acoustic measurement, Power station, Clinker, Tube leak, Combustion.

1. Introduction

Acoustics deals with the production, control, transmission, reception, and effects of sound. It is indispensable that abnormalities in power plant be detected in their early stages so that power failures will not seriously affect public life and vital installations and infrastructure. To this end, power plant engineers have introduced a range of equipment monitoring systems, and development work is still going on. These monitoring systems are fitted with a number of sensors that work like human sense organs. Acoustic sensors are one of the most important kinds of these sensors [1].

This paper presents a method of detecting abnormalities like boiler tube leakage, clinker formation and unbalance temperature profile in the combustion zone using acoustic sensors. These abnormalities do not create any catastrophic situation but if ignored will lead to secondary damages and also unit outages.

2. ASLD System

The Acoustic Steam Leak Detection (ASLD) system works on the principle of detecting the sound waves emanating from the steam leak, processing the same and then indicating the quantum of steam leak and the location. The conventional method of detecting boiler tube steam leaks is by ear. But, this method would lead to secondary damages in the boiler tubes due the delayed actions. In comparison, the computer-based acoustic tube leak-detection system uses FFT (Fast Fourier Transform) to generate audio spectrums and analyze plant conditions. When a leak is detected by a change in the sound patterns, alarms are activated and the fault is localized. Mimic

diagrams enable plant operators to identify the affected area and plot the progress of the leak for planned shutdowns.

The boiler is divided into 24 zones and in each zone a wave guide is mounted on the stub provided in that zone. The wave guide is installed at an angle of 45 degree to the vertical axis of the water wall panel and is welded to the seal box filled with refractory. The wave guide houses the acoustic sensor which is connected to the isolator unit at the boiler side and further processed with signal processing electronics at the Control room as shown in Fig. 1.

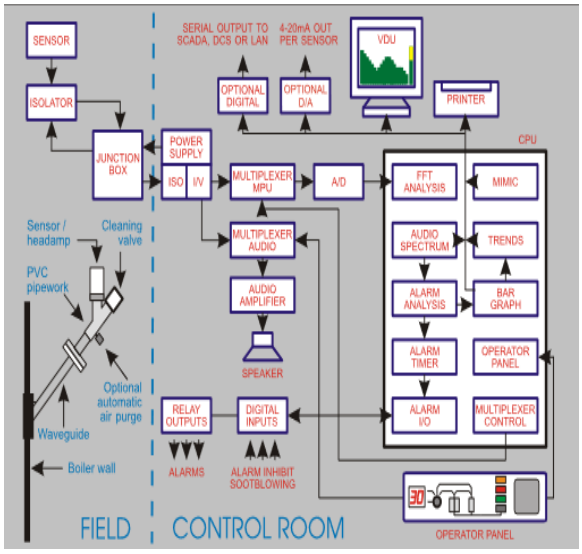

Fig. 1. Architecture of ASLD.

The wave guide houses the acoustic sensor assembly with integrated head amplifiers along with the essential components required for its sustained operation such as the air purging arrangement, isolation valve, heat insulated spacers and heat insulated coupling as shown in Fig. 2.

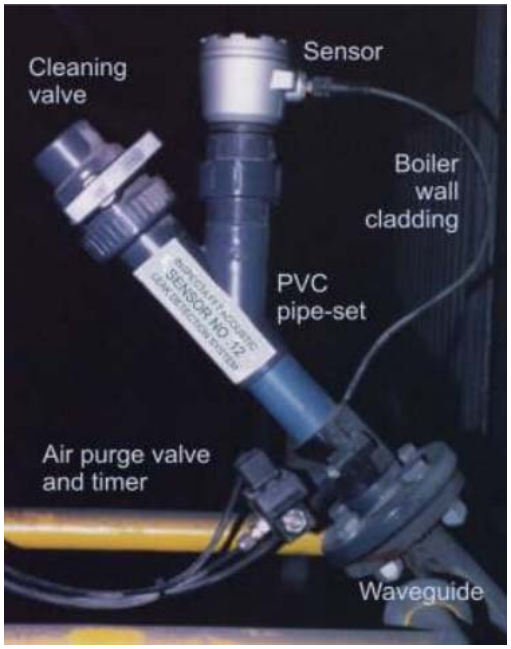

Fig. 2. Wave guide assembly.

This coupling is used to avoid heat conduction to the sensor assembly. A variation in the normal sound frequency and amplitude is used to detect steam leaks.

In leak detection applications, the most important factor to consider is background noise within the propagation medium of interest. Almost all background noise can be characterized as white noise combined with discrete frequency noise. White noise can be defined as containing components at all frequencies within a range or band of interest. Both normal boiler noise and leak noise are considered to be white noise. Boiler noise is best described as low frequency white noise (rumbling) while leak noise is best described as higher frequency white noise (hissing).

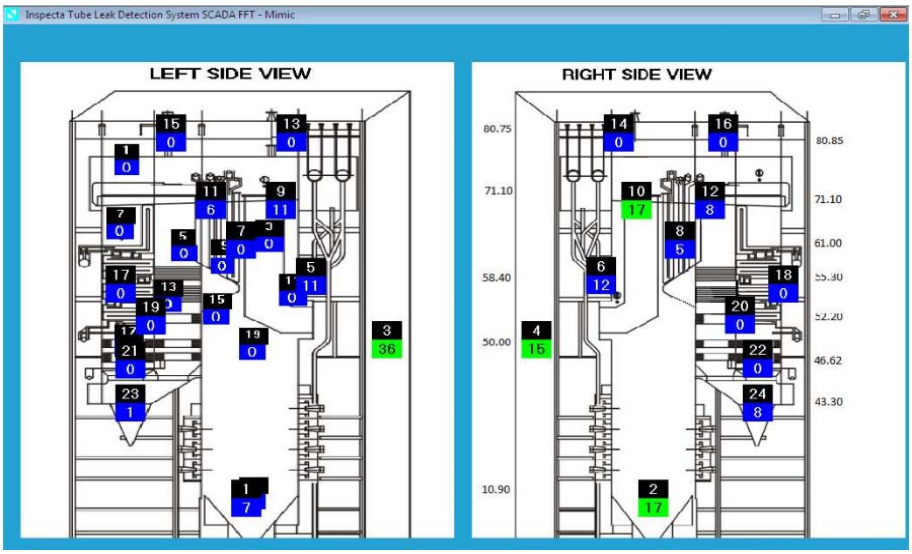

Fig. 3. Layout of sensors in 500 MW Boiler.

The mimic layout of 24 nos sensors is shown in Fig. 3. The bar graph of the 24 sensors is shown in Fig. 4 and the trend is shown in Fig. 5.

Latest signal processing approach is implemented wherein the Signal processing modules consists of audio spectrum analyzers based on FFT techniques with central processor unit, programmable memory and an interface card with a high-speed analog-to-digital converter and isolated input/output circuits for interfacing with field wiring and an operator's console. The incoming signal is digitized and FFT is performed to produce the frequency spectrum. This spectrum memorized and compared with a previous spectrum that is characteristic of normal background noise. The comparison is done by software means. The normal background noise is stored as a reference spectrum when the unit is running at full load with no tube leakage. If a considerable difference exists between these two signals, a leak is indicated. The benefits of using FFT based acoustic detection system includes the early detection of tube leaks, the avoidance of unscheduled outages, early steam-leak detection and an increase in boiler-tube life, operating performance, power station uptime, operating profits and personal safety.

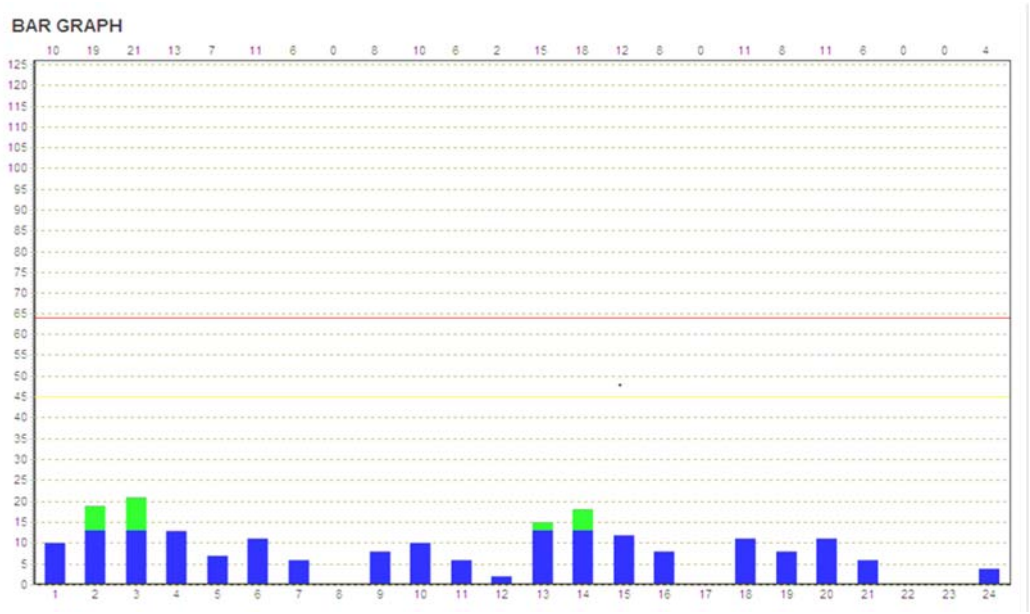

Fig. 4. Bar graph of 24 sensors.

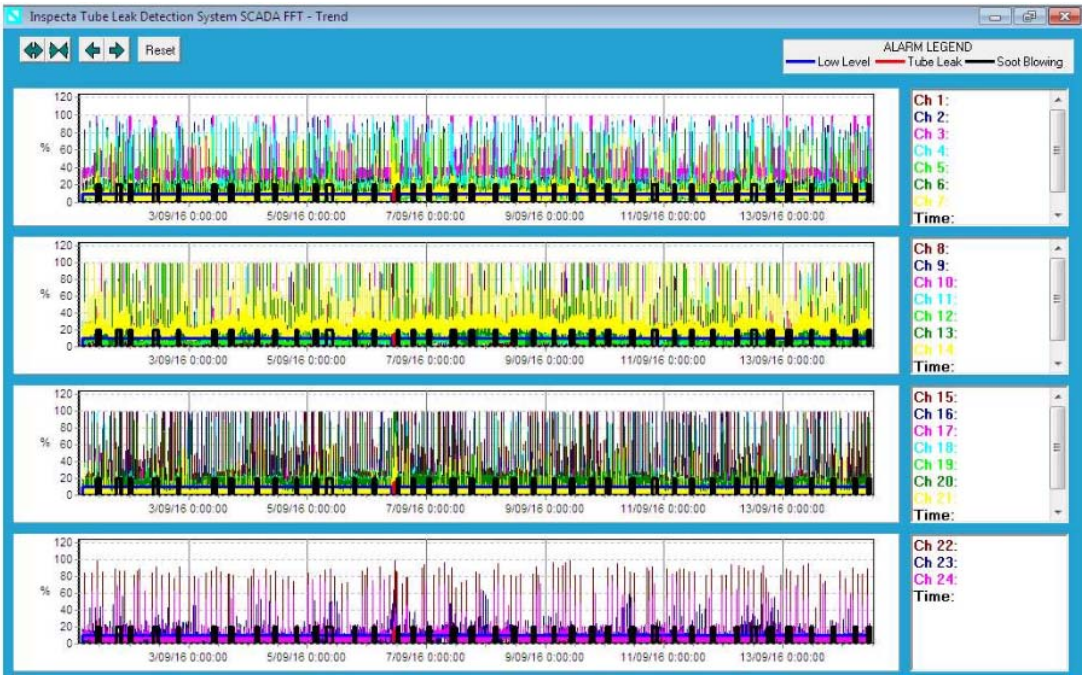

Fig. 5. Trend of 24 sensors.

3. Slagging and Clinkering

Slagging and Clinkering are a critical in the safe running of boilers of thermal power plants as this may lead to forced outage of the Boiler. Slagging is the deposition of ash on furnace walls which tends to solidify due to the lower temperature of the boiler tube. Clinker formation occurs due to low quality coal having low gross calorific value, high ash content, high mineral content, low fusion temperature of ash or over firing. Clinker formation may also occur due to improper air fuel mixture in the furnace, change in coal quality etc. There are several existing technologies to minimize the slagging and clinkering problems in boilers, such as pulse detonation wave technology, intelligent shoot blower, anti-fouling coatings, chemical treatment technology, strain gauges, measurement of temperature in bottom hopper etc. [3]. But they have their own limitations. These techniques have certain drawbacks such as very expensive to implement and also, the indication is not instantaneous owing to the fact that they primarily rely on change in primary parameter (like temperature) as the sensing method which inherently is a slow process. Hence generally it is detected by variation of other derivative parameters.

Detection of clinker formation at an early stage is helpful because when the clinker falls into bottom ash, it disturbs the furnace flame, pressure and drum level occasionally causing Boiler trip. In this paper, a novel approach is proposed for detecting the rate of slag formation in the furnace by sensing the periodical fall of clinker. It gives an early indication to the operator to take preventive and corrective action. This approach focuses on being cost effective by utilizing the existing ASLD of the boiler as the primary sensing medium. The proposed basic approach has been validated with implementation in a 500 MW thermal power plant.

The Proposed system of acoustic clinker fall detection focuses on an effective and reliable method to detect in real time when lumps of clinker fall into the furnace by sensing the sound wave generated when the lump of clinker hits the bottom ash hopper. A deep thud is generated when the mass of clinker falls into the bottom ash hopper. This also creates a small disturbance in furnace pressure proportional to the size and inherent energy of the lump of clinker.

On detailed analysis of the audio spectrum generated using real time audio spectrum analysis software, it was found that when the lump of clinker hits the water in the bottom ash hopper, a peak is generated between the 20 Hz to 1 kHz frequency band in the audio spectrum. This important finding formed the base of the acoustic clinker fall detector. The existing ASLD is extended for the proposed system.

3.1. System Design Considerations

Fig. 6 shows the designed clinker detector circuit. The audio input from the ASLD system is sent to a low pass filter with cut off at 1.5 kHz. The boiler is a very noisy area with continuous low frequency combustion noise between 20 Hz to 100 Hz. As our desired bandwidth of 20 Hz-1.5 kHz is also polluted with this combustion noise, a background noise suppressor circuit subtracts the low frequency continuous combustion noise below 100 Hz. A comparator circuit was designed which gave a high pulse and triggered a relay whenever the input signal crossed the threshold value , the limit value being set after deployment at site by means of a potentiometer carefully so that it does not falsely trigger due to boiler combustion noise . In the present iteration, two comparator circuits are used, one set at a low threshold and the other set at a higher threshold to indicate fall of small clinker and fall of large clinker respectively. The relay outputs are connected to digital input cards in the DCS system for the purpose of storing and analysis.

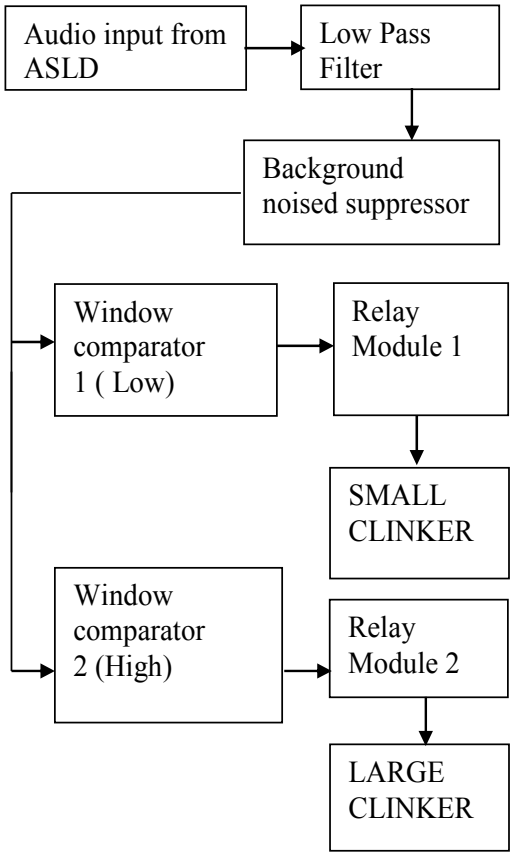

Fig. 6. Clinker detector design.

The existing use for ASLD remained unaffected by this connection thus effectively making them dual purpose detectors for both steam leakage and clinker fall detection. Comparator 1 was set to a low threshold of 50 mV and comparator 2 was set to a higher threshold of 90 mV. Both the settings were done after experimental analysis of the boiler noise. The relay outputs of comparator 1 & comparator 2 were connected to DCS. The system was put under continuous monitoring. Several relationships between furnace pressure and size of clinker falling were established.

3.2. Analysis

On analysis of several samples recorded at different times throughout the operation of the unit at a load of 500 MW, few observations are made.

1. It was observed that when a peak is created between 20 Hz to 500 Hz with amplitude of - 15 dB to - 5 dB, a large size clinker has fallen

2. When a peak is created between 500 Hz to 1000 Hz with a similar amplitude range, a small size clinker has fallen.

3. The combustion noise which is generated continuously when the unit is running has been found to have maximum energy in the 20 Hz to 1500 Hz band with an amplitude range of - 20dB to -30 db.

4. During Soot blowing with steam pressure of 9.5 kg/cm2, the noise generated is between 800 Hz to 1500 Hz with an amplitude range of - 30dB to -4 dB.

Hence, with reference to Fig. 7, it is inferred that Clinker falling is characterized by low frequency and high amplitude signal.

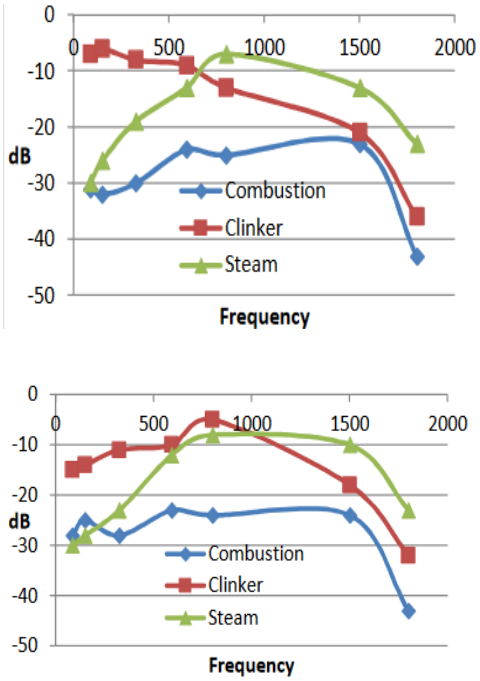

Fig. 7. Frequency versus dB plot of furnace sounds.

Based on the above consideration, logic is developed in the DCS system to annunciate clinker fall based on fall of clinker in unit time. (Number of clinker falls / time).

The Four indications generated in DCS are:

a) Category 1 Normal – 4 to 9 falls of small size clinker in 120 seconds.

b) Category 1 High – More than 10 falls of small size clinker in 120 seconds.

c) Category 2 Normal –5 to 10 falls of large size clinker in 120 seconds.

d) Category 2 High– More than 11 falls of large size clinker in 120 seconds.

The category inferences were made when Unit load is at 500 MW with coal flow 300 Ton per hour with coal calorific value of 3500 kcal/kg and average ash content of 30%. Graphics for the above logic were implemented in the DCS system with trend plots for easy analysis as shown in Fig. 8.

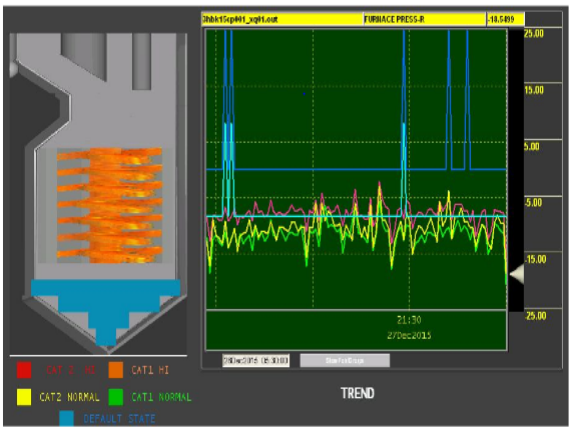

Fig. 8. Trend plots for clinker falling.

4. Acoustic Pyrometer

Acoustic pyrometer is a device instrument that provides measurement of high combustion-gas temperatures within boilers and furnaces. It is a nonintrusive method which works on the principle that the speed of sound in a gas is proportional to the temperature of that gas. An acoustic transmitter and receiver are located on the outside of opposing walls of the boiler/furnace, and a low intensity acoustic signal is launched through the gas stream. Since the distance between the transmitter and receiver is known and fixed, the average temperature of the gas along the acoustic path is computed from an accurate measurement of the sound signal's transit time.

4.1. Principle of Operation

Acoustic Pyrometry is a non-contact method based on the relationship of between the speed of sound and the density of the medium through which it travels. It is well known that the speed of sound varies with the temperature of the medium through which it travels and that changes in speed sound can therefore provide a direct measurement of the medium's temperature.

The relationship is based on the Ideal Gas Law:

$$p = \rho RT,$$

where p is the pressure, ρ, is the density, R is the specific universal gas constant, T is the temperature.

And on the relationship between the speed of sound and the ratio of the pressure to the density given by:

$$c^2 = \gamma p/\rho,$$

where c is the speed of sound and γ is the ratio of the specific heats at constant pressure and volume, respectively.

Combining these two relationships yields:

$$c = (\gamma RT)^{1/2}$$

which is the basic relationship between the speed of sound and the temperature.

These relationships imply that all that is required for the temperature measurement is a transmitter to produce a sound wave at a specific time, and a receiver at a known distance to measure the arrival time of the sound wave, determine the sound speed, and compute the temperature [4]. Speed is directly proportional to the square root of the temperature. The schematic layout is shown in Fig. 9. Plant air is used for sending acoustic signals and each one of the transmitters is also and receiver, so known as the transceiver. At a time one acts as a transmitter and other as a receiver. Signal once received by the receiver passes through piezo-microphone and gets converted into electrical signal and then enters into the control unit as an input which gives 4-20 mA as output.

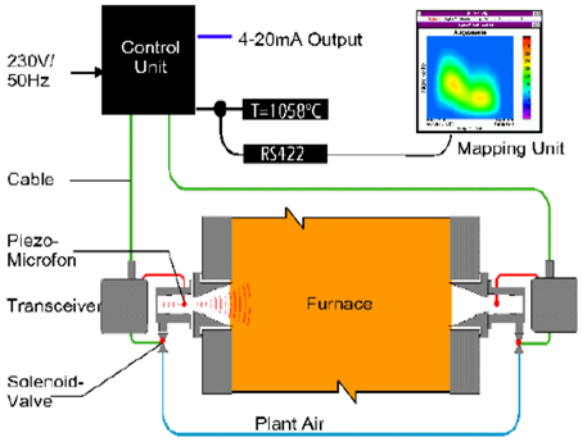

Fig. 9. Layout of Acoustic Pyrometer system.

Finally output through the software gives thermal gradient of the zone as the final output either in the form of Isothermal map or Area Plot as shown in Figs. 10 and 11 respectively.

For efficient combustion it is mandatory to maintain a balanced Furnace Temperature Profile. Whenever unbalance in fire ball or shifting of flame is observed, the acoustic pyrometer indicates the necessary action to be taken thereby optimizing the combustion process. As an example, in Unit 1 at 500 MW with MILL ABCFGJ and K in service, the temperature profile is unbalanced along with two temperature zone in the middle of fire ball as shown in Fig. 12. The unbalance fire ball will result in poor combustion.

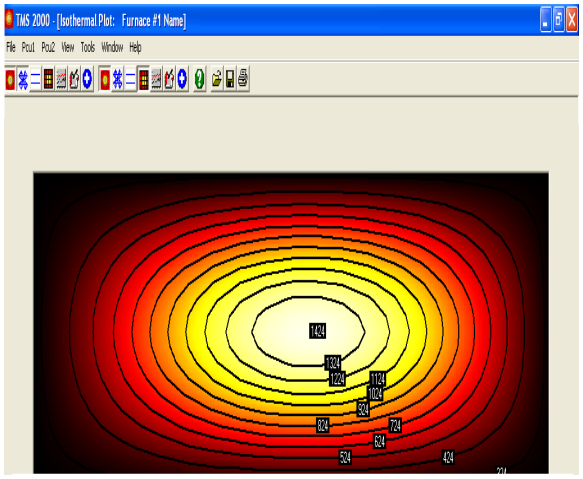

Fig. 10. Isothermal map.

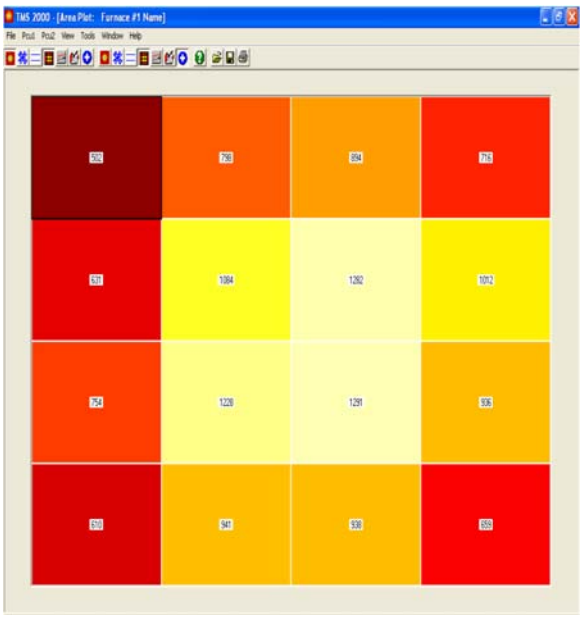

Fig. 11. Area plotting by acoustic pyrometer.

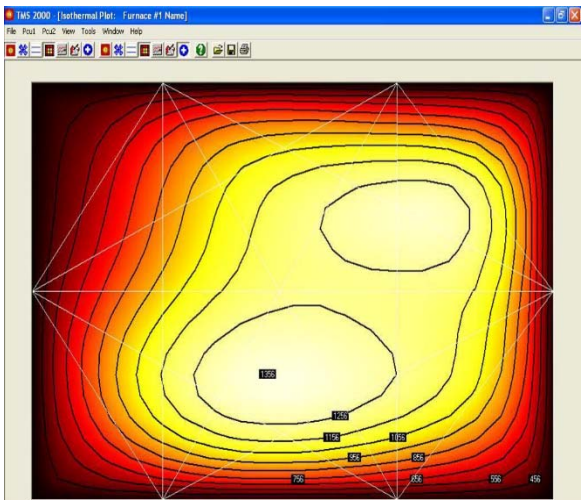

Fig. 12. Temperature profile with 2 zones.

After Mill change over from K to E, at 500 MW with mill ABCEFGJ in service, the temperature profile is now balanced as shown in Fig. 13. There is one temperature zone and hence the fire ball is stable thereby the combustion efficiency improves.

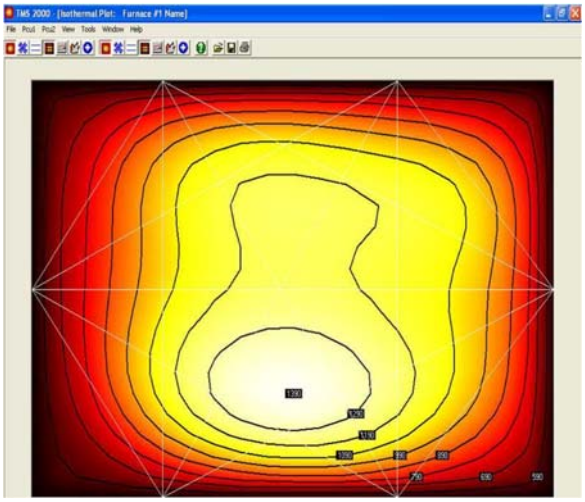

Fig. 13. Balanced temperature profile.

4.2. Limitations of Acoustic Pyrometer

The main drawback of the sensor is the reliability to generate sound signals loud enough to be detected in the presence of considerable background noise. This drawback has been overcome recently with the development of patented technology which has a high intensity pneumatic sound generator, coupled with an advanced signal detection algorithms. The sound generator produces a high-energy sound wave (over 170 dB) using a unique patented pneumatic device as shown in Figs. 14 and 15 [5].

Fig. 14. Arrangement of pneumatic device.

The sound wave produced by the pyrometer has a sharp leading edge that is propagated concentrically from the generator. This enables the pyrometer to accurately measure temperatures to within + 1 % over a range of 0 to 1900 ^{0}C, even in the presence of considerable noise.

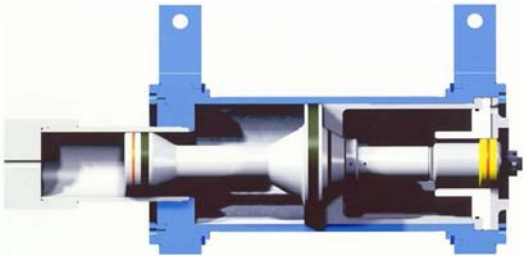

Fig. 15. New pneumatic device.

The new sound source enables the measurement of gas temperatures in furnaces over 30 meters wide, and within sootblower lanes (up to 25 m), which has previously not been possible. It also permits the use of long (up to 13 meter) pipes to deliver the sound to the desired measurement location, such as the tip of the boiler "bullnose". This permits mounting arrangements through windboxes and/or around obstructions without affecting the quality of the resultant measurement. The high-energy sound wave also enables the use of smaller and more sophisticated receivers that can be readily installed through boiler tube webbing using 12 mm by 25 mm slots. This has had a major impact on reducing installation costs and eliminating the need to bend boiler tubes [5].

4.3. Advantages of Acoustic Pyrometer

A. Soot Blowing Operations.

Soot blowing operations has been optimized by the use of Acoustic Pyrometer resulting in significant reduction in steam combustion and over blowing operations.

B. Reduction in Superheater & Reheater spray leads to reduction in efficiency, so once real time temperature gradient is known to operator, combustion conditions are analyzed to reduce over heating combustion.

C. Reduction in Clinkering Problem.

Nowadays blending of imported coal with Indian domestic coal is a common phenomenon in all NTPC stations and Clinkering is a problem attached with blending. Clinkering depends on ash fusion temperature. Real time temperature zone of the combustion area proves to be very advantageous for the boiler desk operator in controlling temperature well below ash fusion temperature.

D. Reduction in NOX formation.

High temperature leads to NOX formation, polluting our environment. Real time temperature assessment proves beneficial in saving our environment.

E. Reduction in tube leakage & shutdown time.

Monitor flue gas temperature from 32 ºF to 3500 ºF (0 ºC to 1927 ºC) for boiler startup, preventing over firing that could damage superheat tubes, and in

worst case it can lead to tube leakage, resulting in unit shut down for 24- 150 hours.

F. Replacement of Contact type Probes.

In the old thermal power plants, we used to have Furnace Temperature probe for measuring furnace temperature. This long probe used to get bent and stuck up inside the furnace.

G. Detection of shifting of combustion zone.

Isothermal mapping shows whether combustion ball is shifted towards any of the sides inside the boiler leading to overheating of particular side water wall tubes.

5. Conclusion

In this paper, we summarize the acoustic signal detection applications in boiler of a thermal power plant. According to our research, the acoustic technology has wide application in boilers. Early detection of faults will decrease the amount of repairs to be made and the unit downtime. Acoustic based detection system for steam leaks, clinker formation and combustion profile is an excellent method of minimizing downtime, improving reliability, efficiency and emission control. All the three applications have been implemented successfully in a 500 MW power plant.

References

[1]. T. Usami, Plant equipment diagnosis by sound processing, in *Proceedings of the 25th Annual Conference of the IEEE Industrial Electronics Society (IECON 99)*, Cat No 99CH37029, 1999.
[2]. http://www.babcock.com
[3]. http://www.wseaus.com
[4]. http://www.enertechnix.com
[5]. George Kychakoff, Michael F. Anna, Sagar Naik, Advances in acoustic pyrometry Provide improved temperature measurement for combustion and emission control, IPS 2016.
[6]. Kovecevich, S. P. Nuspl and M. O. Robertson, Recent advances in the application of acoustic leak detection to process recovery boilers, in *Proceedings of the TAPPI Engineering Conference*, 1996.
[7]. ASLD manual by M/s BHEL
[8]. Don-Hyun Kim, Bo-Suk Yang and Sang-Bum Lee, 3D boiler tube leak detection technique using acoustic emission signals for power plant structure health monitoring, in *Proceedings of the IEEE Prognostics and System Health Management Conference,* 24 -25 May 2011.
[9]. N. Hare, M. G. Rasul and Moazzem, A review on boiler deposition/Fouling prevention and removal techniques for power plants, in *Proceedings of the 5th IASME/WSEAS international conference on Energy & Environment (EE'10)*, 2010, pp. 217-222.
[10]. Manuals of Acoustic Pyrometer by Boiler Watch USA.

Published by International Frequency Sensor Association (IFSA) Publishing, S. L., 2017 (http://www.sensorsportal.com).

Aims and Scope

Sensors & Transducers is established, international, peer-reviewed, open access journal (print and electronic). It provides the best platform for the researchers and scientist worldwide to exchange their latest findings and results in science and technology of physical, chemical sensors and biosensors. The journal publishes original results of scientific and research works related to strategic and applied studies in all aspects of sensors: reviews, regular research and application specific papers, and short notes. In comparison with other sensors related journals, which are mainly focused on technological aspects and sensing principles, the *Sensors & Transducers* significantly contributes in areas, which are not adequately addressed in other journals, namely: frequency (period), duty-cycle, time-interval, PWM, phase-shift, pulse number output sensors and transducers; sensor systems; digital, smart, intelligent sensors and systems designs; signal processing and ADC in sensor systems; advanced sensor fusion; sensor networks; applications, etc. By this way the journal significantly enriches the appropriate databases of knowledge.

Sensors & Transducers journal has a very high publicity. It is indexed and abstracted very quickly by Chemical Abstracts, EBSCO Publishing, IndexCopernicus Journals Master List (ICV=6.13 in 2011), ProQuest Science Journals, CAS Source Index (CASSI), Ulrich's Periodicals Directory, Scirus, Google Scholar, etc. Since 2011 to 2014 *Sensors & Transducers* journal was covered and indexed by EI Compendex (CPX) index (including a Scopus, Embase, Engineering Village and Reaxys) in Elsevier products. The journal is included in the IFSA List of Recommended Journals (up-dated 9.12.2015), which contains only the best, established sensors related journals.

Topics of Interest

Include, but are not restricted to:

- Physical, chemical sensors and biosensors
- Digital, frequency, period, duty-cycle, time interval, PWM, pulse number output sensors and transducers
- Theory, principles, effects, design, standardization and modelling
- Smart sensors and systems
- Intelligent sensors and systems
- Sensor instrumentation
- Virtual instruments
- Sensors interfaces, buses and networks
- Signal processing, sensor fusion
- Remote sensing
- Frequency (period, duty-cycle)-to-code converters, ADC
- Technologies and materials
- Nanosensors and NEMS
- Microsystems
- Applications

Further information on this journal is available from the Publisher's web site:
http://www.sensorsportal.com/HTML/DIGEST/New_Digest.htm

Free Access and Subscriptions

Sensors & Transducers is the open access journal. All single articles are available for free download (article by article) without any registration and embargo period. For those who want to get the full page journal issue in print and/or pdf format there is an annual subscription. It includes 12 regular issues and some special issues. Annual subscription rates for 2016/2017 are the following: Electronic version (in printable pdf format): 590.00 EUR; Printed with b/w illustrations: 950.00 EUR; 15 % discount is available for IFSA Members.

Further information about subscription is available on the IFSA Publishing's web site: http://www.sensorsportal.com/HTML/DIGEST/Journal_Subscription.htm

Advertising Information

If you are interested in advertising or other commercial opportunities please download our Media Planner 2016: http://www.sensorsportal.com/DOWNLOADS/Media_Planner_2016.pdf

Instructions for Authors

http://www.sensorsportal.com/HTML/DIGEST/Guides_for_Authors.htm

Theory:

Digital Sensors and Sensor Systems: Practical Design

and

Practice:

Development Board EVAL UFDC-1/UFDC-1M-16

+

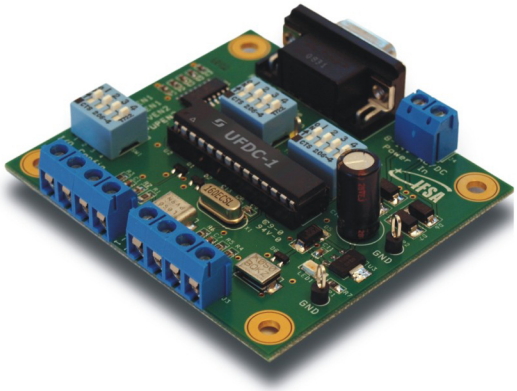

Buy book and Evaluation board together. **Save 30.00 EUR**

Development Board EVAL UFDC-1 / UFDC-1M-16

Full-featured development kit for the Universal Frequency-to-Digital Converters UFDC-1 and UFDC-1M-16. 2 channel, 16 measuring modes, high metrological performance, RS232/USB interface, master and slave communication modes. On-board frequency reference (quartz crystal oscillator). Operation from 8 to 14 V AC/DC. Development board software is included.

All existing frequency, period, duty-cycle, time interval, pulse-width modulated, pulse number and phase-shift output sensors and transducers can be directly connected to this 2-channel DAQ system. The user can connect TTL-compatible sensors' outputs to the Development Board, measure any output frequency-time parameters, and test out the sensor systems functions.

Applications:

- Digital sensors and sensor systems
- Smart sensors systems
- Data Acquisition for frequency-time parameters of electric signals
- Frequency counters
- Tachometers and tachometric systems
- Virtual instruments
- Educational process in sensors and measurements
- Remote laboratories and distance education

Order online:
http://www.sensorsportal.com/HTML/BOOKSTORE/Digital_Sensors_and_Board.htm

IFSA

International Frequency Sensor Association Publishing

www.sensorsportal.com

ISSN 1726- 5479